EVALUATION OF ADVANCED OXIDATION TECHNOLOGIES AND NANOSCALE PARTICLES FOR WATER AND GROUNDWATER REMEDIATION

by

Dila Aksoy

BS. in Env.E. Yıldız Technical University, 1999

M.S. in E.Tech., Boğaziçi University, 2001

Submitted to the Institute of Environmental Sciences in partial fulfillment of the requirements for the degree of

Doctor

of

Philosophy

Boğaziçi University
2008

EVALUATION OF ADVANCED OXIDATION TECHNOLOGIES

AND

NANOSCALE PARTICLES

FOR WATER AND GROUNDWATER REMEDIATION

APPROVED BY:

Prof. Dr. Nilsun H. İnce . . . . . .

(Thesis Supervisor)

Assoc. Prof. Nadim Copty . . . . . .

(Co-Supervisor)

Prof. Dr. İlhan Talınlı . . . . . .

Prof. Dr. Orhan Yenigün . . . . . .

Assoc. Prof. Turgut Onay . . . . . .

DATE OF APPROVAL 05.03.2008

ACKNOWLEDGEMENTS

I would like to express my sincere gratitude to my thesis supervisor Prof. Dr. Nilsun H. İnce and my co-supervisor Assoc. Prof. Nadim Copty for their support, valuable criticism and endless patience throughout my study. I am extremely grateful to them for their supervision, advice, and guidance from the very early stage of this research as well as giving me extraordinary experiences throughout the work.

I would like to thank Scientific and Technical Research Council of the Turkish Republic (TUBITAK) for the funding of 104I130 project.

I am thankful to my jury members Prof. Dr. İlhan Talınlı, Prof. Dr. Orhan Yenigün, and Assoc. Prof. Turgut Onay for their critical and supportive comments.

I am much indebted to my dear friend and sister Işıl Gültekin for her endless support and help. I deeply acknowledge Gülhan Özkösemen and Asu Ziylan for their help during my laboratory studies. Collective and individual acknowledgements are also owed to my friends at Institute of Environmental Sciences. I am also thankful to Assist. Prof. Funda Yağcı Acar for providing me the nanoparticle samples.

I keep the most special thank for my parents K. Aydın and Türkan N. Aksoy who sincerely raised me with their caring and gently love. I convey special acknowledgement to them for their indispensable support, motivation and encouragement.

My dear sister Esra and brother in law Mert deserve special mention for their inseparable support, endless love, patience and encouragement.

Words fail me to express my appreciation and gratitude to Ege Erşenkal whose dedication, love and persistent confidence in me, has taken the load off my shoulder.

Finally, I would like to express my gratitude and thanks wholeheartedly to everybody who contributed to the successful realization of the thesis.

ABSTRACT

Advanced Oxidation Processes (AOP) that are based on the in-situ generation of hydroxyl radicals in solution are extremely powerful tools for the destruction of recalcitrant compounds in water and groundwater. Recent research has shown that subsurface injection of nanoparticles may also be a viable technology for the in-situ remediation of contaminated groundwater resources.

The purpose of this study was to assess the degradability of typical groundwater contaminants, namely phenol and 2-chlorophenol by advanced oxidation processes, nanoparticles and combinations thereof. Advanced oxidation processes investigated were ozonation, UV irradiation, sonolysis, and sono-Fenton process. Experiments with nanoparticles involved batch adsorption tests to assess the adsorptive properties of the target contaminants followed by combined processes involving the particles and ultrasound. All those experiments in the first part of the study involving AOP and nanoparticles were run in batch reactors investigating the impacts of operational parameters such as pH, ultrasonic frequency, initial contaminant concentration, ozone flow rate, and reagent dose. In the second part of the research, flow-through reactors were used to test the mobility of the selected nanoparticle solutions in porous media under different flow configurations.

It was found that the rate of destruction of the test compounds by AOP followed pseudo-first order kinetics. Ultrasonic experiments revealed that the reactions were faster at higher ultrasonic frequencies and under Argon atmosphere. It was also found that the use of ultrasound and hydrogen peroxide together with particle suspensions and nanoparticles significantly enhanced the degradation efficiency.

Continuous flow experiments mainly focused on the assessment of the mobility of nanoparticle solutions in porous media under different flow configurations. Comparison of the nanoparticle breakthrough curves to that of the conservative tracers showed that the transport of nanoparticles is influenced by their concentration, which strongly controls the

particle size and hence, their mobility. Decreasing the concentration of nanoparticles in solution resulted in an increase in the effective size, which in turn reduced their mobility.

Overall, this study has demonstrated that phenolic compounds in contaminated water and groundwaters may be effectively destroyed by use of optimized hybrid processes involving Advanced Oxidation Processes and nanoparticles. Furthermore, the experimental results show that the stabilization of nanoparticle solutions is a critical factor in their applicability for the in-situ remediation of contaminated water and groundwater resources.

ÖZET

Hidroksil radikallerinin oluşumunu temel alan İleri Oksidasyon Teknolojileri, sudaki ve yeraltısuyundaki bozunması zor bileşiklerin parçalanması için oldukça etkilidir. Son dönemdeki araştırmalar, kirlenmiş yeraltısuyu kaynaklarının in-situ olarak ıslah edilmesi için nanopartiküllerin yeraltına enjekte edilmesinin de yararlı bir teknoloji olduğunu göstermiştir.

Bu çalışmanın amacı, yeraltı kirleticilerinden olan fenol ve 2-klorofenolün ileri oksidasyon teknolojileri, nanopartiküller ve hibrid sistemler ile parçalanmasının değerlendirilmesidir. Kullanılan ileri oksidasyon teknolojileri ozon, ultraviyole (UV) ışıması, sesüstü dalgalar ve sono-Fenton proseslerini içermektedir. Nanopartiküller ile yapılan deneyler, hedef kirleticilerin adsorpsiyon kapasitelerinin değerlendirilmesi ve bu partiküllerin sesüstü dalgalar ile birlikte kullanılmasından oluşmaktadır. İlk bölümde ileri oksidasyon teknolojileri ve nanopartiküller ile gerçekleşirilen tüm deneyler doldur-boşalt reaktörlerde yapılmış ve pH, ultrasonik frekans, başlangıç kirletici konsantrasyonu, ozon debisi vb. operasyonel parametelerin arıtım hızı üzerindeki etkisi incelenmiştir. Çalışmanın ikinci bölümünde, nanopartikül çözeltilerinin gözenekli ortamda farklı akış konfigurasyonlarında taşınımını değerlendirmek için sürekli akış reaktörleri kullanılmıştır.

Kirleticilerin, İleri Oksidasyon Teknolojileri ile parçalanmasının 1.derece reaksiyon kinetiğini takip ettiği tespit edilmiştir. Ultrasonik deneyler, reaksiyonların yüksek frekanslarda ve Argonun bulunduğu ortamlarda daha hızlı olduğunu göstermiştir. Ayrıca, sesüstü dalgaların ve hidrojenperoksitin, partikül çözeltileri ve nanopartiküller ile birlikte kullanılması durumunda parçalanma veriminin belirgin derece arttığı görülmüştür.

Sürekli akış deneyleri nanopartikül çözeltilerinin gözenekli ortamda farklı akış konfigurasyonlarında taşınımını değerlendirmeye odaklanmıştır. Nanopartiküllerin kırınım grafiklerinin reaksiyona girmeyen izleyici grafikleri ile karşılaştırılması, bu partiküllerinin hareketinin, partikül boyutunu ve dolayısıyla taşınımını da kontrol eden konsantrasyondan etkilendiğini göstermektedir. Nanopartiküllerin konsantrasyonunun azalması ile nanopartiküllerin efektif boyutu artmakta ve dolayısıyla taşınım azalmaktadır.

Sonuç olarak, bu çalışma operasyonel parametrelerin optimizasyonu ile özellikle hibrid sistemler kullanıldığında kirlenmiş su ve yeraltısuyundaki fenolik bileşiklerin etkin arıtımının sağlandığını ortaya koymaktadır. Ayrıca, nanopartiküllerin stabilizasyonunun, kirlenmiş su ve yeraltısuyu kaynaklarının in-situ olarak ıslah edilmesi için kullanılmasında kritik bir faktör olduğu gösterilmektedir.

TABLE OF CONTENTS

LIST OF FIGURES

LIST OF TABLES

LIST OF SYMBOLS/ABBREVIATIONS

Symbol	Explanation	Units used
AOP	Advanced Oxidation Process	-
k’	Rate Constant	min^{-1}
K	Hydraulic Conductivity	$m\ s^{-1}$
D	Hydrodynamic Dispersion	-
D_d	Effective Molecular Coefficient	-
D_m	Mechanical Mixing	-
D_0	Diffusion Coefficient in a Water Body	-
DCP	Dichlorophenol	-
ESS	European Society of Sonochemistry	-
PAA	Polyacrylic Acid	-
PCP	Pentachlorophenol	-
RNIP	Reactive Nanoscale Iron Particle	-
SBL	Single Bubble Luminescence	-
SET	Sinle Electron Transfer	-
TCA	Trichloroethane	-
TCP	Trichlorophenol	-
TeCP	Tetrachlorophenol	-
TOC	Total Organic Carbon	$mg\ L^{-1}$
US	Ultrasound	-
UV	Ultraviolet	-
ZVI	Zero-Valent Iron	-
2-CP	2-Chlorophenol	-
θ_t	Porosity	-
α	Dispersivity	-
τ	Tortuosity	-

1. INTRODUCTION

The contamination of soil and surface and subsurface with organic compounds such as chlorinated hydrocarbons and aromatic hydrocarbons has long been of concern, thus stimulating the continuous development of recently analytical and site remediation technologies. The carbon-chlorine (C-Cl) bond in all chlorinated organics increases their stability, causing the molecules to remain in the environment for long time periods, threatening aquatic and soil systems (Schwarzenbach et al., 1993).

The transport of these contaminants within compartments of the environment follows pathways such as volatilization, biodegradation partitioning into water, oxidation, and photodegradation. There are also reported occurrences of bioaccumulation of anthropogenic chlorinated compounds in areas remote from human settlements. Such widespread distribution of these compounds is believed to be due to their use in a broad spectrum of industrial applications and their long-range transport in the environment.

The wide use of chlorinated and aromatic hydrocarbons poses a critical environmental problem. Accidental spills or leaks from storage tanks cause these compounds to reach the subsurface and contaminate the groundwater. Cleanup of soils and groundwater contaminated by these compounds has been a focus of numerous environmental remediation studies. The primary obstacle is the lack of cost-effective remediation techniques. Field applications have shown that conventional groundwater remediation schemes- such as pump and treat- are not efficient in the recovery of large fractions of the contaminant mass. Therefore, there is an urgent need for developing new cost-effective in-situ techniques for the cleanup of soils and groundwater contaminated by chlorinated hydrocarbons.

There has been much research into the removal of chlorinated and aromatic hydrocarbons compounds from contaminated sites. Major conventional destruction technologies involve biological, thermal and chemical treatments (Jardim et al., 1997). The need to achieve a complete mineralization and produce less harmful intermediates has led to the development of new alternative technologies. Among these technologies, Advanced

Oxidation Processes (AOP) are proven to be a promising field of study due to their ability to dismantle and completely mineralize a wide range of pollutants in short periods of time.

AOPs are based on the generation of powerful hydroxyl radicals that have the potential to render destruction and complete mineralization of organic compounds to carbon dioxide and water. One of the novel approaches of AOPs is the use of ultrasonic waves alone and in combination with particles to degrade organic contaminants that cannot be destroyed by conventional treatment methods. The use of ultrasound in environmental applications has gained interest owing to the unique properties of ultrasound to induce sonochemical effects (Ince et al., 2001).

Recently published studies have shown that the use of reactive nanoparticles for the in-situ remediation of groundwater contaminated with organic compounds holds significant promise. The benefit of using nanoparticles is the potentially high reaction rates due to their large specific surface area and their ability to be injected into groundwater systems and flow through the porous medium. However, several issues regarding their reactivity with the organic compounds remain unresolved as well as their deliverability, and mobility in porous media. Despite the research reported in the literature, there remain several uncertainties and unanswered questions about the implementation of nanoparticles for in-situ groundwater remediation. As a consequence, much research is needed to obtain fundamental information on the behavior of these particles in groundwater systems and to develop realistic models that will be helpful in application of nanoparticle technologies for groundwater remediation.

The objectives of this research were: i) lab-scale analysis of ultrasound (US), ozone (O_3), ozone/ultraviolet light (UV), nanoparticles and hybrid systems to evaluate the performance of each for the degradation of groundwater contaminants (e.g. phenol and 2-chlorophenol) in batch reactors; ii) lab-scale analysis of nanoparticles in flow-through reactors simulating a groundwater system to prepare the background information for the development of an in-situ groundwater treatment model. The first part involved parameter analysis of ozonation (with or without UV irradiation), sonication, adsorption (on nano/micro-particles) and combined systems based on the rate of contaminant degradation. In the second part of this study, selection of the best nanoparticle (based on reliability of

particle size analysis) in flow-through reactors to investigate the mobility and migration profiles in the subsurface with respect to different hydrologic regimes are investigated so as to assess the potential of the system for field applications.

The dissertation covers:

1. Theoretical background of advanced oxidation processes, ultrasonic cavitation/sonochemistry, nanoparticles, and transport of contaminants in groundwater (Chapter 2).
2. Literature review addressing results of those studies related to the destruction of common groundwater contaminants such as phenol and 2-chlorophenol (Chapter 3).
3. Description of the experimental methods (Chapter 4).
4. Determination of ultrasonic power density (Chapter 5).
5. Results and discussion of batch experiments with varying AOPs and nano/micro-particles (Chapter 6).
6. Results and discussion of flow-through experiments in simulated groundwater systems (Chapter 7).
7. Conclusions and recommendations for future work (Chapter 8).

2. THEORETICAL BACKGROUND

2.1. Advanced Oxidation Processes

Advanced oxidation processes (AOPs), which involve the in-situ generation of highly potent chemical oxidants such as the hydroxyl radical (•OH) have recently emerged as an important class of technologies for accelerating the oxidation and hence destruction of a wide range of organic contaminants in water (Bolton, 1994). AOPs involve two stages of oxidation: 1) the formation of strong oxidants (i.e., hydroxyl radicals) and 2) the reaction of these oxidants with organic contaminants in water. However, the term "advanced oxidation processes" refers specifically to processes in which oxidation of organic contaminants occurs primarily through reactions with hydroxyl radicals (Glaze et al., 1987). Relative oxidation power of some oxidizing species and the second order reaction rate constants of some organic pollutants with ozone and hydroxyl radicals are summarized in Table 2.1 and Table 2.2, respectively. As a final remark, it should be noted that the attack of a hydroxyl radical depends on the nature and structure of the organic contaminant: it may either (i) abstract a hydrogen atom from water as with alkanes and alcohols, or (ii) add itself to the contaminant as with aromatic compounds.

Table 2.1. Relative oxidation power of some oxidizing species (Carey, 1992).

Oxidizing Species	Relative Oxidation Power
Chlorine	1.00
Hypochlorous Acid	1.10
Permanganate	1.24
Hydrogen Peroxide	1.31
Ozone	1.52
Atomic Oxygen	1.78
Hydroxyl Radical	2.05
Positively Charged Hole on TiO_2^+	2.35

Table 2.2. Reaction rate constants (k, $M^{-1}s^{-1}$) of O_3 vs. •OH (Solarchem Environmental Systems).

Compounds	**O_3**	**•OH**
Chlorinated Alkenes	10^3 to 10^4	10^9 to 10^{11}
Phenols	10^3	10^9 to 10^{10}
N-Containing Organics	10 to 10^2	10^8 to 10^{10}
Aromatics	1 to 10^2	10^8 to 10^{10}
Ketones	1	10^9 to 10^{10}
Alcohols	10^{-2} to 1	10^8 to 10^9

AOPs promote reactions that bring about a nearly complete oxidation of the pollutants to yield HCO_3^- and H_2O for complete mineralization of organic carbon to CO_2. However, such may require large quantities of energy chemical dosages thus to end up as economically non-feasible.

The following is a brief summary of most common AOPs, which are generally classified as either (i) homogeneous or (ii) heterogeneous.

2.1.1. Homogeneous AOPs

2.1.1.1. Photochemical Homogeneous AOPs.

UV/H_2O_2

The UV/ H_2O_2 system generates •OH by photolyzing the peroxide HO-OH bond with UV light below 300 nm (Yao and Mill, 1994). Generation of •OH by UV photolysis of H_2O_2 is described by the following reaction:

$$H_2O_2 + h\nu \longrightarrow 2\ \bullet OH \qquad (2.1)$$

Low pressure mercury vapor UV lamps with a 254 nm peak emission are typically used to produce UV radiation, but these lamps may not be the best choice for a UV/H_2O_2 process because the maximum absorbance of UV radiation by H_2O_2 occurs at about 220 nm and because the molar absorption coefficient of H_2O_2 at 254 nm is low. If low-pressure mercury lamps are used, a high concentration of H_2O_2 is needed in the medium to generate sufficient •OH because of the low molar absorption coefficient. High concentrations of H_2O_2, HCO_3^- and CO_3^{-2} may scavenge the •OH, making the UV/H_2O_2 process less effective due to the production of radical intermediates, •OH, HO_2•, $•O_2^-$, and $•CO_3^-$ as shown in reactions 2.2, 2.3, 2.4, and 2.5.

$$•OH + H_2O_2 \longrightarrow H_2O + HO_2• \quad (2.2)$$

$$•OH + HO_2^- \longrightarrow •O_2^- + H_2O \quad (2.3)$$

$$•OH + HCO_3^- \longrightarrow H_2O + •CO_3^- \quad (2.4)$$

$$OH + CO_3^{-2} \longrightarrow HO^- + •CO_3^- \quad (2.5)$$

To overcome this limitation, some AOP technology vendors use high intensity, medium-pressure, broad band UV lamps; others use high intensity, xenon flash lamps whose spectral output can be adjusted to match the absorption characteristics of H_2O_2 or another photolytic target (EPA, 1998).

UV/Ozone (O_3)

O_3 has been used successfully for removing various synthetic organic compounds from water. It is selective in its reaction with organic substances and might also decompose in water to generate •OH (Akata and Gurol, 1992). UV photolysis of O_3 in water yields H_2O_2, which in turn reacts with UV radiation of O_3 to form •OH as shown below.

$$O_3 + h\nu + H_2O \longrightarrow H_2O_2 + O_2 \quad (2.6)$$

$$H_2O_2 + h\nu \longrightarrow 2\ •OH \quad (2.7)$$

$$2\ O_3 + H_2O_2 \longrightarrow 2\ •OH + 3O_2 \quad (2.8)$$

$$O_3 + h\nu \longrightarrow O_2 + O\ (^1D) \quad (2.9)$$

$$O\ (^1D) + H_2O \longrightarrow 2\ •OH \quad (2.10)$$

However, generation of H_2O_2 by photolysis of ozone at short wavelengths is an expensive way to produce •OH radicals despite the fact that photochemical cleavage of H_2O_2 is conceptionally the simplest method for generating hydroxyl radicals. The handicap arises from the fact that H_2O_2 has very low absorbptivity at 254 nm that limits the yield of •OH radicals in solution.

UV/ H_2O_2/O_3 Process

The addition of hydrogen peroxide to the ozone/UV process accelerates the decomposition of ozone, resulting in an enhanced rate of •OH radical production as shown below.

$$H_2O_2 \longleftrightarrow HOO^- + H^+ \quad (2.11)$$

$$O_3 + HOO^- \longrightarrow \bullet OH + O_2^{\cdot -} + O_2 \quad (2.12)$$

$$O_3 + O_2^{\cdot -} \longrightarrow O_3^{\cdot -} + O_2 \quad (2.13)$$

$$O_3^{\cdot -} + H_2O \longrightarrow \bullet OH + HO^- + O_2^{\cdot} \quad (2.14)$$

Photo-Fenton Process

The rate of removal of organic pollutants and the extent of mineralization with the Fe (II)/ H_2O_2 and Fe (III)/ H_2O_2 reagents are improved considerably by irradiation with near-UV radiation and visible light (Ruppert et al., 1993). This process, called the photo-Fenton reaction, is shown in Figure 2.1 (A is the target contaminant. A* and A• are reaction intermediates).

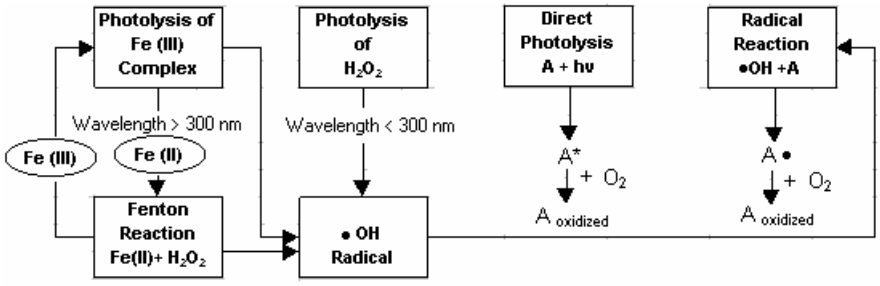

Figure 2.1. Scheme of chemical reactions in the photo-Fenton reaction (Kim et al., 1997).

Photoenhancement of reaction rates is due to (1) photoreduction of Fe(III) to Fe(II); (2) photodecarboxylation of ferric carboxylate complexes; and (3) photolysis of H_2O_2:

(1) Photoreduction of Fe (III) to Fe (II)

$$Fe\ (III)\ (OH)_2^{+} + h\nu \longrightarrow Fe\ (II) + \bullet OH \qquad (2.15)$$

(2) Photodecarboxylation of ferric carboxylate complexes

$$Fe\ (III)\ (RCO_2)_2^{+} + h\nu \longrightarrow Fe\ (II) + CO_2 + R\bullet \qquad (2.16)$$

(3) Photolysis of H_2O_2

$$H_2O_2 + h\nu \longrightarrow 2\ \bullet OH \qquad (2.17)$$

The initial rate of removal of organic pollutants by the Fe(III)/H_2O_2 reagent is much slower than that for the Fe(II)/H_2O_2 reagent because of the lower reactivity of Fe(III) toward H_2O_2. These systems have their maximum activity at a pH of about 2.8-3.0. An increase or decrease in the solution pH reduces the activity of the metal ion sharply. At high pH, Fe(II) precipitates as ferric hydroxide and at lower pH the pre-complexation of Fe(III) with H_2O_2 is inhibited (EPA, 1998).

Although iron is a highly abundant and non-toxic element and H_2O_2 is easy to handle, there are some liabilities in this system such as additional chemical cost, sludge disposal cost, salt formation, and maintaining proper chemial reaction conditions (Tezcanlı, 1998).

2.1.1.2. Non-Photochemical Homogeneous AOPs. There are five well known methods for generating hydroxyl radicals without using light energy. These methods are ozonation at high pH, combining ozone with hydrogen peroxide, using Fe^{2+} ions as the catalyst (Fenton process), ultrasonically induced cavitation and ionizing radiation.

Ozone at High pH

Oxidation of organic species may occur due to a combination of reactions with molecular ozone and reactions with •OH radicals depending upon the pH of the aqueous solution. Molecular O_3 is the major oxidant at acidic pH and reacts directly by electrophilic attack, where as less selective and faster radical reaction oxidation (mainly •OH) becomes predominant at pH>7 as a consequence of OH^- accelerated O_3 decomposition (Glaze et al., 1987).

The reaction between hydroxide ions and ozone leads to the formation of super-oxide anion radical $\bullet O_2^-$ and hydroperoxyl radical $\bullet HO_2$. By the reaction between ozone and the super-oxide radical, the ozonide radical $\bullet O_3^-$ is formed, which decomposes immediately giving •OH radical. The net reaction of ozone with OH^- ions to produce •OH radicals is given below (Gottschalk et al, 2000):

$$3O_3 + OH^- + H^+ \longrightarrow 2\bullet OH + 4O_2 \qquad (2.18)$$

The rate of attack by OH radicals is typically 10^6 to 10^9 times faster than the corresponding reaction rate for molecular ozone. Staehelin and Hoigné (1982) have shown that the mechanism of reaction of ozone with another substrate may involve both direct reactions and indirect reactions with •OH even at neutral pH. The relative proportions of each depend on the type and concentration of the contaminants present.

Ozone and Hydrogen Peroxide (Peroxone)

Depending upon the pH of the medium, hydrogen peroxide partially dissociates into hydroperoxide ion, which initiates the decomposition cycle of ozone, resulting in the formation of •OH radicals (Gottschalk et al, 2000).

$$H_2O_2 + H_2O \longleftrightarrow HO_2^- + H^+ \qquad pK = 11.8 \qquad (2.19)$$

$$HO_2^- + O_3 \longrightarrow \bullet HO_2 + O_3^- \qquad k_1 = 2.8 \times 10^6\ M^{-1}s^{-1} \qquad (2.20)$$

$$H_2O_2 + \bullet OH \longrightarrow O_2^- + H_2O + H^+ \qquad k_2 = 2.7 \times 10^7\ M^{-1}s^{-1} \qquad (2.21)$$

$HO_2^- + \bullet OH \longrightarrow OH^- + \bullet HO_2$ $\quad k_3 = 7.5 \times 10^9\ M^{-1}s^{-1}$ (2.22)

The overall reaction for O_3 decomposition is:

$2O_3 + H_2O_2 \longrightarrow 2\bullet OH + 3O_2$ (2.23)

The concentration of H_2O_2 added is an important control parameter for the fact that excess amounts may induce inhibitory effects upon the reaction of H_2O_2 with •OH radicals (Ince and Gönenc, 1997).

Fenton Process

Decomposition of H_2O_2 using ferrous iron Fe (II) or ferric iron Fe (III) under acidic conditions to yield •OH is known as the classical Fenton process. One hundred years ago, the oxidation of maleic acid by Fe(II)-H_2O_2 was reported by Fenton. Decomposition of H_2O_2 is also catalyzed by Fe (III) (Walling, 1975). In this process, H_2O_2 is decomposed to the water molecule and O_2, and a steady-state concentration of Fe (II) is maintained during the decomposition (EPA, 2001).

$Fe\ (II) + H_2O_2 \longrightarrow Fe\ (III) + OH^- + \bullet OH$ (2.24)

The •OH thus formed either reacts with Fe(II) to produce Fe(III) or can react with and initiate oxidation of organic pollutants present in a waste stream.

$\bullet OH + Fe\ (II) \longrightarrow Fe\ (III) + OH^-$ (2.25)

$Fe\ (III) + H_2O_2 \longrightarrow Fe\ (II) + \bullet HO_2 + H^+$ (2.26)

$\bullet HO_2 + Fe\ (III) \longrightarrow Fe\ (II) + H^+ + O_2$ (2.27)

The use of Fe(II)/ H_2O_2 as an oxidant for wastewater treatment is attractive due to the fact that: iron is a highly abundant and non-toxic element and hydrogen peroxide is easy to handle and environmentally benign (Munter, 2001).

Ultrasonically Induced Cavitation

Propagation of an ultrasound wave in aqueous solution leads to the formation of cavitation bubbles and a prerequisite for these bubbles is the presence of a dissolved gas (Suslick, 1990). Cavitation refers to the formation, growth and implosive collapse of gas-or vapor filled cavities (bubbles) in a liquid matrix. The cavities grow as they absorb energy from alternating compression and expansion waves. As energy is absorbed, the surface area of a cavity increases during expansion cycles and decreases during compression cycles. Because the amount of gas that diffuses into or out of the cavity depends on the surface area of the cavity, diffusion into the cavity during expansion cycles exceeds diffusion out of the cavity during compression cycles. Over successive cycles, the cavity eventually reaches a critical size at which it can no longer absorb energy efficiently to sustain itself. At this point, the cavity cannot withstand the net external pressure of the surrounding water, and the cavity implodes in a very short time (about 10 microseconds) (EPA, 2001).

When the cavity implodes, the gas inside is compressed generating intense heat. This heat raises the temperature and pressure of the gas phase in the collapsing cavity and the water immediately surrounding it. Hence, following the violent collapse of the cavity the surrounding water rushes into the cavity. In that sense, cavitational collapse produces localized high-temperature (about 5000 °C) and high pressures (about 50 Mpa) in hotspots (Suslick, 1990). When the liquid is water, this results in molecular fragmentation of water vapor to yield •OH formation as (Ince et al., 2001):

$$H_2O \longrightarrow \bullet OH + \bullet H \qquad (2.28)$$

The hydroxyl radicals generated by water sonolysis may either react in the gas phase or recombine at the cooler gas-liquid interface and/or in the solution bulk to produce hydrogen peroxide and water as shown in Equations 2.29 and 2.30 (Ince et al., 2001; Fischer et al., 1986).

$$\bullet OH + \bullet H \longrightarrow H_2O \qquad (2.29)$$

$$2\bullet OH \longrightarrow H_2O \qquad (2.30)$$

$2\bullet OH \longrightarrow H_2O_2$ (2.31)

$2\bullet H \longrightarrow H_2$ (2.32)

Because •OH radicals are highly reactive they do not have a long travel pathlength into the bulk water. As a result, destruction of organic compounds by •OH mainly occurs in the cavity or near the cavity surface. Detailed information about sonochemistry is given in Chapter 2.2.

The combination of acoustic cavitation with ozonolysis has been studied in the past (Ince and Tezcanlı, 2001; Weavers et al., 1998; Olson and Barbier, 1994). During acoustic cavitation, O_3 is thermolytically decomposed in the gas phase of a cavity to form two OH radicals. In addition, because sonication of ozonated water produces H_2O_2, •OH also form near the surface of the cavity and the bulk water as a result of the reaction between O_3 and H_2O_2 (EPA, 2001).

Ionizing Radiation

In ionizing radiation process, ions and a variety of excited species that are extremely reactive are produced. The process is based on the chemical changes produced by the absorption of radiation of sufficiently high energy to produce ionization (Cooper et al., 1998). There are two types of ionizing radiation: Gamma irradiation and electron beam irradiation. Gamma irradiation is performed by the use of $Cobalt_{60}$ and electron beam irradiation is performed by the use of electron accelerators (McKeown et al., 1998).

2.1.2. Heterogeneous AOPs

2.1.2.1. UV/TiO_2 Processes. The basis of photocatalysis is "photo-excitation" of a solid semiconductor as a result of absorbing electromagnetic radiation. In such a process metal semiconductors are used to destroy environmental contaminants by means of light induced reactions. Under near UV irradiation a suitable semiconductor material such as TiO_2 may be excited by photons possessing energies of sufficient magnitude to produce conduction band electrons and valence band holes. The formation and availability of •OH are

maximized by addition of oxidants (H_2O_2, O_3). The primary photocatalytic mechanism is believed to proceed as follows (EPA, 1998):

$$TiO_2 + h\nu \rightarrow e^-_{CB} + h^+_{VB} \quad (2.33)$$

At the TiO_2 surface, the holes react with either H_2O or OH^- to form •OH as follows:

$$h^+_{VB} + H_2O \rightarrow \bullet OH + H^+ \quad (2.34)$$

$$h^+_{VB} + OH^- \rightarrow \bullet OH \quad (2.35)$$

2.2. Ultrasound and Sonochemistry

2.2.1. Ultrasound

Ultrasound is any sound above human hearing (>16 kHz) and has wavelengths between succession compression waves measuring roughly 10 cm to 10^{-3} centimeters (Suslick, web). Ultrasound is the part of the sonic spectrum which ranges from about 20 kHz to 10 MHz and can be roughly subdivided into three main regions: (1) low frequency or conventional power ultrasound (20-100 kHz), (2) medium frequency or "sonochemical effects" ultrasound (300 kHz-1 MHz), and (3) high frequency or diagnostic ultrasound (2-10 MHz) (Ince et al., 2001).

2.2.2. Historical Background

The chemical effect of acoustic cavitation was first noticed in 1930's but the process was essentially untouched until mid 1980's. At this time inexpensive ultrasound equipment became commonplace and the process was rediscovered with various applications explored (Suslick et al., 1999). With the discovery of single bubble sonoluminescence (SBSL) in 1990 (Gaitan et al., 1990) many researchers rushed to explain this fascinating phenomenon of turning sound into light through a single micron sized bubble. SBSL provided a technique for isolating a single, stable acoustically forced cavitation bubble that was undergoing many of the same processes as the bubbles in sonochemistry. This growth in

SBSL research activity led to theoretical investigations of the behavior of the gas in the interior of strongly forced bubbles (Bremner et al., 2001).

2.2.3. Sonochemistry

Sonochemistry can be defined as chemistry induced by intense pressure waves in a liquid medium. Even though the chemical effects of ultrasound have been known for a long time, intensive studies in this area only began at the beginning of the 1980s (Dahlem et al., 1998). The chemical effects of ultrasound fall into three areas: homogeneous sonochemistry of liquids, heterogeneous sonochemistry of liquid-liquid or liquid-solid systems, and sonocatalysis (which overlaps the first two) (Suslick, web).

By ultrasonic waves in liquid media unique and extreme conditions are generated and this medium is remarkably suitable for 'high-energy chemistry'. These extremes promote the oxidative destruction of target contaminants via free radical reactions and provide an excellent medium for their thermal decomposition in the gas phase (Ince et al., 2001). Ultrasonic irradiation of liquids produces excessive energy for chemical reactions due to the physical phenomena that create the conditions necessary to drive chemical reactions. The most important of these is acoustic cavitation. It is the formation, growth and violent collapse of bubbles formed by coupling the pressure waves of ultrasound with a liquid (Hua and Hoffmann, 1996; Mason 1990).

Ultrasound is transmitted through a medium via pressure waves by inducing vibrational motion of the molecules which alternately compress and stretch the molecular structure of the medium due to a time-varying pressure. Therefore, the distance among the molecules varies as the molecules oscillate around their mean position. If the intensity of ultrasound in a liquid is increased, and the applied pressure is equal to the negative pressure developed in the rarefaction cycle of the wave such that the distance between the molecules of the fluid exceeds the critical molar distance to hold it together, the liquid breaks apart to form cavities made of vapor and gas filled microbubbles. This cavity is called "cavitation bubble" as this process is called "acoustic cavitation" and the point where it starts "cavitation threshold".

The phenomenon of acoustic cavitation consists of at least three stages: 1) nucleation, 2) bubble growth (expansion), and 3) implosive collapse. The first stage is a nucleated process, by which cavitational nuclei are generated from microbubbles trapped in microcrevices of suspended particles within the liquid. In the bubble growth stage, the bubbles grow and expand in a manner restricted by the intensity of the applied sound wave. The third stage occurs only if the intensity of the ultrasound wave exceeds that of the "'acoustic cavitational threshold". At this condition, the microbubbles overgrow to the extent where they can no longer efficiently absorb energy from the sound environment to sustain them and implode violently. The temperatures and pressures within a collapsing microbubble can reach values as high as 4200-5000 K and 200-500 atm respectively (Ince et al., 2001).

Two types of cavitation are known: stable and transient. Stable cavitation means that the bubbles oscillate around their equilibrium position over several refraction/compression cycles. These stable bubbles are formed by power ultrasound and they have enough time to expand. In transient cavitation, the bubbles grow over one (sometimes two or three) acoustic cycles to double their initial size and finally collapse violently. Transient bubbles are formed by the application of medium frequency ultrasound and they do not have enough time to grow to form large bubbles. Transient cavitation induces the implosive collapse of gas and vapor bubbles and thus generates transient "hot-spots'' with local temperatures and pressures thought to be several thousand degrees Kelvin and hundreds of atmospheres (Margulis and Dmitrieva, 1982). The pressures and temperatures developed in transient cavitations are much higher than found in stable cavitations because in stable cavitation phenomena there is lots of time for the diffusion of dissolved gases and vapors into the bubble. Therefore this collapse has a "cushion effect" (Ince et al., 2001).

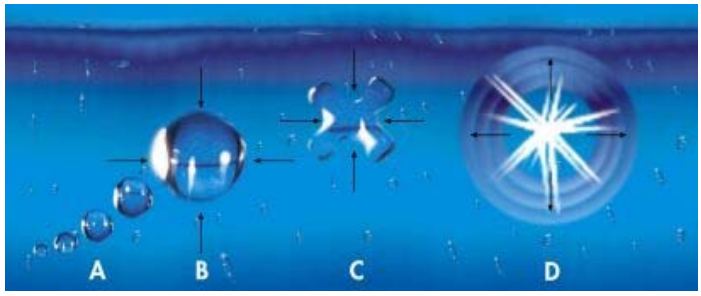

Figure 2.2. Formation, growth and implosion of a cavitation bubble (Suslick, 1994).

During phase A, numerous gas bubbles are formed in the liquid and these bubbles expand during time. The formation of gas bubbles is the start of cavitation. During the second phase of ultrasonic compression (phase B), the enormous pressure exerted on the expanded bubble causes the compression of the bubble (phase C) until the bubble implodes violently generating intense localized temperatures and pressures (phase D). The collapse becomes so rapid compared to the time it takes water to diffuse through the bubble interior that excess vapor becomes trapped inside. As the excess vapor is compressed by the collapse, the contents reach several thousand Kelvin and the trapped vapor is largely dissociated. In the case with water, it is the creation of hydroxyl radicals (•OH) from the hot vapor that is often of interest in applications (Mark et al., 1998; Gong and Hart, 1998; Storey and Szeri, 2002).

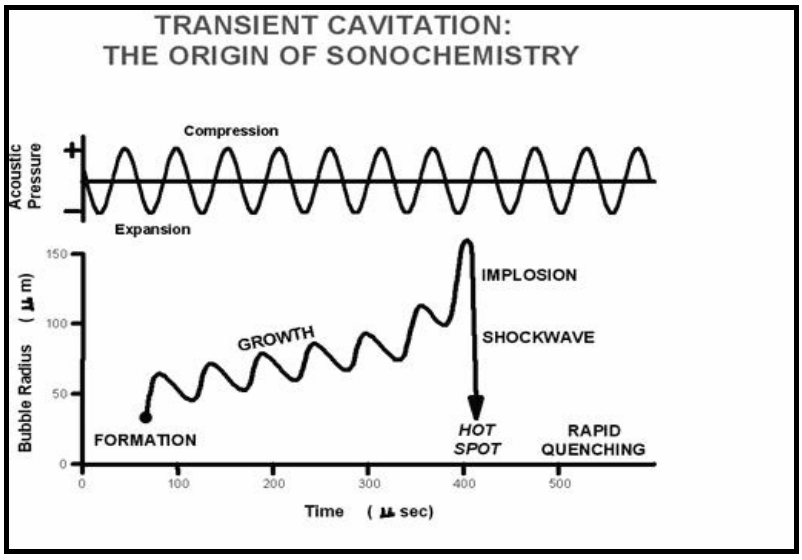

Figure 2.3. Transient cavitation: the origin of sonochemistry (Suslick, 1994).

2.2.3.1. Sites for Sonochemical Reactions. There are three potential reaction sites of a collapsing bubble for chemical reactions in ultrasonically irradiated liquids; (i) the cavitation bubble itself (the gaseous phase inside the bubble), (ii) the interfacial sheath between the gaseous bubble and the surrounding liquid and (iii) the surrounding liquid, the solution bulk as shown in Figure 2.4.

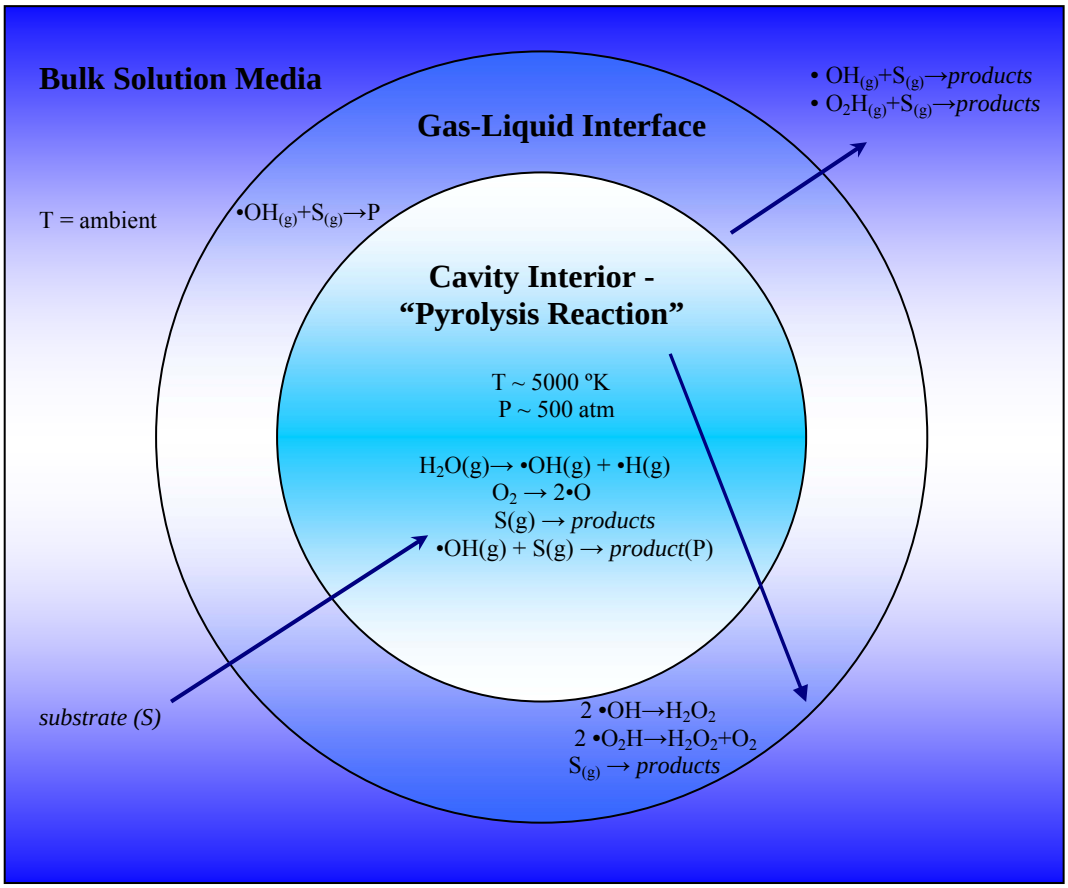

Figure 2.4. Possible sites of chemical reactions in homogeneous reaction media (Ince et al., 2001).

Organic pollutants may be destroyed either at the first two sites upon combined effects of pyrolytic decomposition and hydroxylation, or in the solution bulk via oxidative degradation by hydroxyl radicals and hydrogen peroxide (Ince et al., 2001, Weavers et al., 1998). The intensity of oxidation reactions in the latter site is directly and exclusively related to the quantity of available uncombined hydroxyl radicals, as they migrate into the aqueous phase during collapse of cavity bubbles. The extent of oxidation in the latter site is limited by the quantity of uncombined hydroxyl radicals available in solution.

To undergo a reaction inside the bubble where extreme conditions exist, a substrate must be easily expelled from the solution, either because of a low degree of salvation and/or a relatively high volatility with respect to the solvent. In water and aqueous

solutions, the predominant phenomenon is the sonolysis of the O-H bond, which occurs in the gas phase of the bubble (Henglein, 1991). Reactions in the interfacial region correspond to an indirect mechanism in which sonolysis of the solvent in the bubble or a volatile solute constitutes a first step. The sonolysis occurs with preferential hydroxylation and subsequent oxidations induced by the hydroxyl radical.

The third site where a reaction can take place is the solution itself. Substrates reacting at this site are non-volatile or strongly solvated compounds, with no special tendency to migrate towards the bubble boundary.

The hydroxyl radicals generated by water sonolysis may either react in the gas phase or recombine at the cooler gas-liquid interface and/or in the solution bulk to produce hydrogen peroxide and water as shown in the following equations (Ince et al., 2001; Riesz and Mason, 1991; Fischer et al., 1986):

$$H_2O +))) \longrightarrow \bullet OH + \bullet H \quad \text{(pyrolysis)} \tag{2.36}$$

$$\bullet OH + \bullet H \longrightarrow H_2O \tag{2.37}$$

$$2\bullet OH \longrightarrow H_2O \tag{2.38}$$

$$2\bullet OH \longrightarrow H_2O_2 \tag{2.39}$$

$$2\bullet H \longrightarrow H_2 \tag{2.40}$$

If the solution is saturated with oxygen, peroxyl and additional hydroxyl radicals are formed in the gas phase (due to the decomposition of molecular oxygen), and the recombination of the former at the cooler sites (interface or the solution bulk) produces more hydrogen peroxide, as shown (Ince et al., 2001; Makkino et al., 1982; Petriér et al., 1994):

$$O_2 + \bullet H \longrightarrow \bullet O_2H \tag{2.41}$$

$$O_2 +))) \longrightarrow O + O \tag{2.42}$$

$$O + H_2O \longrightarrow \bullet OH + \bullet OH \tag{2.43}$$

$$\bullet O_2H + \bullet O_2H \longrightarrow H_2O_2 + O_2 \tag{2.44}$$

Radical, mechanical or electrochemical effects are achieved depending upon the reaction site.

Radical Effects

(European Society of Sonochemistry-ESS, http://www.europeansocietysonochemistry.eu/)

- ligand-metal bond cleavage in transition metal complexes to give coordinatively unsaturated species or modified complexes as well as complete strip off of ligands to produce amorphous metals
- disrupture of the solvent structure altering the solvation of reactants
- sonolysis of molecules (homolytic fragmentation to radicals, rupture of polymers, generation of excited states, cell disrupture)

Mechanical Effects (ESS, http://www.europeansocietysonochemistry.eu/)

- mechanical effects by cavity collapse onto metals and solids (shear forces, jets and shock waves resulting in rapid mass transfer, surface cleaning, particle size reduction and metal activation), modification of the properties of solid particles

Electrochemical Effects (ESS, http://www.europeansocietysonochemistry.eu/)

- effects in liquid-liquid systems (improved mass transfer, emulsification, increase of the effect of phase transfer catalysts or even their replacement)
- effects in gas-liquid systems (degassing of liquids or melts, atomization of liquids in air, thin film preparation)
- single electron transfer (SET) steps in chemical reactions may be accelerated and if an ionic and an electron transfer pathway are possible the latter seems to be preferred ("sonochemical switching")

2.2.3.2. Parameters Affecting Sonochemical Reactions. The main concern of scientists and engineers working with ultrasonic systems is to accomplish maximum reaction yields and/or maximum pollutant destruction at optimal conditions (Ince et al., 2001). Research

and development in sonochemical systems exposed the significance of two basic strategies for maximizing reaction efficiencies: i) optimization of power and reactor configuration and/or ii) enhancement of cavitation. The first strategy requires a mechanistic approach with features like: (a) selection of the transducer (piezoelectric or magnetic material that converts electrical impulses to mechanical vibrations) and generator (probe types for low frequency, and plate types for high frequency effects), (b) configuration and dimensioning of the reaction cell, and (c) optimization of the power efficiency (i.e. the effective power density delivered to the reaction medium). The effect of frequency, applied pressure, power intensity and bulk solution temperature for the optimization of power and reactor configuration are explained. The effect of physicochemical properties of the pollutant and the solute, bubbled gas, and the solid addition to enhance cavitation, and therefore maximize chemical reactions are explained (Ince et al., 2001).

Frequency

The more important cavity effects are reported to occur when the frequency of the ultrasonic wave is equal to the resonating frequency of the bubbles. The resonance radius of a bubble excited by low frequency waves is reported to be ~170 μm (at 20 kHz), and the cavities entrapping such bubbles are said to be "stable" or long-lived, with average life times of ~10 μs (Mason, 1990; Petriér et al., 1994). In this kind of cavitation, the collapse stage is delayed till after the elapse of a number of compression and rarefaction cycles, during which sufficient volumes of volatile solutes and solvent vapors within the liquid may flow into the gas phase (Mason, 1990). The delayed growth and long collapse duration of gas-filled bubbles allow radical scavenging and recombination reactions at the interfacial sheath, thus inhibiting the mass transfer of hydroxyl radicals into the solution bulk (Barbier et al., 1996). Hence low frequency ultrasound is expected to induce effects only for hydrophobic solutes, which easily diffuse into the cavity bubbles to undergo pyrolytic destruction inside the collapsing bubble, or hydroxylation and thermal decomposition at its interfacial sheath, where pressure gradients and temperatures are still high enough to induce thermolytic fragmentation.

On the contrary, the resonance radii of bubbles excited by medium frequency (300-1000 kHz) ultrasound waves are extremely small (4.6 μm at 500 kHz), giving rise to very short-lived (0.4 μs on the average) and mainly void or vapor-filled "transient" cavitations (Ince et al., 2001; Mason, 1999). The pressures and temperatures developed in such cavities are much higher than found in"stable" cavities, and larger energies are released into the surrounding liquid during their more rapid and violent collapse (Mason et al., 1990; Henglein, 1987; Suslick, 1990). Furthermore, such cavitations are so short-lived and the collapse is so rapid that the time for appreciable degree of radical scavenging reactions in the hot bubble or at the interfacial region is insufficient. As a consequence, medium frequency waves are highly effective for oxidation reactions in the liquid bulk, due to the highly probable ejection of uncombined hydroxyl radicals into the surrounding liquid during collapse (Ince et al., 2001; Mason et al., 1994; Barbier et al., 1996).

It should be remembered that, lower frequency ultrasound produces more violent collapse, leading to higher localized temperatures and pressures. However, current research indicates that higher frequencies lead to higher oxidation reaction rates. Beckett and Hua (2001) have postulated that the degree of heat generated upon collapse would be most intense at lower frequencies but there would be more cavitation events and thus more opportunities for the free radicals to be produced and diffuse into the bulk media with increasing frequency. Thus, there should be an optimum frequency where the competing effects balance.

Power Intensity

The intensity of sonication (in W m^{-2}) is directly proportional to the square of the amplitude of vibration of the ultrasonic source (Equation 2.45). By increasing the amplitude, the power is increased, and in most cases, as the power is increased, the reaction rate also increases. It is important to remember that, as in the other cases, sonochemical activity rises with increasing intensity to an optimum at which efficiency falls. When a large amount of ultrasonic power enters a system, a great number of cavitation bubbles are generated in the solution. Many of these will come together to form larger and longer lived bubbles. These will certainly act as a barrier to the transfer of acoustic energy through the liquid (Mason, 1990).

$$I = \frac{P_a^{\,2}}{2\rho c} \qquad (2.45)$$

P_a : the acoustic power, W

ρ : the density of water, g cm^{-3}

c : the speed of sound in water, (1500 m s^{-1})

The acoustic power P_a represents the intensity emitted by a given surface. The term ρc represents the acoustic impedance (Z) of the medium.

In general an increase in intensity will provide an increase in sonochemical effects, but there are limits to the ultrasonic energy input to the system.

(i) A minimum intensity for sonication is required to reach the cavitation threshold. This minimum depends upon the frequency.

(ii) When a large amount of ultrasonic power enters a system, a great number of cavitation bubbles are generated in the solution. Many of these will coalesce forming larger, more long lived bubbles. These will certainly act as a barrier to the transfer of acoustic energy through the liquid.

(iii) At high vibrational amplitude the source of ultrasound will not be able to maintain contact with the liquid throughout the complete cycle. Technically this is known as decoupling, and results in a great loss in efficiency of transfer of power from the source to the medium. Decoupling is more effective when large numbers of cavitation bubbles build up at or near the emitting surface of the transducer.

Bulk Solution Temperature

Assuming adiabatic bubble collapse, the maximum temperatures within the collapsed cavitation bubbles are predicted from approximate solutions of Rayleigh-Plesset equations as stated in Equation 2.46 (Noltingk and Neppiras, 1950; Neppiras, 1980):

$$T_{max} = T_0 \left[\frac{P_a(\gamma - 1)}{P_v} \right] \quad (2.46)$$

where: T_{max} is the temperature reached after the collapse of the bubble, T_0 is the temperature of the sonication bath, $\gamma = Cp/Cv$, P_a is the external pressure equal to the sum of the hydrostatic and acoustic pressure, and P_v is the pressure of the gas inside the cavity, at the radius at which it collapses.

The choice of a nonvolatile solvent guarantees that only the vapors of the solute can be found inside the cavitating bubble. Thus P_v is practically the vapor pressure of the solute and lower P_v results in higher temperatures and faster reaction rates. At low vapor pressure, less vapor diffuses into the bubble thus favoring more violent collapse.

Physicochemical Properties of the Pollutant

It is obvious then that the selection of the right frequency range (the region of conventional power ultrasound, or that of "sonochemical effects" ultrasound) is of utmost significance for achieving appreciable degrees of decontamination. The choice is based primarily on the physicochemical properties of the contaminating species, such as vapour pressure (or Henry's constant), solubility and octanol-water partition coefficient (Log K_{ow}).

Hydrophobic chemicals with high vapor pressures have a strong tendency to diffuse into the gaseous bubble interior, so that the most effective reaction site for their destruction is the bubble-liquid interface and/or the gaseous bubble itself (Alegria et al., 1989; Kontronarou et al., 1991; Drijivers et al., 1999). Hence, irradiation of aqueous solutions contaminated with volatile pollutants by power ultrasound at 20-100 kHz (whereby long-lived "stable" cavities are generated) is a very effective decontamination method, owing to its potential to render pyrolytic destruction of the solutes in the gas and gas-liquid phase (Ince et al., 2001; Kontronarou et al., 1991).

In contrast, hydrophilic compounds with low vapor pressures and low concentrations tend to remain in the bulk liquid during irradiation, due to the repulsive forces exerted to-

and-from the slightly hydrophobic bubble surfaces. The major reaction site for these chemicals, therefore, is the liquid medium, where they may be destroyed by oxidative degradation, provided that sufficient quantities of hydroxyl radicals are ejected into the solution during cavitational collapse. As pointed out previously, maximum radical transfer into the bulk medium occurs when the collapse is “transient”, or when sonication is carried out via medium frequency ultrasound waves (Ince et al., 2001; Drijvers et al., 1999).

Thermal decomposition of non-volatile solutes is also possible at the interfacial bubble sheath, at which solutes may accumulate via adsorptive processes during the formation and growth of acoustic cavities, but is not as effective as hydroxylation in the bulk medium.

Dissolved Gases

Dissolved gas bubbles serve as nuclei for cavitation. However, since the first effect of cavitation is degassing, the solution will rapidly be free of dissolved gases if gas introduction is ceased during sonication (Mason, 1999). Therefore, the liquid is bubbled continuously with a gas throughout the sonication to maintain a constant gas flow into the bubbles so as to sustain the “extreme” conditions of collapse (Ince et al., 2001).

The selection of the gas is also of significance, because the final temperature of a collapsing bubble is closely related to specific heat (heat released upon gas compression), thermal conductivity (heat dissipation to the surrounding environment), and the solubility of the sparge gas. The higher the heat capacity ratio (C_p/C_v) or polytropic ratio (γ) of the gas in the bubble, the higher the final temperature produced in an adiabatic compression, and the cause of reaction (Hua and Hoffmann, 1997). Assuming adiabatic bubble collapse, the maximum pressures within the collapsed cavitation bubbles are predicted by Noltingk and Neprrias from approximate solutions of Rayleigh-Plesset equations as follows (Noltingk and Neppiras, 1950; Neppiras, 1980):

$$P_{max} = P_v \left\{ \frac{P_a(\gamma - 1)}{P_v} \right\}^{\left[\gamma/\gamma-1\right]} \quad (2.47)$$

where P_v = pressure in the bubble at its maximum size or the vapor pressure of the solution, P_a = pressure in the bubble at the moment of transient collapse (acoustic pressure), γ = polytropic index. As can be seen from these equations, higher temperatures and pressures are generated with monatomic gases with higher γ than those with polyatomic gases with lower γ (Riesz et al., 1990). The studies showed that γ is the highest for monatomic gases such as Ar, Ne, He; lower for diatomic gases such as N_2, O_2; and lowest for polyatomic gases such as CH_4 (Ince et al., 2001).

Another parameter that affects cavitational collapse is the thermal conductivity of the gas. Although compression is adiabatic in the sonochemical process, still small amounts of heat are transferred to the bulk liquid. A gas with low thermal conductivity reduces heat dissipation from cavitation site following adiabatic collapse and should favor higher collapse temperature. Thermal conductivity of rare gases decreases in the order: Xe < Kr < Ar < Ne < He. Despite the equal γ ratios of Ar and Helium, much higher yields of pyrolysis products were detected with Ar by Colarusso and Serpone (1996), as attributed to its 10-fold lower thermal conductivity. Gas solubility is also an important aspect, the more soluble the gas, the more likely it is to diffuse into the cavitation bubble. Hence, larger number of cavitation nuclei will form and will lead to an extensive bubble collapse (Kontronarou et al., 1991).

Addition of Solids

The addition of solid catalysts, such as glass beads, ceramic disks, SiO_2, Al_2O_3 and talc into the reaction medium is another common method for enhancing cavitation effects (Ince and Kidak, 2006). Furthermore, the presence of such material is reported to be especially useful for micronization of species (in ultrasonic cell disruption), and for the abrasion, activation and alteration of the chemical properties of catalyst surfaces during ultrasonic irradiation of liquid media (Ince and Kidak, 2006).

2.3. Nanoparticles and Nanotechnology

A nanometer is one billionth of a meter (10^{-9} m)—about one hundred thousand times smaller than the diameter of a human hair, a thousand times smaller than a red blood cell, or about half the size of the diameter of DNA. Figure 2.5 illustrates the scale of objects in the nanometer range (EPA, 2007).

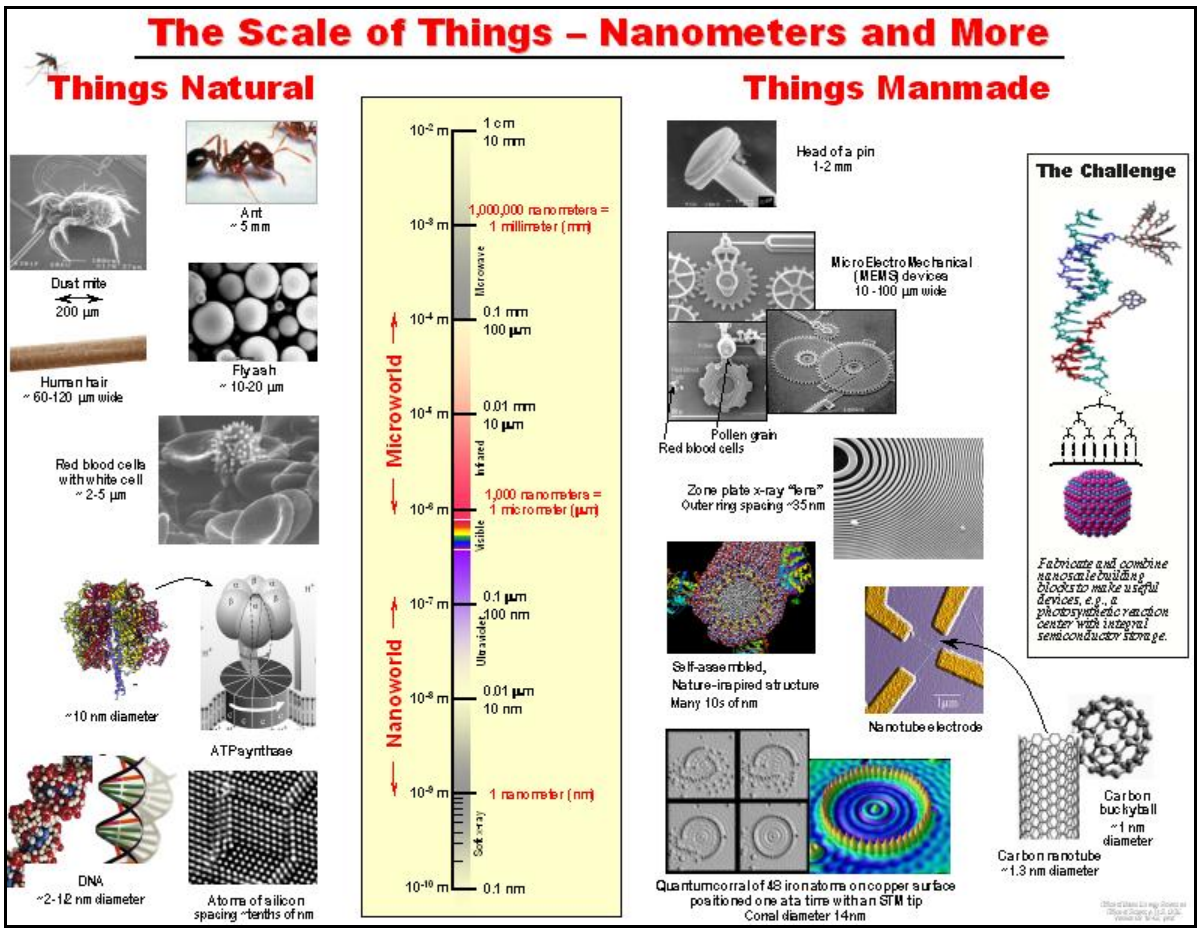

Figure 2.5. The scale of objects in the nanometer range (NNI website, courtesy Office of Basic Energy Sciences, U.S. Department of Energy).

A nanoparticle - a collection of tens to thousands of atoms measuring about 1-100 nm in aggregate diameter – is the most basic structure in nanotechnology. Such nanoparticles are created atom by atom, so the size, and often the shape of a particle are controlled by experimental conditions. These particles can also be described as nanocrystals, because the atoms within the particle are highly ordered or crystalline (Zhang and Masciangioli, 2003).

Nanomaterials can be categorized in four groups (EPA, 2007):

Carbon-based materials: These nanomaterials are composed mostly of carbon, most commonly taking the form of a hollow spheres, ellipsoids, or tubes. Spherical and ellipsoidal carbon nanomaterials are referred to as fullerenes, while cylindrical ones are called nanotubes. These particles have many potential applications, including improved films and coatings, stronger and lighter materials, and applications in electronics. Figure 2.6 shows an example of a carbon-based nanoparticle.

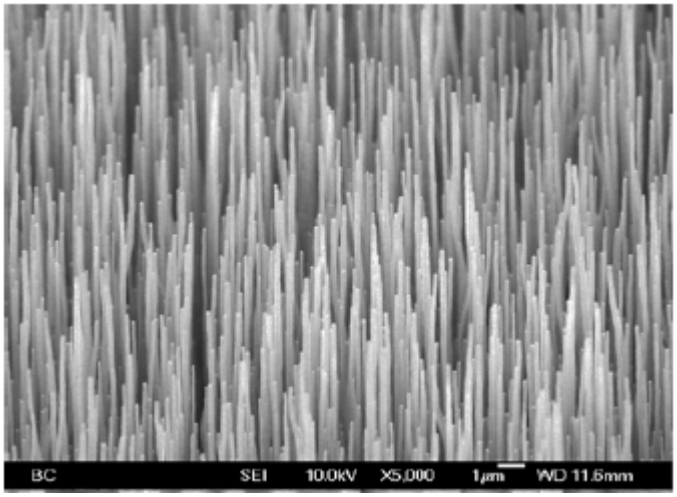

Figure 2.6. Image of a carbon nanotube (NanoLab, Inc.).

Metal-based materials: These nanomaterials include quantum dots, nanogold, nanosilver and metal oxides, such as titanium dioxide. A quantum dot is a closely packed semiconductor crystal comprised of hundreds or thousands of atoms, and whose size is on the order of a few nanometers to a few hundred nanometers. Changing the size of quantum dots changes their optical properties. Figure 2.7 is an example of a metal-based nanoparticle.

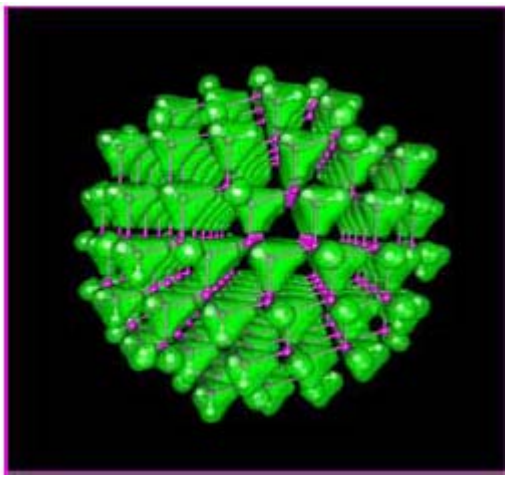

Figure 2.7. Computer image of a metal-based nanoparticle (Lawrence Berkeley Lab.).

Dendrimers: These nanomaterials are nanosized polymers built from branched units. The surface of a dendrimer has numerous chain ends, which can be tailored to perform specific chemical functions. This property could also be useful for catalysis. Also, because three-dimensional dendrimers contain interior cavities into which other molecules could be placed, they may be useful for drug delivery. Figure 2.8 illustrates the generation of a dendrimer.

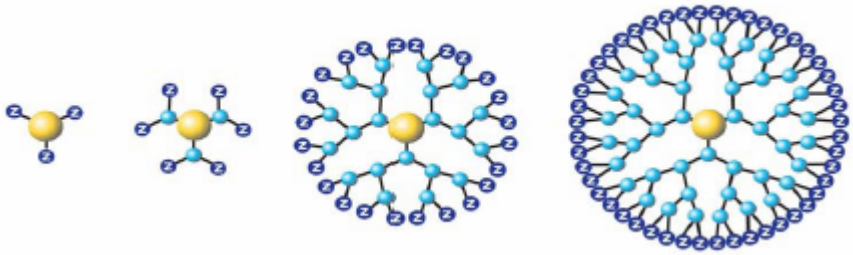

Figure 2.8. Computer image of generations of a dendrimer (Dendritic Nano Technologies, Inc.).

Composites: Composites combine nanoparticles with other nanoparticles or with larger, bulk-type materials. Nanoparticles, such as nanosized clays, are already being added to products ranging from auto parts to packaging materials, to enhance mechanical, thermal, barrier, and flame-retardant properties. Figure 2.9 illustrates the computer image of a nano composite.

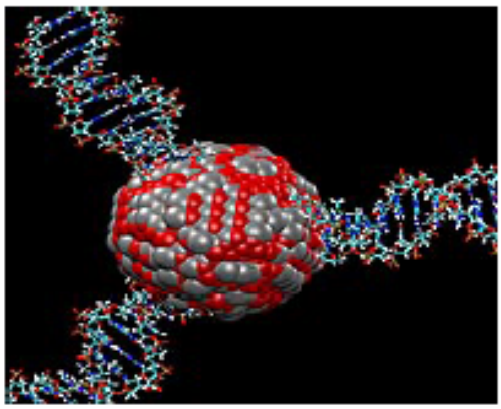

Figure 2.9. Computer image of a nano composite (Argonne National Lab.).

Chemical composition is an important parameter for the characterization of nanomaterials. Dependent on the particle surface chemistry, reactive groups on a particle surface will certainly modify the chemical and biological effects. Under ambient conditions, some nanoparticles can form aggregates or agglomerates. To maintain the characteristics of nanoparticles, they are often stabilized with coatings or derivative surface to prevent agglomeration. The properties of nanoparticles can be significantly altered by surface modification and the fate and transport of nanoparticles in the environment strongly depends upon the surface characteristics. To prevent aggregation or agglomeration, surface properties of the nanoparticles may be changed by coating of nanoparticles with different types and concentrations of surfactants.

The transition from microparticles to nanoparticles can lead to a number of changes in physical properties. Two of the major factors in this are the increase in the ratio of surface area to volume, and the size of the particle moving into the realm (Holister et al., 2003).

The increase in the surface area to volume ratio, which is a gradual progression as the particle gets smaller, leads to an increasing dominance of the behavior of atoms on the surface of a particle over that of those in the interior of the particle. This affects both the properties of the particle in isolation and its interaction with other materials.

The unique, nanostructure-dependent properties of nanoparticles (e.g., chemical, mechanical, electrical, optical, magnetic, biological) make them desirable for applications in commercial, medical, military, and environmental sectors.

Nanotechnology is defined as research and technology development at the atomic, molecular, or macromolecular levels using a length scale of approximately one to one hundred nanometers in any dimension; the creation and use of structures, devices and systems that have novel properties and functions because of their small size; and the ability to control or manipulate matter on an atomic scale. This definition is based on part on the definition of nanotechnology used by the National Nanotechnology Initiative (NNI), a U.S. government initiative launched in 2001 to coordinate nanotechnology research and development.

Nanotechnology holds great promise for creating new materials with enhanced properties and attributes. These properties, such as greater catalytic efficiency, increased electrical conductivity, and improved hardness and strength, are a result of nanomaterials' larger surface area per unit of volume and quantum effects that occur at the nanometer scale ("nanoscale"). Nanomaterials are already being used or tested in a wide range of products such as sunscreens, composites, medical and electronic devices, and chemical catalysts. Similar to nanotechnology's access in consumer products and other sectors, nanomaterials have promising environmental applications. For example, nanosized cerium oxide has been developed to decrease diesel missions, and iron nanoparticles can remove contaminants from soil and ground water.

Nanotechnology for groundwater remediation involves pumping nanoparticles--minute, magnetic particles into the groundwater. Nanoparticles have a large relative surface area and a high rate of reactivity. They also provide enormous flexibility for in situ applications. Recent research has shown that they are very effective for the transformation and detoxification of a wide variety of common environmental contaminants. When applied to water contaminated with carcinogenic solvents, nanoparticles can convert the solvents to harmless hydrocarbons. These studies demonstrate that nanoparticle technologies can potentially lead to a dramatic increase in remediation efficiency in

comparison to traditional cleanup methods that require water to be pumped out, treated, than disposed of.

2.3.1. The Fate of Nanoparticles in Soil

The fate of nanomaterials released to soil is likely to vary depending upon the physical and chemical characteristics of the nanomaterial. Nanomaterials released to soil can be strongly sorbed to soil due to their high surface areas and therefore be immobile. On the other hand, nanomaterials are small enough to fit into smaller spaces between soil particles, and might therefore travel further than larger particles before becoming trapped in the soil matrix. The strength of the sorption of any intentionally produced nanoparticle to soil will be dependent on its size, chemistry, applied particle surface treatment, and the conditions under which it is applied. Studies have demonstrated the differences in mobility of a variety of insoluble nanosized materials in a porous medium (Zhang, 2003; Lecoanet and Wiesner, 2004).

Additionally, the types and properties of the soil and environment (i.e., clay versus sand) can affect nanomaterial mobility. For example, the mobility of mineral colloids in soils and sediments is strongly affected by charge (Wiesner et al., 2004). Surface photoreactions provide a pathway for nanomaterial transformation on soil surfaces. Humic substances, common constituents of natural particles, are known to photosensitize a variety of organic photoreactions on soil and other natural surfaces that are exposed to sunlight. Studies of nanomaterial transformations in field situations are further complicated by the presence of naturally occurring nanomaterials of similar molecular structures and size ranges. Iron oxides are one example.

2.3.2. The Fate of Nanoparticles in Water

Fate of nanomaterials in aqueous environments is controlled by aqueous solubility or dispersability, interactions between the nanomaterial and natural and anthropogenic chemicals in the system, and biological and abiotic processes. Waterborne nanoparticles generally settle more slowly than larger particles of the same material. However, due to their high surface area to mass ratios, nanosized particles have the potential to sorb to soil

and sediment particles (Oberdörster et al., 2005). Where the soil and sediment particles are subject to sedimentation, the sorbed nanoparticles can be more readily removed from the water. Some nanoparticles will be subject to biotic and abiotic degradation resulting in removal from the water.

Abiotic degradation processes that may occur include hydrolysis and photocatalyzed reaction in surface waters. Particles in the upper layers of aquatic environments, on soil surfaces, and in water droplets in the atmosphere are exposed to sunlight. Light-induced photoreactions often are important in determining environmental fate of chemical substances. These reactions may alter the physical and chemical properties of nanomaterials and so alter their behavior in aquatic environments. Certain organic and metallic nanomaterials may possibly be transformed under anaerobic conditions. Complexation by natural organic materials such as humic colloids can facilitate reactions that transform metals in anaerobic sediments (Nurmi et al., 2005). The concentration of nanomaterials in the suspensions can be as high as 100 ppm, but is more typically in the range of 10-50 ppm. The stability of particles and suspensions is sensitive to pH and ionic strength (Fortner et al., 2005).

Heterogeneous photoreactions on metal oxide surfaces are increasingly being used as a method for drinking water, wastewater and groundwater treatment. Semiconductors such as titanium dioxide and zinc oxide as nanomaterials have been shown to effectively catalyze both the reduction of halogenated chemicals and oxidation of various other pollutants, and heterogeneous photocatalysis has been used for water purification in treatment systems.

Nanoparticle photochemistry is being studied with respect to its possible application in water treatment. Processes that control transport and removal of nanoparticles in water and wastewater are being studied to understand nanoparticle fate (Moore, 2006; Wiesner et al., 2006). The fate of nanosized particles is not well characterized. Nanosized particles are most likely to be affected by sorption processes and chemical reactions. The ability of either of these processes to immobilize or destroy the particles will depend on the chemical and physical nature of the particle and the residence times.

2.3.3. Environmental Applications of Nanoparticles

The high surface area of nanosized particles provides enhanced ability to sorb both organic and inorganic chemicals from environmental matrices compared to conventional forms of the same materials. This property can potentially be utilized to bind pollutants to enhance environmental remediation.

Nanoscale particles are typically more reactive than larger particles of the same material. This is true especially for metals and certain metal oxides. In the environment, nanomaterials have the potential to react with a variety of chemicals; their increased or novel reactivity coupled with their sorptive properties allows for accelerated removal of chemicals from the environment.

Nanoscale iron particles have been demonstrated to be effective in the in situ remediation of soil contaminated with tetrachloroetylene. A wide variety of pollutants are claimed to be transformed by iron nanoparticles in laboratory experiments, including halogenated methanes, chlorinated benzenes, chlorinated ethanes, dyes, and inorganic anions. Further investigations are underway with bimetallic nanoparticles (iron particles with Pt, Pd, Ag, Ni, Co or Cu deposits) and metals deposited on nanoscale support materials such as nanoscale carbon platelets and nanoscale polyacrylic acid (Zhang, 2003).

A challenge for environmental protection is to help fully realize the societal benefits of nanotechnology while identifying and minimizing any adverse impacts to humans or ecosystems from exposure to nanomaterials. In addition, we need to understand how to best apply nanotechnology for pollution prevention in current manufacturing processes and in the manufacture of new nanomaterials and nanoproducts, as well as in environmental detection, monitoring, and clean-up (EPA, 2007). Currently a wide variety of potential remedial tools employing nanotechnology are being examined at the bench-scale for use in waste water and soil remediation. One emerging nanotechnology, nanosized zero valent iron and its derivatives, has reached the commercial market for field-scale remediation and studies. Laboratory and field applications of nanoparticles for remediation purposes are given in more details in Chapter 3.

2.4. Transport of Contaminants in Groundwater

Interest in the transport and fate of the contaminants in subsurface environments developed as a result of concern for the protection and remediation of both ground- and surface-water resources. To achieve this protection, it is necessary to (i) predict the time of arrival and concentration of cotaminants at a receptor such as a monitoring well, a water supply, or a surface water body; (ii) design safe, cost-effective waste facilities, (iii) install effective monitoring systems, and (iv) develop efficient and cost effective strategies for remediation of contaminated aquifers. To attain these goals, the processes involved in the transport and transformation of contaminants in porous medium, and under either saturated or unsaturated conditions must be understood.

The fate and transport of contaminants in the groundwater system is controlled by several complex processes. The major processes controlling the transport of the contaminants in the aqueous phase are (i) advection, (ii) hydrodynamic dispersion (iii) adsorption and (iv) chemical/biological transformations.

Advection is the transport of the dissolved species with the average groundwater velocity. The average linear velocity, v, at which groundwater flows through a porous aquifer is defined using Darcy's Law:

$$v = - (K/ \theta_t) (dh/dx) \quad (2.48)$$

where K is the hydraulic conductivity of the formation in the direction of groundwater flow, θ_t is the porosity of the formation, and (dh/dx) is the hydraulic gradient in the direction of groundwater flow (Freeze and Cherry, 1979).

Hydrodynamic Dispersion is the spread of contamination around the average groundwater flow. It is represented mathematically in terms of Fick's Law:

$$F_{d,x}=-D (dC/dx) \quad (2.49)$$

where $F_{d,x}$ is the dispersive flux in the x direction, D is coefficient of hydrodynamic dispersion and dc/dx is the concentration gradient.

Hydrodynamic dispersion comprises of two different mechanisms: molecular diffusion and mechanical mixing. Hence, the coefficient of hydrodynamic dispersion can be defined as:

$$D = D_m + D_d \tag{2.50}$$

where D_m represents mechanical mixing and D_d is the effective molecular diffusion coefficient in porous media.

Mechanical mixing is the mixing of the contaminant resulting from movement through complex pore structures (Greenkorn, 1983). Mechanical mixing is caused by the non-uniform velocity distributions in porous media which is mainly due to (i) the velocity variations within a pore, (ii) different pore geometries, and (iii) the divergence of flow lines around the sand grains present in a porous medium (Gillham and Cherry, 1982). Hydrodynamic dispersion is mathematically defined using a Fickian-like expression where the constant, the coefficient of hydrodynamic dispersion, is defined as:

D_m has been found to be function of groundwater velocity through the porous media:

$$D_m = \alpha v \tag{2.51}$$

where α is the constant of proportionality and is known as the dispersivity parameter.

Molecular diffusion is due to concentration gradients and the random; Brownian motion of water molecules. It can be obtained from the diffusion coefficient in a water body (without a porous medium), D_o, by:

$$D_d = \tau D_o \tag{2.52}$$

where τ is the tortuosity of the medium. Tortuosity is a factor that accounts for the increased distance a diffusing ion must travel to get around the sand grains.

Adsorption of a substance involves its accumulation at the interface between two phases, such as a liquid and a solid, or a gas and a solid. The molecule that accumulates, or adsorbs, at the interface is called and adsorbate, and the solid on which adsorption occurs

is the adsorbent (Pontius, 1990). In groundwater applications, sorption of non-polar organics often can be treated as an equilibrium-partitioning process between the aqueous phase and the porous medium (Chiou et al., 1979).

The term of "Chemical/Biological Transformations" represents any biological or chemical transformations that the dissolved species undergoes as it travels through the porous media. It includes decay, as well as any reaction with other dissolved species or the soil minerals.

The classical mathematical approach used to describe the solute transport of a non-reactive conservative solute in porous media is the advection-dispersion equation, described in Equation 6.5.

$$\partial / \partial x \ (\mathrm{D}.\partial C / \partial x) - \mathrm{v}.\partial C / \partial x = \partial C / \partial t \qquad (2.53)$$

D is the dispersion coefficient, v is the groundwater velocity, C is the concentration of the solute, x is the spatial coordinate, and t is time. This equation is an expression of the mass balance of a contaminant within the aquifer as a result of advection and hydrodynamic dispersion.

Aquifer and groundwater remediation is becoming more important as easily accessible water supplies steadily decrease and demand continues to increase. Most of the remediation technologies available today, very often are costly and/or time consuming, particularly pump-and-treat methods. Advances in nanoscale science and engineering are providing unprecedented opportunities to develop more cost effective and environmentally acceptable water purification processes. Recent studies on the use of nanoparticles for decontamination of soil and groundwater is given in Chapter 3.3.

3. LITERATURE REVIEW

Widespread and improper use of phenols and chlorophenols in the industry for manufacturing polymers, solvents, mothproofing agents, miticides, germicides, algicides, fungicides, and wood preservatives pose a great risk for the environment in terms of contamination and adverse health effects on living organisms. Phenolic compounds used for these purposes mainly end up in soils, surface and groundwaters**.**

There has been much research into the removal of these compounds from contaminated sites and many treatment techniques have been reported for their destruction. The need to achieve a complete mineralization and produce less harmful intermediates has led to the development of new alternative technologies. Among these technologies, Advanced Oxidation Processes (AOP) are proven to be a promising field of study due to their ability to dismantle and completely mineralize a wide range of pollutants in short periods of time.

AOPs are based on the generation of powerful hydroxyl radicals that have the potential to render destruction and complete mineralization of organic compounds to carbon dioxide and water. One of the novel approaches of AOPs is the use of ultrasonic waves alone and in combination with other methods to degrade organic contaminants that cannot be destroyed by conventional treatment methods. The use of ultrasound in environmental applications has gained interest owing to the unique properties of ultrasound to induce sonochemical effects (Ince et al., 2001).

Nanoparticles have also been presented to be effective for remediation of contaminated groundwater. The use of zero-valent iron (ZVI) for the remediation purposes has received utmost attention due to its ability to generate a reaction similar to that of Fenton and enhance the reaction rates causing catalytic effects (Chung et al., 2006).

This chapter consists of a literature review addressing results of those studies related to the destruction of phenolic compounds.

3.1. Destruction and Removal of Phenolic Compounds by AOPs

Aqueous solutions of Fenton's reagent (Fe^{2+} + H_2O_2) have been used by Pelizzetti et al. (1987) to determine the decomposition of the following chlorophenols: 2-chlorophenol, 3-chlorophenol, 4-chlorophenol, 3,4-dichlorophenol and 2,4,5-trichlorophenol. The mineralization of these chlorinated aromatic substrates to CO_2 and free Cl^- has been studied as a function of [Fe^{2+}] and [$HClO_4$]. They found that increasing the concentration of Fe^{2+} enhanced the decomposition process, while an increase in the concentration of $HClO_4$, inhibited the reaction. They also showed that the presence of Fe^{3+} alone (without any Fe^{2+}) with H_2O_2 had no effect on the degradation of the chlorophenols. In all cases, the stoichiometric quantity of free Cl^- was obtained at the completion of the decomposition reaction; but the rates of disappaearance of the chlorophenol and of the formation of the Cl^- were not similar.

Benitez et al. (2000) studied the chemical decomposition of aqueous solutions of various chlorophenols (4-chlorophenol(4-CP), 2,4-dichlorophenol (2-DCP), 2,4,6-trichlorophenol (2,4,6-TCP) and 2,3,4,6-tetrachlorophenol (2,3,4,6-TeCP)) by means of single oxidants (hydrogen peroxide, UV radiation, Fenton's reagent and ozone at pH 2 and 9), and by the Advanced Oxidation Processes (AOPs) constituted by combinations of these oxidants (UV/H_2O_2, UV/Fenton's reagent and O_3/UV). For all these reactions the degradation rates were evaluated by determining their first-order rate constants and the half-life times. They found that ozone was more reactive with higher substituted chlorophenols while •OH radicals reacted faster with those chlorophenols having lower number of chlorine atoms. The improvement in the decomposition levels reached by the combined processes, due to the generation of the very reactive hydroxyl radicals, in relation to the single oxidants was demonstrated and evaluated by kinetic modeling.

Haertel et al. (2001) investigated photochemical advanced oxidation processes utilizing the combinations of UV/H_2O_2 and the photo-Fenton reaction for the degradation of p-chlorophenol. The study showed that the photo-Fenton process was the most effective treatment process under acidic conditions and produced a higher rate of degradation of p-chlorophenol at a very short radiation time. The reaction was found to follow first order kinetics. They demonstrated that pH, H_2O_2 concentration, the amount of the iron catalyst

and the type of the iron salt influenced the reaction rates. The experimental results showed that the optimum conditions were obtained at a pH value of 3, with 0.03 mol L^{-1} H_2O_2, and 1 mmol/l Fe(II) for the UV/H_2O_2/Fe(II) system and 0.01 mol L^{-1} H_2O_2 and, 0.4 mmol L^{-1} Fe(III) for the UV/H_2O_2/Fe(III) system. The reactions were accompanied by the generation of Cl which reached its maximum value at a short reaction time when using the photo-Fenton process. They concluded that the photo-Fenton process reduced the energy consumption by at least 73 to 83% compared with the UV/H_2O_2 process (Haertel et al., 2001).

In their study, Song-hu and Xiao-hua (2005) compared the degradation of various chlorophenols by electro-Fenton method. Using pentachlorophenol (PCP) as the model compound, they investigated the effects of cell voltage, electrolyte concentration and pH to optimize the degradation conditions. It was noted that the addition of small quantities of Fe^{3+} or Fe^{2+} significantly accelerated the degradation rate. Under the optimal conditions, electro-Fenton method was used to treat various chlorophenols including PCP, 4-chlorophenol (4-CP), 2,4-dichlorophenol (2,4- DCP), 2,4,6-trichlorophenol (2,4,6-TCP) and their mixture aqueous solutions. Their pseudo first-order degradation rate constants were found to be in the following sequence: 2,4-DCP > 2,4,6-TCP > PCP > 4-CP. The relationship between the chlorine content and degradation rate was discussed and compared with other advanced oxidation processes.

Loung-Chen et al. (2005) conducted a study on the response of 2,4,6-trichlorophenol (1)1,2,3,4,5-tetrachloro-phenol (2) and 4,5-dichloroguaiacol (3) toward advanced oxidation processes, such as UV-, O_2/UV-, H_2O_2/UV-, O_3/UV- and O_3–H_2O_2/UV-photolyses with irradiation of 254 nm photons. The studies were extended to treatment of these compounds with ozonation and O_3–H_2O_2 oxidation systems in alkaline aqueous solution. Except for the O_2/UV-photolysis of 1 and H_2O_2/UV-photolysis of 2, the dechlorination of 1–3 by O_2/UV- and H_2O_2/UV-potolyses were less effective than the corresponding N_2/UV-potolysis of 1–3. The dechlorination of 2 by treatment with O_3 alone was found to be slightly more effective than the corresponding O_3/UV-photolysis, whereas the dechlorination of 2 by treatment with the combination of O_3 and H_2O_2 was slightly less effective than the corresponding O_3–H_2O_2/UV-photolysis. In contrast, the dechlorination of 3 on treatment with O_3 alone was slightly less effective than the corresponding the O_3/UV-

photolysis, whereas the dechlorination of 3 on treatment with the combination of O_3 and H_2O_2 was slightly more effective than the corresponding the O_3–H_2O_2/UV-photolysis.

Sung and Huang (2007) studied the degradation of 2-chlorophenol by ozonation at pH 3 and investigated the byproduct distribution during ozonation. In this study, transient distribution of degradation products, in a semi-batch reactor under three ozone dosages were identified. An empirical degradation pathway was proposed to describe the ozonation reaction. They developed a mathematical protocol to solve and optimize the kinetic parameters. Modeling results revealed that the empirical pathway was capable of predicting the ozonation reaction at the beginning phase under a higher ozone dosage. The degree of agreement between predicted and experimental data decreased as the ozone dosage decreased. Results suggested that there was a dosage-dependent pathway in the direct ozonation of 2-chlorophenol.

3.2. Destruction and Removal of Phenolic Compounds by Ultrasound

Wu et al. (1996) studied the decomposition of 2-chlorophenol (2-CP) in aqueous solution with ultrasound and H_2O_2. The experiment was conducted with a sonicator (Microson XL-2020) operated at 20 kHz. The initial concentration of aqueous 2-CP solution was 100 mg L^{-1}, treated in the system with 0, 100, 200 and 500 mg L^{-1} H_2O_2 individually. The results showed the decomposition of 2-CP was effective at increased amplitude of ultrasound and concentration of H_2O_2, and smaller pH. At reaction duration 360 min, 2-CP decomposition with 500 mg L^{-1} H_2O_2 was found with 57% improvement over the control without H_2O_2 addition. The pH, controlled below the pKa of 2-CP (8.49 at 25°C), had significantly better decomposition of 2-CP than at greater values. The removal of total organic carbon was found to be only 63%. From the analysis of the experimental results, the data on 2-CP decomposition appeared to follow pseudo-first-order reaction kinetics.

Gaw-Lin and Shih-Ma (2000) investigated the effect of H_2O_2 and Fe^{2+} dosages on the decomposition of 2-CP using a coupled ultrasound/Fe^{2+}/ H_2O_2 process. They showed that the extent of 2-CP decomposition and mineralization depended on the dosages of $H_2O_2$and

Fe^{2+}. More than 99% of 2-CP was decomposed and 86% of 2-cp was mineralized using the ultrasound/ Fe^{2+}/ H_2O_2 process at Fe^{2+} of 10 mg L^{-1} and H_2O_2 of 500 mg L^{-1}. They also monitored the oxidation reduction potential (ORP) to determine the decomposition efficiency of 2-CP. There was a slight increase in the ORP values with increasing Fe^{2+} dosages, and an apparent increase with increasing H_2O_2 dosages was observed. They concluded that the major intermediate formed during the decomposition of 2-CP was 2-chloro-*p*-benzoquinone, which readily decomposed using the coupled ultrasound/ Fe^{2+}/ H_2O_2 process.

Wu et al. (2001) studied the photosonochemical degradation of phenol in water. They used the combination of ultrasound (US) and photochemistry to degrade an aqueous solution of phenol. They showed that the proposed combination was considerably more effective than ultrasound or ultraviolet (UV) light alone. They also showed that the combinative use of ultrasound and ultraviolet light had a synergistic effect on total organic carbon (TOC) removal. Identification of the first intermediates of the reaction (hydroquinone, catechol, benzoquinone and resorcin) indicated that •OH radicals were involved in the photosonochemical degradation mechanisms. The effect of operational parameters such as pH, saturating gases, and Fe^{2+} on the photosonochemical degradation rates has been studied. They showed that lower pH values and higher concentration of dissolved oxygen favored the phenol degradation and that the presence of Fe^{2+} enhanced TOC removal of phenol solutions.

Ma et al. (2005) showed that the decomposition rates of several monochlorophenols by sonolysis were enhanced by the presence of hydrogen peroxide. An optimum concentration of hydrogen peroxide was observed for achieving maximum sonolysis rate of monochlorophenols. The decomposition rates of 3-chlorophenol by sonolysis were higher than those for 2- and 4- chlorophenol for most experiments conducted, suggesting that the ring structure of 3-chlorophenol provided more sites available for free radical attack. They concluded that the temporal decomposition behavior of monochlorophenol in aqueous solutions was markedly influenced by the species distribution and the volatility of specific monochlorophenols.

Tarr et al. (2005) studied the sonochemical degradation of phenol using hydrogen atom scavengers CCl_4 and perfluorohexane. They showed that the first order rate constant for aqueous phenol degradation in separate experiments using different sonochemical probes increased in the presence of CCl_4 from 0.014 to 0.031 min^{-1} (probe 1) and from 0.022 to 0.061 min^{-1} (probe 2). They found that hydroquinone was the major reaction intermediate both in the presence and absence of hydrogen atom scavengers. They observed that hydroquinone yields were substantially higher in the presence of hydrogen atom scavengers and revealed that hydroxyl radical pathways for phenol degradation were enhanced by the hydrogen atom scavengers. Their study concluded that these additives could be useful in improving pollutant degradation efficiency or improving synthetic processes that rely on hydroxyl radical as a key intermediate.

In a review of Ince and Kidak (2006), the studies that are directly related with the use of ultrasound in decontaminating effluents with phenol residuals has been investigated and the main points of interest and problems encountered has been summarized. They reported that the optimum range for the frequency was found to be between 200 and 540 kHz in most of the studies. They also pointed out that the injection of mixtures of gases was preferred over injection of a single gas. They concluded that the use of ultrasound for destroying phenolic compounds is a promising approach as an environmental remediation technique.

Ultrasonic removal of phenol under irradiation at 20, 300 and 520 kHz was investigated by Ince and Kidak (2006) to assess the impacts of operating parameters on the efficiency of the reaction. It was found that 20 kHz was the least effective frequency for ultrasonic decomposition of phenol, owing to the low volatility of phenol and the slow rate of OH radical ejection to the bulk solution at this frequency. Assessment of relative rates of destruction and ultrasonic yields showed that maximum efficiency was accomplished with 300 kHz employed in a reactor enclosed with an ultrasonic energy of 14.7 W. The same reactor and frequency was found to provide maximum ejection of hydroxyl radicals to the solution. Impacts of pH and initial concentration on the efficiency of phenol removal were such that acidic pH and high concentrations accelerated the process as related to the increased likelihood of phenol at these conditions to approach the cavity sheath. Separate injection of equivalent volumes of air and argon into the reactors showed that the

decomposition was enhanced in the presence of air by virtue of the production of additional reactive species via the reaction of nitrogen with molecular oxygen.

The comparison of enhancement effect of pentachlorophenol sonolysis at 20 kHz by different dual-frequency ultrasonic irradiations has been investigated by Liao et al. (2006). The dual-frequency ultrasounds that were used in the study involved 20 kHz/40 kHz, 20 kHz/530 kHz, 20 kHz/800 kHz and 20 kHz/1040 kHz. It has been found that the highest rate of pentachlorophenol degradation was achieved at dual-frequency ultrasonic irradiation, compared to mono-frequency ultrasonic systems. The order of contribution to the enhancement effect of sonochemical degradation of pentachlorophenol at 20 kHz was found to be as follows: 530 kHz > 800 kHz > 40 kHz > 1040 kHz.

A review addressing photo-degradation of chlorophenols in the aqueous solution has been published by Czaplika (2006). The review presents the chlorophenols' photo-degradation kinetics and mechanism in the aquatic environment under UV–vis in the presence of hydroxyl radicals and singlet oxygen. The influence of experimental parameters such as pH, dissociation degree, presence of oxidants in solution, number and position of Cl atoms on the quantum yield and reaction rate constant of chlorophenols were discussed. Mechanisms of photolysis, reaction with hydroxyl radicals, singlet oxygen and secondary reactions for mono-, di-, tri-, tetra- and pentachlorophenol were proposed. The pathways for intermediate reactions such as dechlorination, oxidation, dimerization for chlorophenols were also presented.

3.3. Destruction and Removal of Phenolic Compounds and Groundwater Contaminants by Nanoparticles

Chlorinated solvents have been shown to biodegrade in-situ by a variety of investigators (Mohn and Tiedje, 1992; Semprini et al.1992; Criddle et al., 1990; Tatara et al., 1993). The rate of degradation was found to be very slow. Weathers and Parkin (1995) have demonstrated that chlorinated solvent transformation was enhanced using methanogenic cell suspensions and iron fillings (zero-valent metals). Although the exact mechanism of this activity is unknown, O'Hannesin (1993) showed that the loss of PCE and TCE (86 % and 90 %, respectively) and the near stoichiometric increase in dissolved chloride and detection of chlorination products.

Wang and Zhang (1997) investigated the synthesis of nanoscale iron particles for rapid and complete dechlorination of TCE and PCBs. It was found that the TCE was completely dechlorinated by palladized commercial Fe powders (Pd/Fe) within 2 h, by the synthesized nanoscale Fe particles within 1.7 h, and by the synthesized nanoscale Pd/Fe bimetallic particles within less than 0.25 h. It was also shown that partial PCB reduction (<25%) was observed in the solution containing nanoscale Fe particles.

Klabunde et al. (1998) investigated the dechlorination of carbon tetrachloride by zinc-silver, zinc-palladium, and zinc-gold bimetallic systems. Reduction products detected were methane, ethylene, acetylene, and other hydrocarbons along with products of partial dechlorination such as chloroform, methylene chloride, and methyl chloride. They showed that the use of zinc dust doped with palladium, gold and silver resulted in 4-10 fold increases in carbontetrachloride degradation rate and conversion into methane.

A field demonstration was performed by Zhang and Elliott (2001) in which nanoscale bimetallic (Fe/Pd) particles were gravity fed into groundwater contaminated by trichloroethene and other chlorinated aliphatic hydrocarbons at a manufacturing site. This study showed that despite the low nanoparticle dosage, trichloroethene reductions efficiencies up to 96% were observed over a 4-week monitoring period.

Zhang and Lien (2001) examined the potential for using laboratory synthesized nanoscale Pd/Fe bimetallic particles to reduce chlorinated ethenes. They showed that the nanoscale bimetallic particles were very effective for complete dechlorination. They also demonstrated that the surface area normalized reactivity for the transformation of chlorinated ethenes was one to two orders of magnitude higher than those reported in the literature for commercial grade iron particles.

Lu et al. (2001) investigated the catalytic decomposition of hydrogen peroxide and 2-chlorophenol with iron oxides. Their study showed that the catalytic activity for hydrogen peroxide decomposition was the highest for granular ferrihydrite, less for goethite, and much less for hematite based on mass and surface area basis. However, the catalytic activity for 2-CP oxidation exhibited a converse series for these three iron oxides. Therefore, they proposed that hematite was the most likely to be involved in the degradation of contaminants in the subsurface environment. Furthermore, the oxidation efficiency of 2-CP was corresponding to the inverse sequence of specific area and pH of the iron oxides, suggesting a guideline on selecting materials as catalyst in application. They demonstrated that the extent of fluid segregation would affect largely on the decomposition kinetics of hydrogen peroxide. They concluded that the extent of mixing should be taken into consideration when applying such the Fenton-like reaction for in situ remediation or ex situ slurry reactor design.

Mallouk et al. (2002) used bimetallic nickel-iron nanoparticles for the hydrodechlorination of TCE to hydrocarbons. They showed that the dehalogenation of TCE was 50-80 times slower using nanoiron or iron filings. They also found that the final TCE degradation products were predominantly saturated hydrocarbons, such as, butane, hexane, and octane.

Zhang and Masciangioli, 2003 has demonstrated that nanoscale bimetallic particles such as iron/palladium, iron/silver, or zinc palladium, can serve as potent reductants and catalysts for a large variety of common environmental contaminants such as PCBs, organochlorine pesticides, and halogenated organic solvents.

In a study of Schrick et al. (2004) the transport of hydrophilic carbon (Fe/C) and polyacyrlic acid supported (Fe/PAA) zerovalent iron nanoparticles was studied by elution through columns packed with sand. They found that there was a dramatic difference in transport of unsupported and carbon-supported metal nanoparticles through sand columns. They reported that the unsupported Fe-Ni nanoparticles penetrated less than 1 cm into the column, where they agglomerated. In contrast, Fe-Ni supported on hydrophilic carbon has found to pass through the sand. They concluded that anionic support materials such as hydrophilic carbon and PAA inhibited agglomeration and significantly reduced the sticking coefficient of iron nanoparticles on sand. They also reported that 30-100 nm diameter nanoparticles had poor transport properties compared to particles that are 400-500 nm in diameter.

Zhao et al. (2004) studied the destruction of polichlorinatedbiphenyls (PCBs), perchloroethylene (PCE) and trichloroethylene (TCE) in Alabama soils and groundwater. They found that the degradation rate of TCE using new nanoparticles was orders of magnitude faster compared to the best reported Fe-based nanomaterials. No toxic intermediate by-products were detected. It was shown that 80% of PCBs in water solution was destroyed using the stabilized nano-materials within 100 hours.

In his study, Okinaka (2004) investigated the degradation of 1,1,1-trichloroethane (TCA) with reactive nanoscale iron product in simulated groundwater. He showed that the large reactive surface area of the nanoscale iron product reduced the high TCA concentrations with low treatment dosages. He found that the production of 1,1-dichloroethene, ethane, and ethane was not proportional to the degradation of TCA.

The degradation of the model pollutant phenol with hydroxyl radicals generated from zero-valent iron and hydrogen peroxide has been investigated by Bremner et al. (2006). The optimum conditions for degradation were found to be the continuous presence of iron metal, acidic pH and relatively concentrated hydrogen peroxide (9.5 M). They showed that when less stringent conditions were used, the products obtained from the decomposition were formed over a much longer timescale. The intermediates in the oxidation were identified as catechol, hydroquinone, benzoquinone, maleic acid and a relatively stable product, tentatively identified as an organic complex of iron and oxidised catechol.

Chung et al. (2006) investigated the application of nano-scale zero-valent iron particles for pentachlorophenol contaminated soil. They showed that when different content percentages of nano-scale zero valent iron (0, 0.2, 0.5 and 1 wt.%) and 1% H_2O_2 to initiate oxidation were used, 1 wt.% of zero-valent iron gained the best treatment result for the pentachlorophenol contaminated soil at 1000 mg kg^{-1}.

Wong et al. (2006) have used palladium-on-gold nanoparticles (Pd/Au) to catalyze the hydrodechlorination of trichloroethene in water. Their study focused on the improvement of the potential of this catalyst as a groundwater remediation technology by synthesizing Pd/Au nanoparticles with smaller diameters and immobilizing them on a solid support. They found that Pd/Au nanoparticles were considerably more active than Pd nanoparticles and conventionally synthesized Pd/Al_2O_3.

In the study of Dunphy et al. (2006), where the effect of pH on nanoparticle aggregation and transport in porous media was investigated, it was reported that nanoparticle aggregate size distributions were either bi- or tri-modal and as the pH approached the pH of zero charge, the aggregate sizes increased. They concluded that the extent of transport was influenced by the surface potential effects and the size of the nanoparticles.

Zhang et al. (2007) investigated the dechlorination of p-chlorophenol using Ni/Fe nanoscale particles. Their results demonstrated that the nanoscale Ni/Fe could effectively dechlorinate *p*-chlorophenol at relatively low metal to solution ratio of 0.4 g L^{-1}(Ni 5 wt%). The target with initial concentration of p-chlorophenol 0.625 mmol L^{-1} was dechlorinted completely in 60 minutes under ambient temperature and pressure. They showed that experimental parameters such as reaction temperature, pH, Ni loading percentage over Fe, and metal to solution ratio had a significant impact on dechlorination efficiency. The possible mechanism of dechlorination of p-CP was proposed and discussed. The activation energy of the dechlorination reaction was determined to be 21.2 kJ mol^{-1} at the temperature range of 287–313 K.

Suresh and Patel (2007) studied the dechlorination of chlorophenols. Dechlorination of PCP was found to be sequential and phenol was identified as the end product along with accumulation of trace concentrations of tetra- and trichlorophenols. Scanning electron microscopy and energy dispersive X-ray spectroscopy revealed that palladium in its metallic form (Pd^0) produced by reduction of Pd^{4+}, was spatially separated from magnesium granules when acid was included in the reaction. They showed that the colloidal palladium particles generated active reductive species of hydrogen and dechlorinated chlorophenols. They found that when there was no acid in the medium, the efficiency of dechlorination of PCP by Pd/Mg^0 system was very low and chief mechanism of removal of the compound was through sorption onto solid surfaces. They also showed that the rate and extent of removal increased with decrease in number of chlorine atoms on phenol. They concluded that (i) the Pd^0/Mg^0 was an efficient system for complete dechlorination of PCP all the way to phenol, (ii) the rate and extent of organic chloride removal followed the order: 2-CP > 2,4,5-TCP > PCP, (iii)Mg^0 in combination with in situ reduced palladium was more efficient in dechlorinating PCP as compared to Mg^0 in combination with ex situ reduced palladium, (iv) acid must be included in the system, to serve triple purposes of (a) corrosion of zero-valent metal and reduction of Pd^{4+} to Pd^0, especially while treating low concentrations of PCP, (b) provision of protons to produce H_2 and (c) retardation of formation of insoluble oxides and hydroxides that may sorb PCP and its dechlorinated products.

Mallouk et al. (2007) studied the transport of polymer-coated micro- and nanoiron particles in saturated porous media using polyelectrolyte mixtures. They reported that the sticking coefficients (defined as the probability that a particle-collector collision results in immobilization) increased with decreasing flowrate and decreased with increasing column length. They also studied the effect of polyacrylic acid (PAA) addition on the sticking coefficient and found that sticking coefficient decreased substantially as the PAA concentration increased.

4. MATERIALS AND METHODS

4.1. Materials

4.1.1. Chemicals Used in Batch Experiments

The test compounds phenol (99 % pure, as solid) and 2-chlorophenol (98 % pure) were purchased from Merck and Fluka, respectively. Water used for the preparation and dilution of the samples was produced from deionized water using a Millipore Milli-Q gradient apparatus. The molecular structures and physical/chemical properties of the test compounds are given in Figure 4.1 and Table 4.1, respectively.

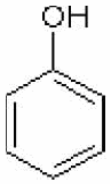

Phenol

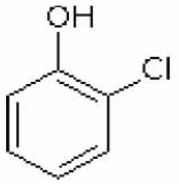

2-Chlorophenol

Figure 4.1. Molecular structures of phenol and 2-chlorophenol used in the experiments.

Table 4.1. Properties of the model phenolic compounds used in the experiments.

Chemical Properties	Phenol	2-Chlorophenol
Molecular Formula	C_6H_6O	C_6H_5ClO
Molecular Weight (g mol^{-1})	94.11	128.56
Melting Point (°C)	43	9.3
Boiling Point (°C)	181.7	174.9
Density (g cm^{-3}) at 20 °C	1.06	1.26
Dissociation constant at 25°C	9.99	8.48
Solubility in water (mg L^{-1}) at 25°C	82.000	28.000
Vapor pressure (10^{-2} mm Hg) at 25°C	62	1.42
Octanol/Water Partition Coefficient (log K_{ow})	1.37-1.75	2.15-2.25

Dichloromethane obtained from Merck was used as the solvent for liquid-liquid extraction of phenol. Analytical grade sodium hydroxide (NaOH), sulfuric acid (H_2SO_4) and hydrochloric acid (HCl) at various concentrations used for pH adjustment were obtained from Merck.

Nanoparticles in powder form and in suspension were used in combination with ultrasound. The particles used in these experiements are listed below:

(i) Ultrasound combined with nanoparticles in powder form:

- Fe (II, III) Oxide Nanoparticles (98 % purity, Aldrich, Istanbul).
- Fe Ni Oxide Nanoparticles (98 % purity, Aldrich, Istanbul).
- Ti (IV) Oxide Nanoparticles (99.7 % purity, Aldrich, Istanbul).
- Copper (II) Oxide Nanoparticles (Sigma-Aldrich, Istanbul).

(ii) Ultrasound combined with particle suspensions:

- Reactive Nanoscale Iron Particles (RNIP) (Toda Kogyo Corp, Japan).
- MD24 Superparamagnetic Iron Oxide Nanoparticles (Koç University, Istanbul).
- Fe^{2+} suspension, prepared by using reagent grade Iron (II) Sulfate Heptahydrate, $FeSO_4.7H_2O$ (Merck, Germany).
- Cu^{2+} suspension, prepared by using reagent grade Cupric Sulfate, $CuSO_4.5H_2O$ (EMD Chemicals, Germany).
- H-200 Zero Valent Iron (Hepure, USA).
- HC15 Zero Valent Iron (Hepure, USA).
- Ancor M-30/80 Zero Valent Iron (Hepure, USA).

H_2O_2 (35%w/w) was analytical Merck grade. Air, argon (Ar) and oxygen (O_2) were obtained from BOS Istanbul with >99% purity.

4.1.2. Chemicals Used in Continuous Flow Experiments

The 60/70 AFS type of sand used for continuous flow experiments was obtained from Siltaş, Istanbul. The chemical analysis of the sand is given in Appendix A. $CaCl_2.2H_2O$ (Merck) was used for the tracer mobility experiments. Three different superparamagnetic iron oxide nanoparticles (MD 24, MD 59 and MD 60, obtained from Koç University, Istanbul) coated with polyacrylic acid to prevent aggregation were used in these experiments.

4.1.3. Experimental Setup Used in Batch Experiments

4.1.3.1. Ultrasonic Reactors. The four different ultrasonic reactors used in the batch reactors are described below.

20 kHz probe inserted reactor (Reactor 1):

The system consists of a 100 mL glass cell surrounded by a water-cooling jacket to keep the reactor at constant temperature (25 ± 0.5 °C); a Bandelin sonoplus HD2200 a probe type transducer (probe tip area = 1.13 cm^2), emitting ultrasonic waves at 20 kHz and a 180 W generator. The horn was submerged 3 cm from the top of a reaction cell, which had an effective volume of 80 mL. The system was mounted in a polyurethane isolating material to prevent excessive noise. A photograph of the reactor is presented in Figure 4.2.

Figure 4.2. Photograph of Reactor 1.

300 kHz plate type reactor (Reactor 2):

The system (Undatim Ultrasonics-Belgium) consists of a 150 mL glass cell equipped with a water cooling jacket to keep its contents at constant temperature (25±0.5 °C), a 300 kHz frequency plate type piezoelectronic transducer (vibrational area = 9.6 cm^2) and a 25 W generator, which converts electrical power into ultrasonic energy. A photograph of the system is presented in Figure 4.3.

Figure 4.3. Photograph of Reactor 2.

520 kHz plate type reactor (Reactor 3):

The system (Undatim Ultrasonics-Belgium) consists of a 1200 mL glass cell equipped with a water cooling jacket to keep the reactor at constant temperature (25±0.5 ºC) , a stainless steel top cover, a 520 kHz frequency plate type piezoelectronic transducer (vibrational area = 22 cm^2) and a generator with a power capacity of 100 W. A photograph of the system is presented in Figure 4.4.

Figure 4.4. Photograph of Reactor 3.

3x520 kHz reactor (Reactor 4):

The system consists of a 2 L stainless steel hexagonal reactor and a power generator operating at 600 W (Undatim Ultrasonics-Belgium). Three piezoelectric transducers emitting at 520 kHz frequency are mounted on the lateral walls of the reactor. Quartz windows are located on the other three walls, in which UV lamps (253.7 nm, Philips, PL-L 18 W TUV) are mounted in front of each quartz panels outside the reactor. A photograph of the system is presented in Figure 4.5.

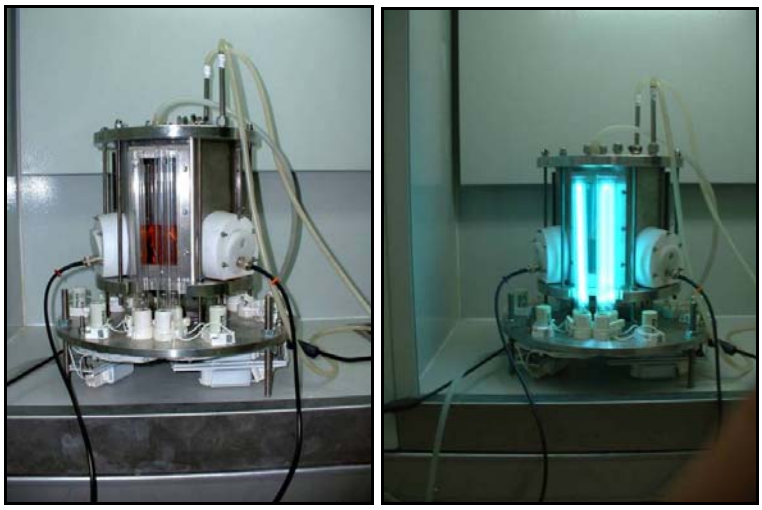

Figure 4.5. Photograph of Reactor 4.

4.1.3.2. Ozone Reactors.

Column Ozone Reactor:

Ozone was generated onsite from dry pure oxygen through an Ozonelab 100 Model (Ozone Service) generator for the ozonation, UV coupled ozonation and ultrasound coupled ozonation experiments. The photograph of the system is presented in Figure 4.6.

Figure 4.6. Photograph of the ozone reactor.

Ozone-UV Combined System:

To evaluate the combined effect of Ozone (O_3) and Ultraviolet light (UV), the column ozone reactor was integrated with a UV lamp. The photograph of the system is presented in Figure 4.7.

Figure 4.7. Photograph of O_3/UV reactor.

Ozone-Ultrasound Combined System:

In the ozone-ultrasound combined system, O_3 was injected into Reactor 2 through a Teflon tube. A scheme of the set-up is given in Figure 4.8.

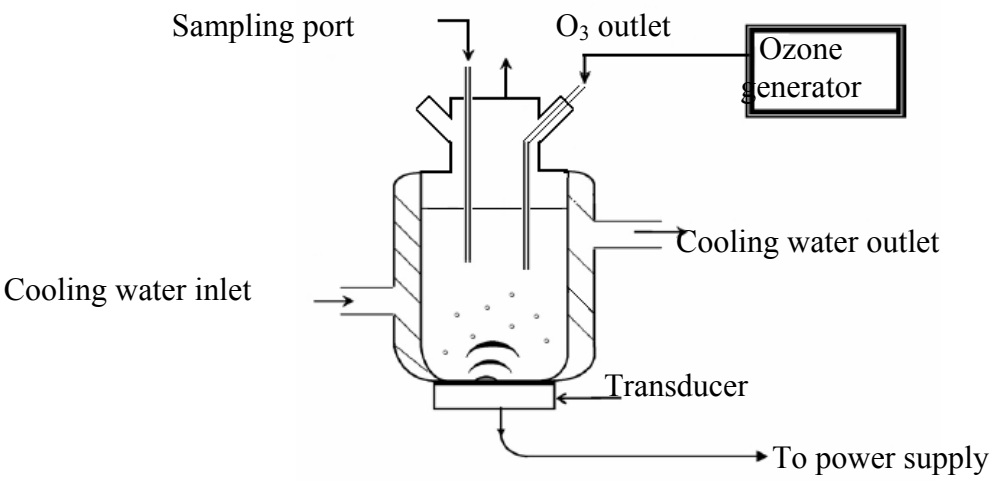

Figure 4.8. Scheme of ozone-ultrasound reactor.

4.1.4. Experimental Setup Used in Continuous Flow Experiments

Continuous flow experiments were performed using a two-dimensional tank (CF 1) and a vertical column (CF 2). Each of these two reactors is described below.

4.1.4.1. Continuous Flow Tank (CF 1). The continuous flow experiments were carried out in a plexy glass reactor tank divided into three compartments. The dimensions of the tank are as follows: 60 cm length, 5.5 cm width and 30 cm height. There was an inlet from which the Milli-Q water or the nanoparticle solution was fed into the reactor and an outlet from which the samples were withdrawn. The flowrate of the system was adjusted to a constant value of 16 mL min^{-1} throughout the experiments. The solutions were fed to the system through a peristaltic pump obtained from Watson Marlow. The photograph of the tank is presented in Figure 4.9.

Figure 4.9. Photograph of CF 1.

The tank was filled with soil by adding incrementally 5 cm of sand. After placing each sand layer in the tank, the soil was compacted uniformly by the repetitive application of a specific weight, a standard procedure to achieve homogeneous soil compaction. The same procedure was also followed each time the tank is filled to achieve near uniform conditions between the different experiments. The tank filled with sand is then saturated with Milli-Q water at a constant flowrate before the mobility experiments are conducted. Once saturated, the flow through the tank is close to 2-dimensional flow in a homogeneous unconfined aquifer.

4.1.4.2. Continuous Flow Column (CF 2). Continuous flow experiments were also carried out in a Chromaflex ® Standard Chromatography Column, 30 cm long and having an inner diameter of 4.8 cm (from Cole Parmer, USA). The column was filled by adding 1 cm sand layers and applying a downward force on the sand surface by a specific weight, a standard procedure to obtain a constant compaction throughout the column. The same procedure was also followed each time the column was filled to achieve uniform conditions for each experiment. The column filled with sand is then saturated with Milli-Q water at a constant upward flow with a flowrate of 1 mL min^{-1} before the mobility experiments are conducted.

A small flow rate was used in saturating the column to prevent air entrapment within the soil.

During saturation and the mobility experiments, Milli-Q water and nanoparticle solutions were fed to the system through a peristaltic pump obtained from Cole Parmer. The photograph of the column is presented in Figure 4.10.

Figure 4.10. Photograph of CF 2.

4.2. Methods

4.2.1. Methods for Batch Experiments

4.2.1.1. Preparation of the Test Solutions. Stock phenol and 2-chlorophenol solutions of 15 mM were prepared in Milli-Q water and stored at 4ºC in the dark. Test samples of 75,

150, 300, and 450 μM of phenol and 2-chlorophenol made from the stock using Milli-Q water.

4.2.1.2. Procedure for Sonication Experiments. All test solutions were bubbled with argon for 30 min prior to sonication and the gas was injected at a flow rate of 0.5 L min^{-1} throughout the sonication time (60 min) to enhance cavitation. Samples were withdrawn from the reactors every 10 min for GC analysis. The molar concentrations of phenol and 2-chlorophenol were estimated from the calibration curves plotted with five data sets using fixed concentrations of phenol and 2-chlorophenol.

4.2.1.3. Procedure for Single, UV-coupled and US-coupled Ozonation Experiments.

1. Single: Ozone was injected into the column at a flow rate of 0.75 L min^{-1} and the reactor was continuously mixed with a magnetic stirrer. Samples were withdrawn from the reactor every 10 min for GC analysis. The concentration of phenol and 2-chlorophenol was estimated from the related calibration curves.
2. UV-coupled: A UV lamp emitting monochromatic light at 253.7 nm was immersed through the ozone reactor and ozone was injected at a flow rate of 0.75 L min^{-1} during irradiation and continuous mixing with a magnetic stirrer. Samples were withdrawn at every 10 min for GC analysis.
3. US-coupled: These experiments were carried out in Reactor 2 and no extra gas injection was applied except for ozone at a flow rate of 0.75 L min^{-1}. Samples were withdrawn from the reactor at every 10 min for GC analysis.

4.2.1.4. Procedure for Sonication Coupled with Particles. These experiments were performed with 2-chlorophenol and in Reactor 2 only. The combinative effect of ultrasound coupled with micro or nanoparticles on the degradation of 2-chlorophenol was tested by sonicating the test solutions in the presence of these particles at various concentrations. Several experiments were also carried out by adding hydrogen peroxide to the reactor. The pH of the solutions was adjusted to 3 after particle addition. Samples were withdrawn from the reactor every 10 min for the GC analysis. When the particles were in powder form, the samples were first filtered through Millipore 0.45 μm syringe filters before the GC analysis.

4.2.1.5. Procedure for Batch Adsorption Tests. The adsorption experiments of 2-chlorophenol on nanoparticles were performed in 50 mL Erlenmeyer flasks shaken at 100 RPM and 25 ºC. A Memmert SV 1422 horizontal shaker was used in all experiments. Adsorption isotherms were determined using the equilibrium data obtained with different masses of nanoparticles contacted with 150 μM of 2-chlorophenol.

4.2.2. Methods for Continuous Flow Experiments

4.2.2.1. Preparation of the Nanoparticle Suspensions. Different concentrations of nanoparticles were prepared by diluting from the stock nanoparticle solutions using Milli-Q water.

4.2.2.2. Adsorption Experiments. For the determination of adsorbability of the nanoparticles used in the mobility experiments on sand, batch adsorption experiments were carried out in 50 mL flasks shaken at 100 RPM and 25 ºC in the Memmert SV 1422 horizontal shaker. Different masses of nanoparticles were contacted with fixed ratios of sand and water, equal to the sand/water ratios in the continuous flow tank and column after compaction, and the mixture was agitated. Initial and final concentrations in adsorption flasks were measured. To evaluate the rate of sorption, samples were also withdrawn from the flasks for analysis after 1 hour and 24 hours of agitation.

4.2.2.3. Mobility Experiments. The mobility experiments were run to investigate the mobility of nanoparticles in porous media and to compare the transport of the nanoparticle solutions with that of the tracer, $CaCl_2.2H_2O$. Different nanoparticle concentrations and different velocities were used to determine their effect on the mobility of the nanoparticles.

The flowrate in the continuous flow tank was adjusted to a constant value of 16 mL min^{-1} throughout the experiments, which corresponds to a velocity of about 6 m d^{-1}. Flow in the tank was 2 dimensional in a vertical plane, equivalent to uniform flow in an unconfined aquifer. Samples were taken from the outlet every five minutes and analyzed

for conductivity in the case of the tracer experiment and for iron content and nanoparticle size analysis in the case of the nanoparticle mobility experiment.

Flow through the column was maintained constant at 2.4 mL min^{-1} for an average velocity of about 5.5 m d^{-1}. The tracer solution and nanoparticle solution were fed into the column from below to prevent having an instable interface between the resident water and injected nanoparticle solution which is slightly denser than 1. As opposed to the continuous flow tank where flow is 2-dimensional and unconfined, flow in the column was one dimensional and confined (pressured). Samples were taken every five minutes for conductivity and iron analysis.

4.3. Analytical Methods

Gas Chromatographic (GC) Analysis:

Phenol and 2-chlorophenol samples were analyzed using an Agilent 6890N gas chromatograph. The system was equipped with an auto-injector, which works either in split or splitless mode. Chromatographic separations were achieved on a HP5 capillary column. The column had a length of 30 m, an inner diameter of 250 μm and was coated with a stationary phase film of 0.25 μm. The detector was flame ionization detector (FID) and it was heated to 300 ºC. Helium was used as the make-up and carrier gas at the splitless mode with a flow rate of 25 cm s^{-1}. The analysis method was built on Environmental Protection Agency (EPA) methods 604 and 8270, which are proposed for the determination of phenols in water (EPA, 2005a; EPA, 2005b). The inlet temperature was 240 ºC and detector temperature was 300ºC. The oven temperature was held at 40 ºC for 1 min, increased to 140 ºC at 10 ºC/min and then increased to 260 ºC at 20 ºC min^{-1}.

Samples were prepared by extracting 1.0 mL aqueous phenol and 2-chlorophenol solutions with 0.5 mL dichloromethane in 2 mL closed vials for 3 minutes and 2 μL of the dichloromethane phase was injected with an Agilent 7683 auto-injector. A series of phenol and 2-chlorophenol solutions were injected to the GC, to achieve calibration curves and these curves were used for the quantification of phenol and 2-chlorophenol as presented in

Figure B1 and Figure B2 in Appendix B. Concentrations were measured using the total area under each peak together with the calibration curves. The GC method separated individual phenolics and thus could provide greater accuracy than the 4-aminoantipyrine method (Neufeld and Paladino, 1985).

Total Organic Carbon (TOC) Analysis:

Total organic carbon (TOC) was monitored by a Shimadzu TOC-V CSH analyzer operating in the non-purgeable organic carbon (NPOC) mode. The instrument was calibrated by standard solutions of KHP (1-10 ppm). Samples were acidified with HCl to pH 1-2 and purged for 1.5 min prior to injection with instrument grade air to ensure that all carbonate, bicarbonate and carbonic acid are removed as carbon dioxide (in gas form) from the solution. All samples were measured in triplicate.

Hydrogen Peroxide (H_2O_2) Analysis:

The concentration of hydrogen peroxide was monitored determination was determined by KI method described by Klassen et al., (1994). The method is based on the reaction of (I^-) with H_2O_2 to form triiodide (I_3^-), which has a strong absorbance at 351 nm. The analysis of H_2O_2 at concentrations as low as 1 mM is possible by determining the yield of I_3^- formed when H_2O_2 reacts with KI in a buffered solution containing ammonium molybdate tetrahydrate as a catalyst. Two sample solutions (A and B) were prepared as described below and 2.5 mL of each was mixed with one another and 1.0 mL of sample to record the absorbance at 351 nm. The calibration curve for H_2O_2 determination is presented in Appendix C.

Solution A: 33 g of KI, 1 g of NaOH and 0.1 g of ammonium molybdate tetrahydrate diluted to 500 mL with Milli Q water. The solution was stirred for 1 h to dissolve the molybdate. It was kept in dark in order not to cause I^- to oxidize.

Solution B: 10 g of potassium hydrogen phthalate was dissolved in 500 mL Milli Q water to act as the buffer solution.

Conductivity Analysis:

Conductivity analysis for the tracer mobility tests in the continuous flow tank and column was performed using a WTW LF 320 conductivity meter.

Nanoparticle Size Analysis:

Hydrodynamic size of the particles was measured with the Brookhaven 90 Plus Nanoparticle Size Analyzer, that is based on the Dynamic Light Scattering (DLS) technique (also known as Quasi Elastic Light Scattering (QELS) and Photon Correlation Spectroscopy (PCS)) (Brookhaven, http://www.brookhaven.co.uk/). This technique is used for measuring particle size over the size range of few nanometers to a few microns. When a beam of light passes through a colloidal dispersion, the particles scatter some of the light in all directions. When the particles are very small compared with the wavelength of the light, the intensity of the scattered light is uniform in all directions (Rayleigh scattering); for larger particles (above approximately 250 nm diameter), the intensity is angle dependent (Mie scattering). Therefore, time-dependent fluctuations in the scattered intensity are observed using a detector. These fluctuations arise from the fact that the particles are small enough to undergo random thermal (Brownian) motion and the distance between them is therefore constantly varying. Constructive and destructive interference of light scattered by neighbouring particles within the illuminated zone gives rise to the intensity fluctuation at the detector plane which, as it arises from particle motion, contains information about this motion. Analysis of the time dependence of the intensity fluctuation can therefore yield the diffusion coefficient of the particles from which, via the Stokes Einstein equation, knowing the viscosity of the medium, the hydrodynamic radius or diameter of the particles can be calculated.

Iron Content Analysis:

Perkin Elmer Optima 2100 Atomic Absorption Spectrometer is used for the determination of iron concentration in samples taken from mobility experiments. The spectrometer is equipped with a S10 model autosampler. ICP continuous technique was used for the analysis.

5. DETERMINATION OF ULTRASONIC POWER DENSITY

5.1. Background Information

An ultrasonic system transforms electrical power to vibrational energy, which is then transmitted into the sonicated reaction medium. Part of it is lost to produce heat, and another part produces cavitation. Not all of the cavitation energy produces chemical and physical effects; some energy is reflected and some is consumed in sound re-emission. Hence, there can be significant differences between the power supplied from the generator and that delivered into the reactor (Mason, 1999). Of the methods available to measure the amount of ultrasonic power entering a sonochemical medium, the most common and easiest is calorimetry, which is based on determination of the initial rate of heating when a system is irradiated by ultrasound (Mason, 1999). The method involves measurement of the temperature rise T against time for about 30 seconds using a thermocouple placed in the reaction vessel. From T versus t data, the rate of temperature rise dT/dt can be estimated by curve fitting the data to a polynomial in t, followed by computing the derivative of the curve at time zero. The ultrasonic power (P_d) actually entering the system can then be calculated by substituting the value of dT/dt into Equation 5.1 (Mason, 1999; Mason and Cordemans, 1998):

$$P_d = (dT/dt)\, C_p\, M \qquad (5.1)$$

where P_d= power dissipated in the system (W)

C_p = specific heat of water (4.184 J $g^{-1}{}^{o}C^{-1}$)

(dT/dt) = the rate of temperature rise at zero time ($^{o}C\ s^{-1}$)

M= mass of water in the reaction vessel (g)

The power calculated by the calorimetric method described above is used to determine the ultrasonic intensity (W cm^{-2}) or density (W mL^{-1}) in the reactor.

5.1.1. Evaluation of the Power Density in Reactor 1

The ultrasonic generator was operated at 10 %, 20 %, up to 70% of the total capacity (180 W). To avoid damage to the probe due to overheating, the highest applied power was 70 % of the total. The power input was determined in tap water using the calorimetric method, by which the increase in temperature against time at 30 s intervals was recorded during 4 minutes sonication of 80 mL water. The data are presented in Table 5.1.

Table 5.1. Temperature increase in Reactor 1 during sonication for 4 minutes without cooling under varying power inputs.

Time, s	**Power Input, %**						
	P= 10%	**P=20%**	**P=30%**	**P=40%**	**P=50%**	**P=60%**	**P=70%**
	Temperature, ^{o}C for 80 mL Sample Volume						
0	18.0	22.0	21.0	23.0	21.0	22.0	23.0
30	21.0	25.0	25.0	26.5	26.0	27.0	28.5
45	22.0	26.5	26.5	29.0	28.0	29.5	31.0
60	22.0	28.0	28.0	30.5	30.5	32.0	33.0
90	23.0	30.5	31.0	34.0	35.0	37.0	38.0
120	24.5	33.5	34.0	38.0	39.0	42.0	43.5
150	25.0	36.0	37.5	42.0	43.0	47.5	50.5
180	27.5	39.0	40.5	45.5	47.5	51.5	55.0
210	28.0	41.50	43.0	49.0	51.5	55.5	58.0
240	30.5	44.0	47.0	53.5	55.0	59.5	63.0

The plot of T versus time (Figure 5.1) provided an estimate of the rate of temperature rise (dT/dt) via fitting of the best polynomial to the observed data set. The value of dT/dt was estimated from the slope of the fitted curves and summarized in Table 5.2.

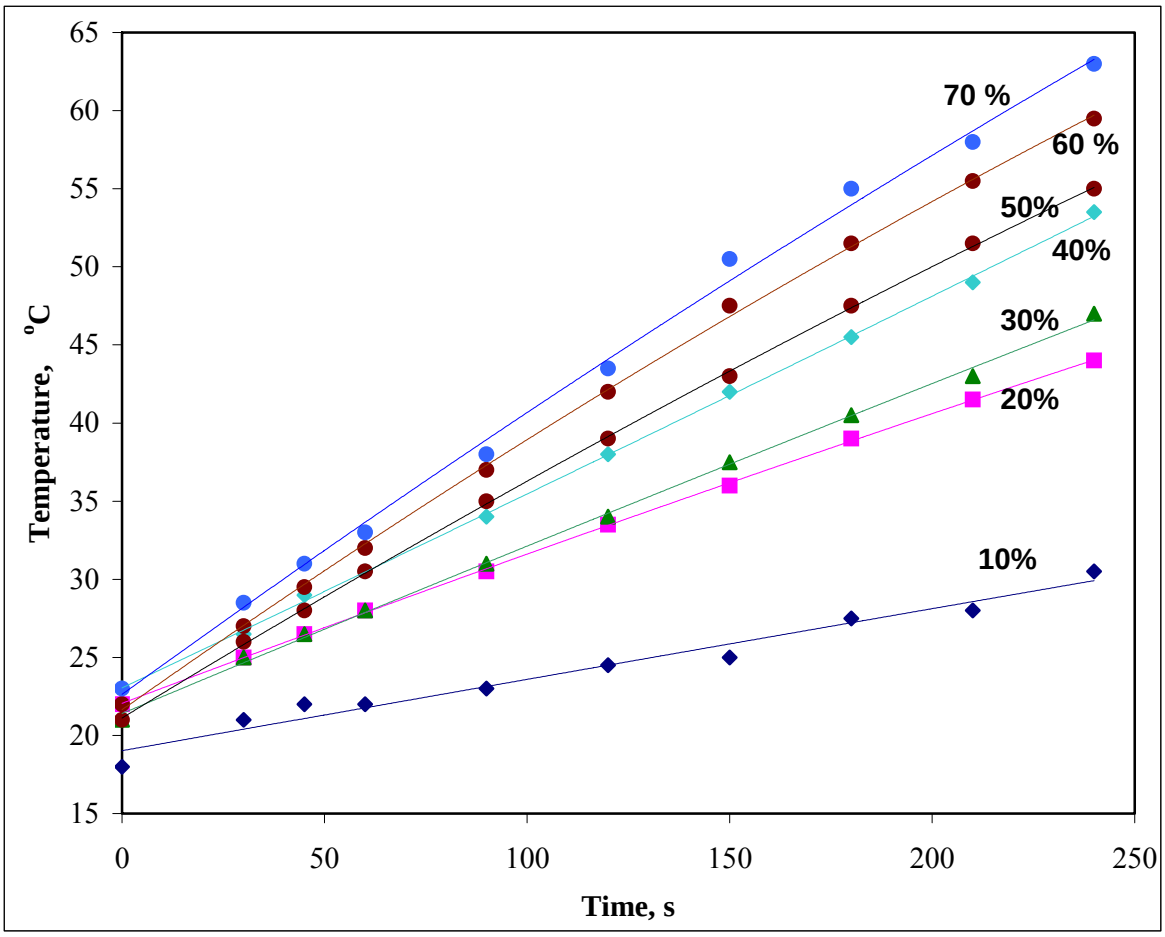

Figure 5.1. Rates of temperature rise during 4 minutes sonication of tap water at various power inputs and the best fit polynomials.

Table 5.2. Estimated values of dT/dt from the slopes of the fitted curves in Figure 5.1.

Applied Power (as % of Maximum-180 W)	P= 10%	P=20%	**P=30%**	P=40%	P=50%	P=60%	P=70%
dT/dt (°C/s)	0.046	0.099	**0.111**	0.126	0.157	0.180	0.184

Values listed in Table 5.2 were used in Equation 5.1 for estimating the power dissipated in solution, as presented in Table 5.3.

Table 5.3. The dissipated power in solution at various generator outputs.

Applied Power (as % of 180 W)	P= 10%	P=20%	**P=30%**	P=40%	P=50%	P=60%	70%
Power in solution (W)	15.4	33.0	**37.3**	42.1	52.4	60.2	61.6
Power in solution as % of supplied power	85.5	91.7	**69.7**	58.5	58.2	55.7	48.9

The relation between the applied power and the power density in solution P_{dt} ($P_{dt}=P_{ap}/V$) is given in Figure 5.2.

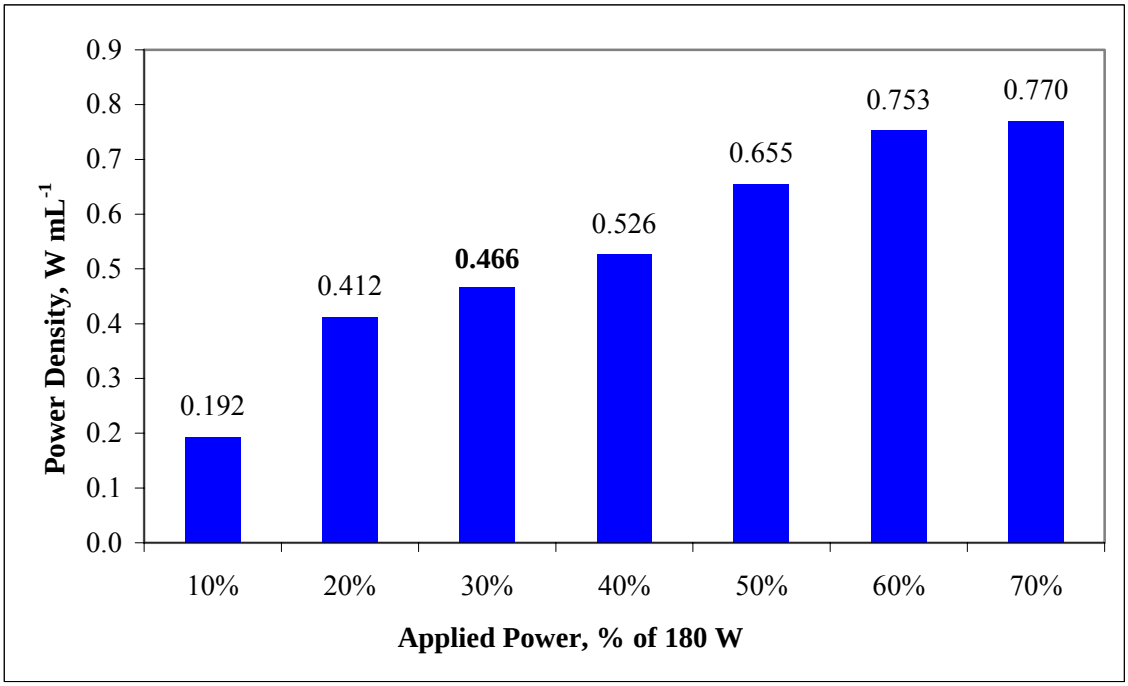

Figure 5.2. Power density as a function of applied power.

Calorimetric determination of P_{dt} was repeated using three other reaction volumes (other than 80 mL), and the results are tabulated in Table 5.4. The selected power and volume for the system are 80 mL and 54 W (30%), respectively that corresponds to dissipation of 37.3 W in solution.

Table 5.4. Power dissipation P_d (W) for various solution volumes.

Generator Power (W)	**70 mL**	**80 mL**	**90 mL**	**100 mL**
18.00 (10%)	14.1	15.4	17.8	19.6
36.00 (20%)	31.6	32.9	33.7	36.5
54.00 (30%)	38.6	**37.3**	39.8	43.9
72.00 (40%)	44.0	42.1	44.4	47.7
90.00 (50%)	50.2	52.4	53.8	56.7
108.00 (60%)	59.2	60.2	63.6	65.9
126.00 (70%)	63.5	61.6	66.2	69.4

5.1.2. Evaluation of the Power Density in Reactor 2

Temperature increase in Reactor 2 during sonication for 5 minutes without cooling under varying power inputs is presented in Table 5.5.

Table 5.5. Temperature increase in Reactor 2 during sonication of tap water for 5 minutes without cooling at 25 W generator output.

t (s)	0	30	60	90	120	150	180	210	240	270	300
T (^{o}C)	16	17.5	18.5	20	21	22	23	24	25	25.5	26.5

The plot of T versus time (Figure 5.3) provided an estimate of the temperature rise (dT/dt) via fitting of a polynomial to the observed data set. The value of dT/dt was 0.0454 °C s^{-1} from the fitted curve.

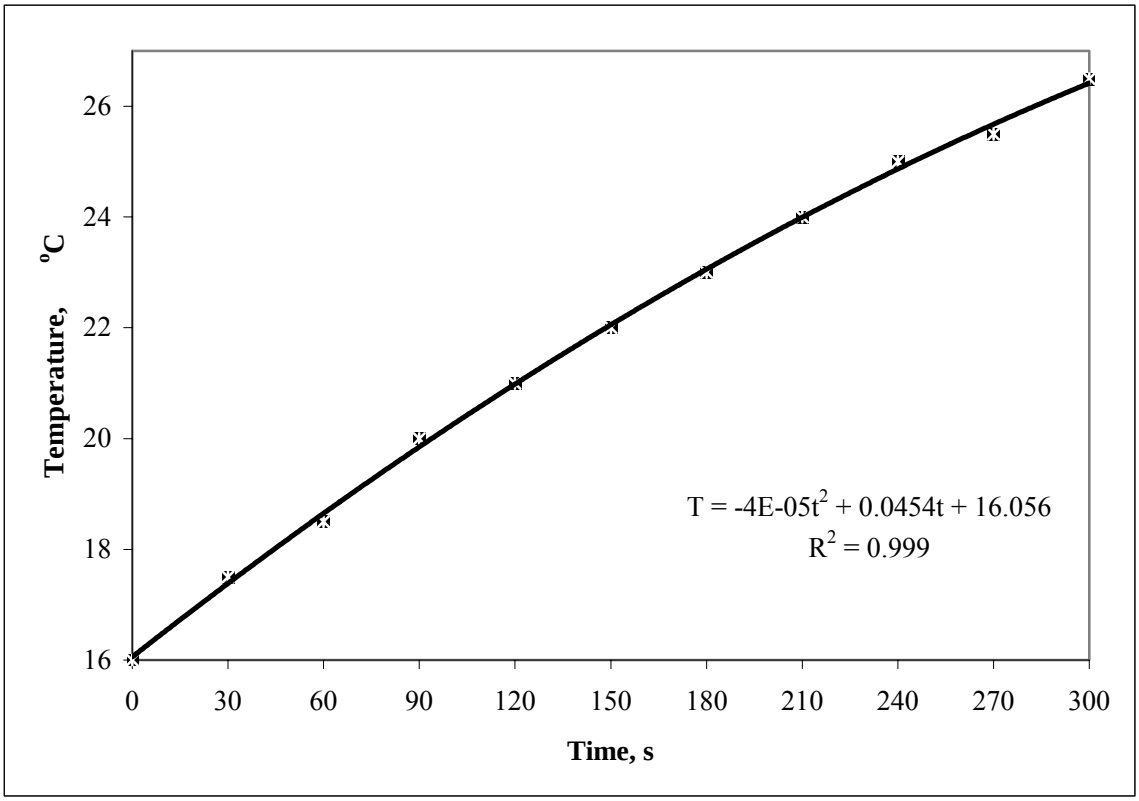

Figure 5.3. Temperature rise during 5 minutes sonication of 100 mL tap water at 25 W generator output.

The power in solution was calculated using Equation 5.2:

$$P_d = 0.0454 \frac{^oC}{\text{sec}} \times 4.182 \frac{J}{g\,^oC} \times 100g = 18.986 \text{ W} \quad (5.2)$$

The dissipated power P_d was also found using different volumes (other than 100 mL) as tabulated in Table 5.6. The maximum dissipation power of Reactor 2 is 19 W which

corresponds to an input power of 25 W and a reactor volume of 100 mL. The power density as a function of system volume for an input power of 25 W is given in Figure 5.4. The corresponding maximum power density is 0.19 W mL^{-1}.

Table 5.6. Power dissipated in solution (W) for an input power of 25 W and for different solution volumes.

Generator Power (W)	100 mL	125 mL	150 mL
5.00	1	-	2
10.00	7	4	4
15.00	9	7	6
20.00	12	13	11
25.00	19	14	12

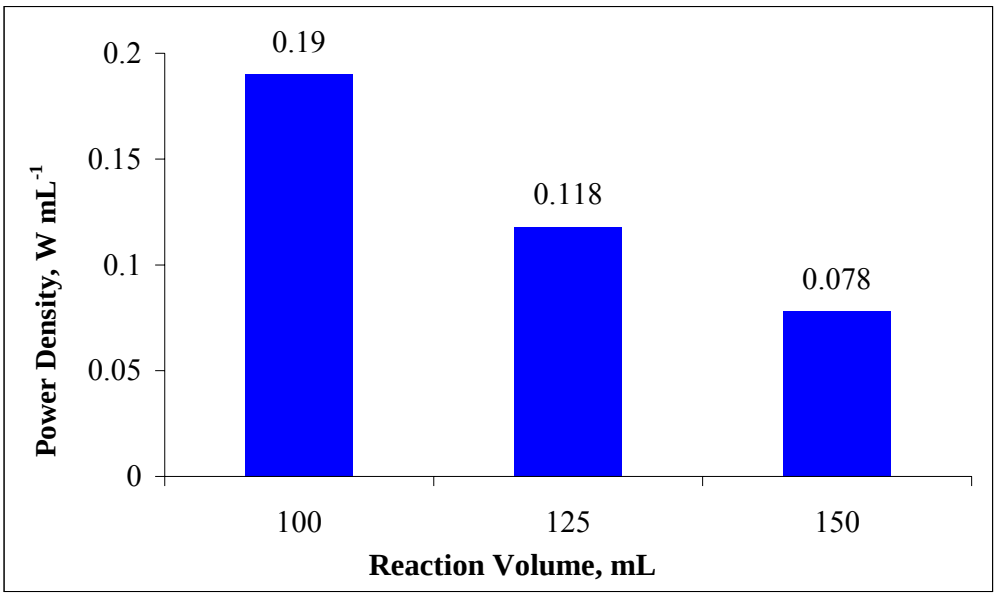

Figure 5.4. Power density as a function of reaction volume for an applied power of 25 W.

5.1.3. Evaluation of the Power Density in Reactor 3

The temperature increase in Reactor 3 during 5 min sonication using a generator output of 40 W without cooling is presented in Table 5.7.

Table 5.7. Temperature increase in Reactor 3 during sonication of 300 mL tap water for 5 minutes under 40 W power input without cooling.

t (s)	0	30	60	90	120	150	180	210	240	270	300
T (^{o}C)	26.5	27.5	28.5	29	30	31	31.5	32.5	33.5	34	34.5

The plot of T versus time and estimation of the slope from the fitted curve is presented in Figure 5.5. The value of dT/dt was estimated as 0.0312 °C s^{-1}. The power in solution was calculated in the same way as was done for the other reactors. The dissipated power P_d was also found using different volumes (other than 300 mL) as tabulated in Table 5.8. The maximum dissipation power of Reactor 3 is 39.1 W which corresponds to an input power of 40 W and a reactor volume of 300 mL. The power density as a function of system volume for an input power of 40 W is given in Figure 5.6. The corresponding maximum power density is 0.13 W mL^{-1}.

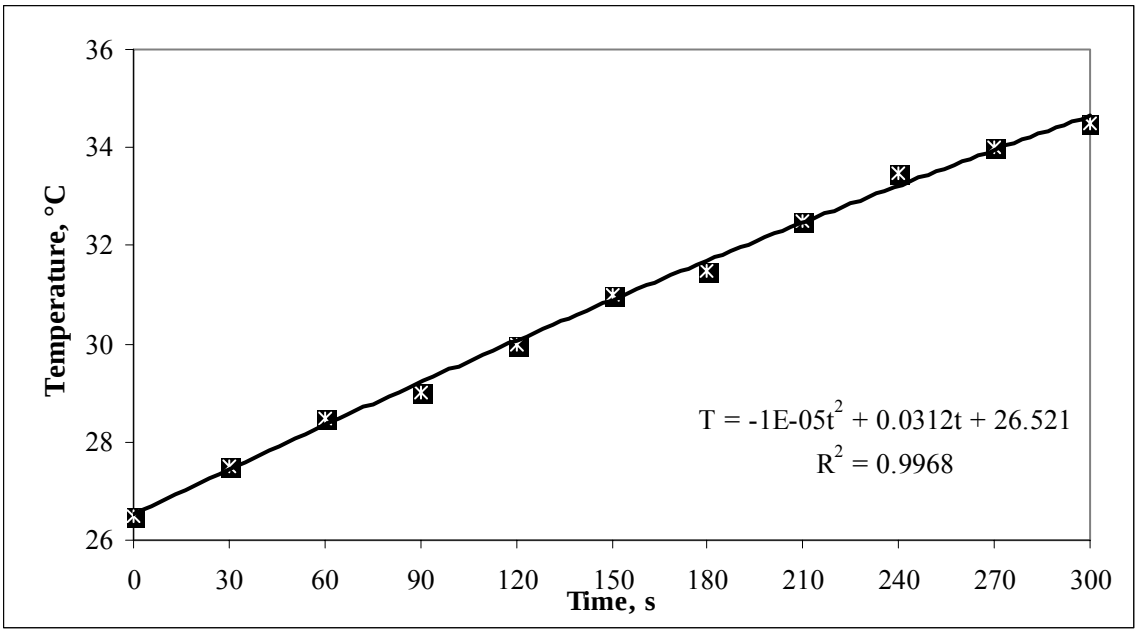

Figure 5.5. Temperature rise during 5 minutes sonication of tap water at 40 W generator output and best fit second-order polynomial.

Table 5.8. Power dissipated in solution (W) for different input power and solution volumes.

Generator Power (W)	300 mL	600 mL	900 mL	1200 mL
20.00	31.4	-	28.2	39.1
40.00	**39.1**	35.9	32.5	36.6
60.00	25.1	29.6	31.3	35.5
80.00	21.1	25.1	26.8	34.1
100.00	20.7	17.5	24.8	-

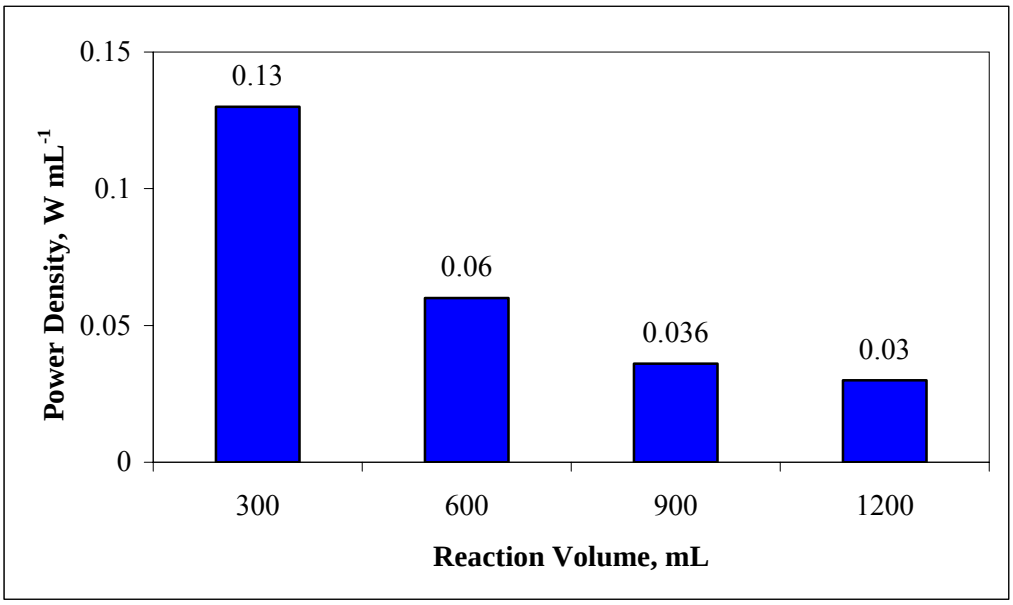

Figure 5.6. Power density as a function of volume for an applied power of 40 W.

5.1.4. Evaluation of the Power Density in Reactor 4

The temperature increase in Reactor 4 during sonication for 5 minutes under 390 W power input without cooling is presented in Table 5.9.

Table 5.9. Temperature rise in 1200 mL of tap water in Reactor 4 during sonication at 390 W generator output.

t (min)	0	0.5	1	1.5	2	2.5	3	3.5	4	4.5	5
T (ºC)	19.1	19.9	20.4	20.9	21.2	21.5	21.9	22.5	22.8	23.0	23.4

From the plot of T versus time and the fitted polynomial to the data (Figure 5.7) the temperature rise (dT/dt) was estimated as 1.0486 °C min^{-1} (0.0174 °C s^{-1}).

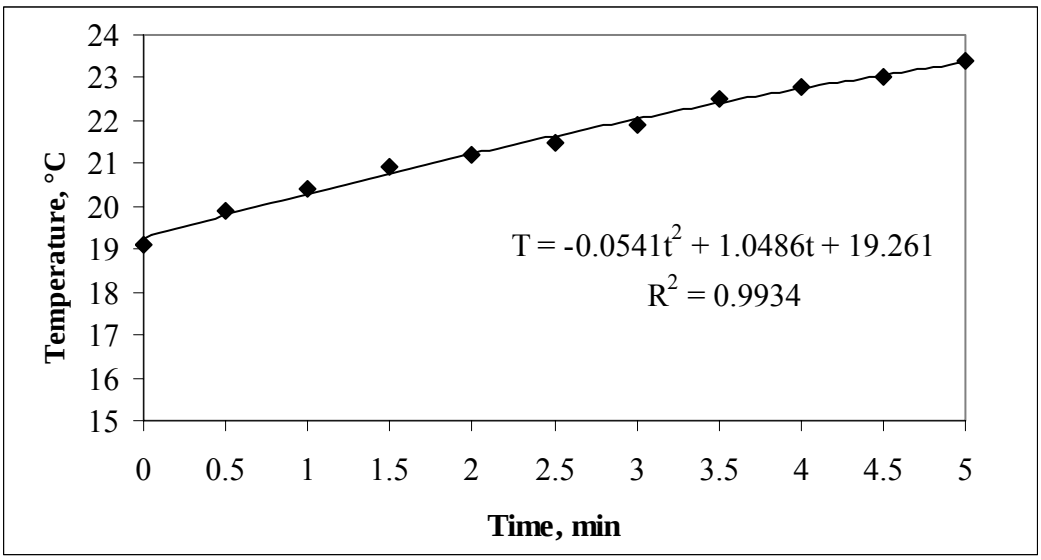

Figure 5.7. Temperature rise during 5 minutes sonication of tap water at 390 W generator output.

The dissipated power P_d was also found using different volumes (other than 1200 mL) as tabulated in Table 5.10. The power density as a function of system volume for an input power of 390 W is given in Figure 5.8. The corresponding maximum power density is 0.073 W mL^{-1}.

Table 5.10. Power dissipated in solution (W) for different input power and solution volumes.

Generator Power (W)	V = 1200 mL		Generator Power (W)	V = 1600 mL	
	Power Dissipation (W)	Power Density (WmL^{-1})		Power Dissipation (W)	Power Density (WmL^{-1})
240	60	0.050	240	55	0.034
300	67	0.056	280	61	0.038
320	78	0.065	320	99	0.062
340	74	0.062	360	82	0.051
350	76	0.063	370	64	0.040
360	80	0.067	390	90	0.056
370	79	0.066	420	88	0.055
390	87	0.073	450	70	0.044
400	91	0.076			
450	110	0.092			

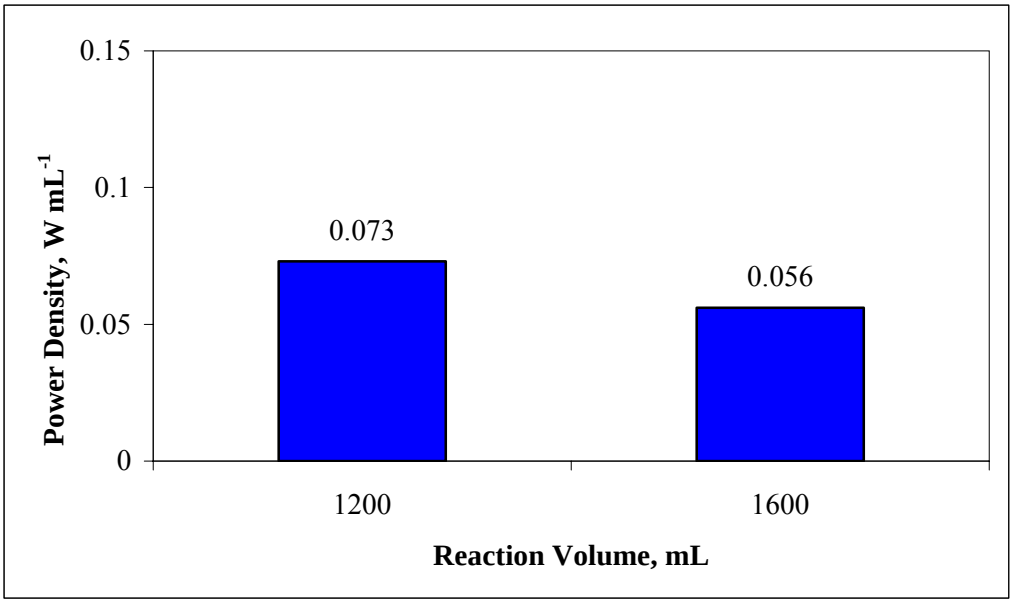

Figure 5.8. Power density as a function of reaction volume for an applied power of 390 W.

5.2. Conclusions

A summary of the above findings that correspond to optimum reactor parameters that were used throughout this study is presented in Table 5.11.

Table 5.11. Optimum reactor parameters.

REACTOR	**Power Applied (W)**	**Power Deposited (W)**	**Volume (ml)**
1	54	37.30	80
2	25	18.99	100
3	40	39.10	300
4	390	87.00	1200

6. BATCH EXPERIMENTS WITH ADVANCED OXIDATION PROCESSES

6.1. Decomposition of Phenol and 2-Chlorophenol by Ozonation and UV-Enhanced Ozonation

6.1.1. Background Information

Numerous methods have been proposed for the destruction of phenolic compounds in water. Among these Advanced Oxidation Processes (AOPs) have been found to be one of the most effective technologies. Ozonation, a common method of AOP, has been investigated by many researchers for the degradation of these compounds. A review of these studies was presented in Chapter 3. The oxidation reactions involving ozone were described in Chapter 2.

In this part of the study the destruction efficiency of phenol and 2-chlorophenol (2-CP) by ozonation was investigated. Specifically, the purpose was to determine the impact of various operating parameters (i.e. pH, ozone, initial phenol and 2-CP concentrations) on the reaction rate coefficients. A summary of the operating parameters considered is presented in Table 6.1. The impact of pH was assessed by monitoring the residual phenol and 2-CP at pH values of 3, 5, 7, and 10. The effect of ozone input was evaluated by ozonating the selected phenol and 2-CP concentrations at 2, 4, 5, and 7 g O_3 m^{-3}. The impact of the initial contaminant concentration on the rate of degradation of the compounds was evaluated by considering initial concentrations of 75, 150, 300, and 450 μM at pH 10. The effect of UV irradiation was determined by turning on of a short radiation (254 nm) UV lamp inserted into the reactor. A summary of the ozonation and UV/Ozone experimental set ups were described in Chapter 4.1.3.2.

Table 6.1. Operating parameters considered in the application of ozone to phenol and 2-chlorophenol.

Operating Conditions	Value
pH	3, 5, 7, and 10
Ozone Concentrations	2, 4, 5, and 7 g O_3 m^{-3}
Initital Contaminant Concentrations	75, 150, 300, and 450 μM
Contaminant	Phenol, 2-Chlorophenol, Mixture of the two
UV irradation	254 nm UV lamp at pH= 3, 5, and 10

6.1.2. Results and Discussion

Effect of pH:

The effect of pH was investigated by ozonation of 150 μM of the test compounds at pH=3.0, 5.0, 7.0 and 10.0. The rate of degradation was found to follow pseudo-first order kinetics in accordance with Equation (6.1):

$$\frac{dC}{dt} = -k'C \tag{6.1}$$

where

C : concentration of the test compound, μM

t : time, min

k' : the pseudo first order decay coefficient , min^{-1}

Normalized plots of C/C_0 against time and the estimated degradation rate constants of phenol and 2-chlorophenol are presented in Figures 6.1 and 6.2, respectively, where the solid lines show the fit of the data to Equation 6.2, which is obtained by integration of Equation 6.1. Estimated pseudo-first order decay rate coefficients for phenol and 2-CP at various pH values are presented in Table 6.2.

$$C = C_0 e^{-k't} \qquad (6.2)$$

C : concentration of Phenol or 2-CP at time = t , µM

C_0 : concentration of Phenol or 2-CP at time = 0, µM

k' : pseudo-first order decay rate constant, min^{-1}

t : time, min

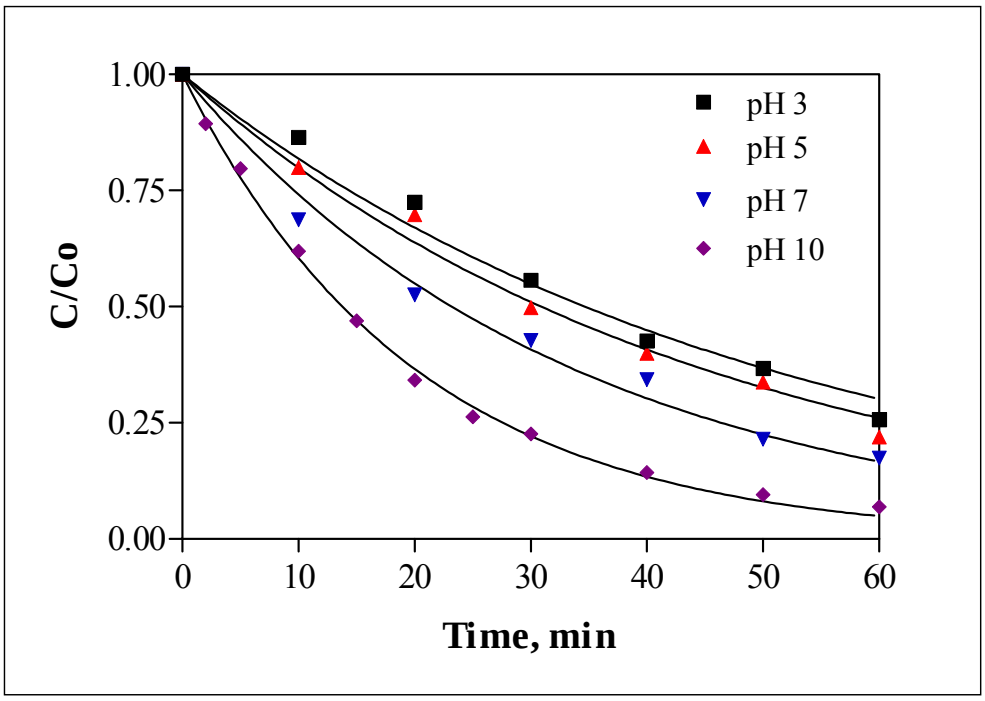

Figure 6.1. Effect of pH on the rate of phenol decomposition (C_0= 150µM; O_3 = 2 g m^{-3}).

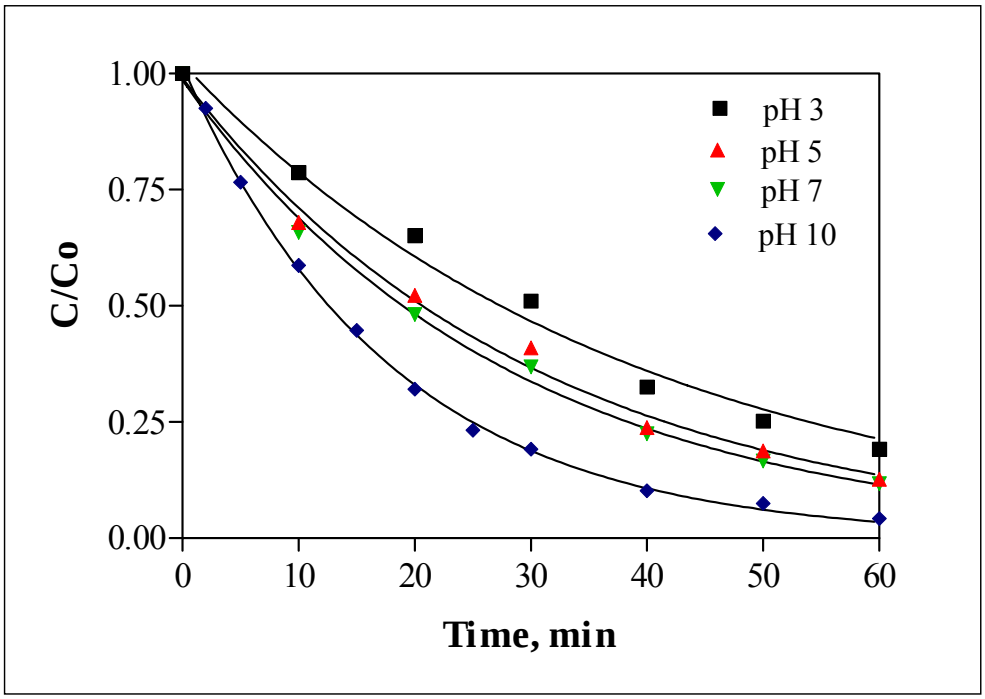

Figure 6.2. Effect of pH on the rate of 2-CP decomposition (C_0= 150 µM; O_3 = 2 g m^{-3}).

Table 6.2. Estimated pseudo-first order decay rate coefficients for phenol and 2-CP at various pH values.

Compound	**-k' x 10^{-2} (min^{-1})**			
	pH 3	**pH 5**	**pH 7**	**pH 10**
Phenol	2.10	2.29	2.89	5.03
2-CP	2.61	3.31	3.57	5.65

The reaction of aqueous phenol and 2-CP with ozone has been extensively studied by several authors and the degradation was found to follow pseudo-first order kinetics in consistency with our study (Augugliaro and Rizzuti, 1978; Hoigne and Bader, 1983; In and Ku, 1997; Abe and Tanaka, 1996; Bonez et al., 1997).

It was shown that the direct reactions of ozone by phenol and 2-CP at acidic pH were less significant than the indirect reaction of ozone with phenol and 2-CP at basic pH (pH=10). The faster degradation of the test compounds in alkali medium can be explained by the increase in the rate of decomposition of ozone, leading to the production of hydroxyl radicals (•OH). The dissociation products of phenol and 2-CP formed by the direct ozonation are also degraded as the indirect pathway prevails.

As reported by Staehelin and Hoigne (1982), the decomposition of ozone in an acidic medium is too low and the formation of the hydroxyl radicals is limited. Therefore, as the pH is lowered, the direct reaction of ozone becomes the dominant reaction pathway. Although ozone is a powerful oxidant, it is selective in terms of its reactions. However, hydroxyl radical is non selective in its reactions, allowing it to react with organic compounds (Weavers et al., 1998).

Moreover, the ionization of phenol and 2-CP are also enhanced by the increasing pH due to their dissociation constants of pKa= 9.99 and pKa=8.48, respectively.

Benitez et al. (2000) have studied the rate constants for the reactions of ozone with chlorophenols and indicated that the higher is the pH, the faster are the degradation of chlorophenols.

As can be seen from Table 6.2, the reaction rate constants for the degradation of 2-CP by ozone is greater than that of phenol. This is consistent with the study of Trapido et al. (1997), who have reported that the degradation rates increased as the number of chlorine atoms in the aromatic ring increased. This is due to the fact that the presence of chlorine enhances the dechlorination step, leading to an increase in the degradation rate.

Effect of Ozone Concentration:

The impact of O_3 input concentration on the rate of destruction is presented in Figures 6.3 and 6.4 for phenol and 2-CP, respectively. It was found that the degree of contaminant destruction increased with increasing inputs of ozone. Specifically, the total phenol removal in 30 min was equal to 77.38 %, 85.43 %, 89.22 % and 92.45 % at 2, 4, 5,

and 7 g O_3 m^{-3}, respectively; while the total 2-CP removal in 30 min was equal to 80.91, 88.07, 91.58 and 96.25 at 2, 4, 5, and 7 g O_3 m^{-3}, respectively.

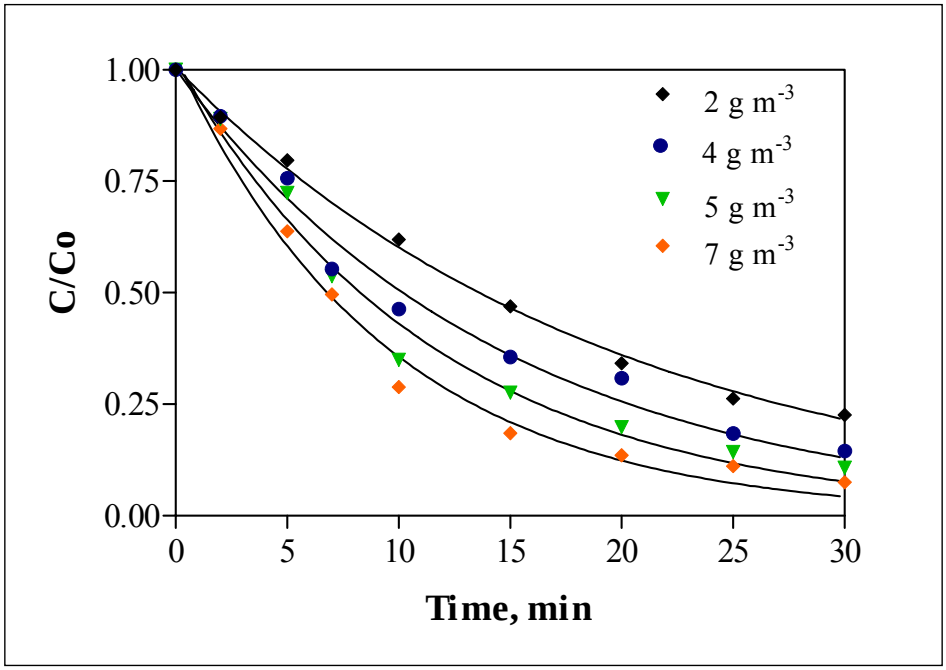

Figure 6.3. Effect of ozone input on the decomposition of phenol at pH=10 and C_0=150 µM.

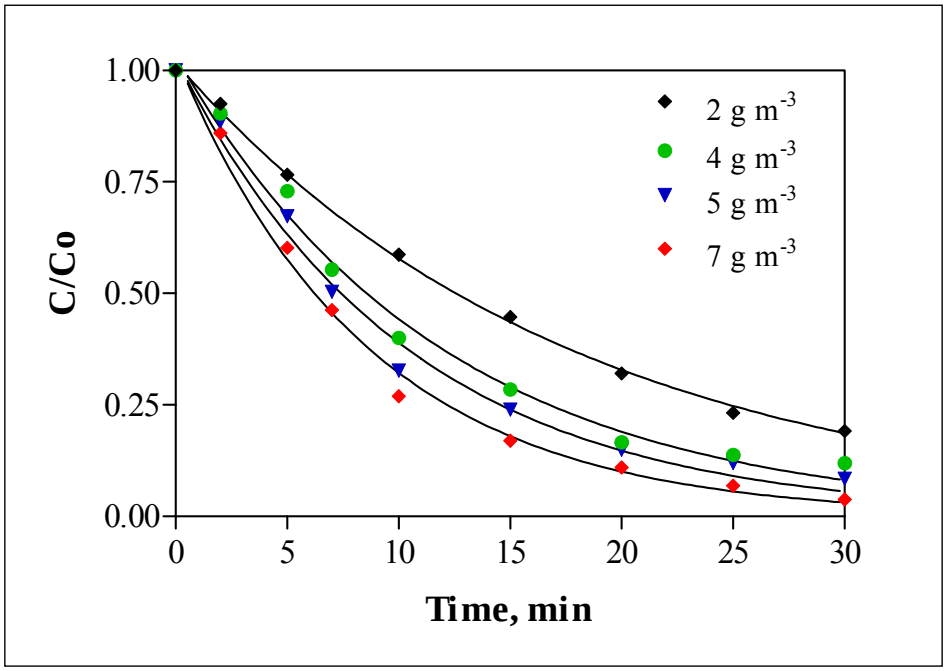

Figure 6.4. Effect of ozone input on the decomposition of 2-CP at pH=10 and C_0=150µM.

Estimated pseudo-first order decay rate coefficients for phenol and 2-CP at various ozone concentrations are presented in Table 6.3.

Table 6.3. Estimated pseudo-first order decay rate coefficients for phenol and 2-CP at various ozone concentrations.

Compound	**-k' x 10^{-2} (min^{-1})**			
	2 g m^{-3}	**4 g m^{-3}**	**5 g m^{-3}**	**7 g m^{-3}**
Phenol	5.03	6.81	8.64	10.58
2-CP	5.65	8.46	9.70	11.64

Effect of Initial Contaminant Concentration:

Effect of initial phenol and 2-CP concentrations were assessed by exposing 75, 150, 300 and 450 µM phenol and 2-CP to ozonation at pH=10. It was found that increasing concentrations of both compounds resulted in slower rates of reaction, as shown in Figure 6.5, Figure 6.6, and Table 6.4.

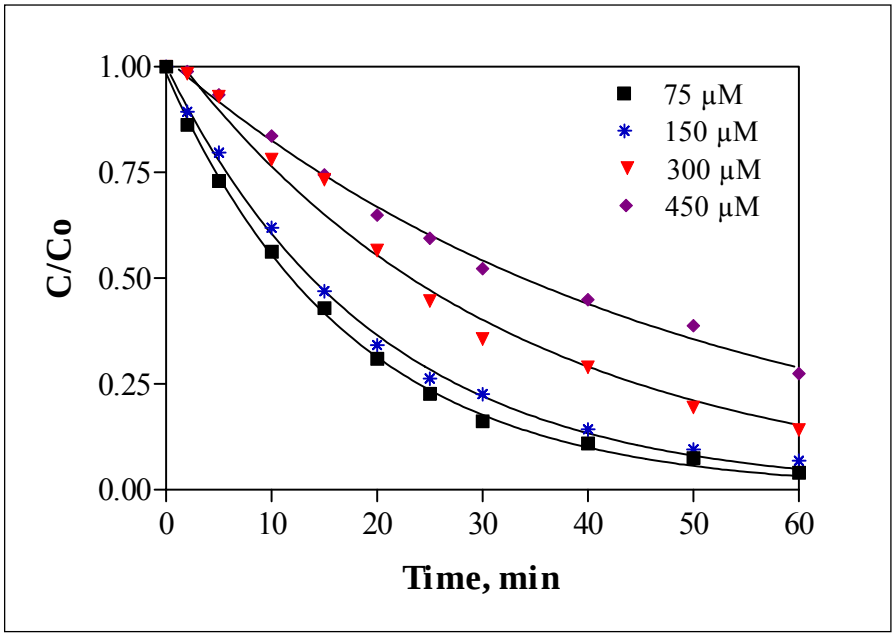

Figure 6.5. Effect of initial concentration on the rate of phenol decomposition by O_3 at pH=10.

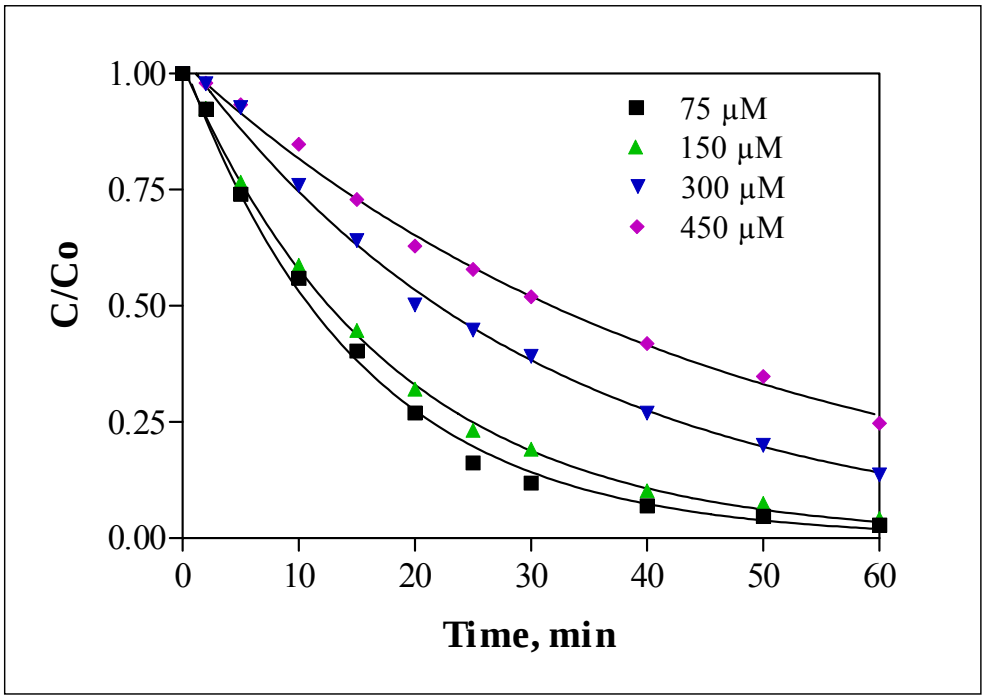

Figure 6.6. Effect of initial concentration on the rate of 2-CP decomposition by O_3 at pH=10.

Table 6.4. Estimated pseudo-first order decay rate coefficients for phenol and 2-CP at various initial concentrations.

Compound	**-k' x 10^{-2} (min^{-1})**			
	75 µM	**150 µM**	**300 µM**	**450 µM**
Phenol	5.72	5.03	3.21	2.10
2-CP	6.61	5.65	3.32	2.26

Effect of Phenol - 2-CP Mixture:

The effect of mixtures was investigated by combining equal concentrations of phenol and 2-CP in the same solution and monitoring the residual concentrations of each during 60 min ozonation at pH 10. Estimated decomposition rate coefficients in mixtures and single solutions are summarized in Table 6.5.

Table 6.5. Estimated decomposition rates in single solutions and mixtures (pH=10, O_3 concentration = 2 g m^{-3}).

Compounds in Solution	**Decomposition Rate Constant, -k' (min^{-1})**
150 μM Phenol	5.03×10^{-2}
150 μM 2-Chlorophenol	5.65×10^{-2}
150 μM Phenol &	3.09×10^{-2}
150 μM 2-Chlorophenol	3.24×10^{-2}

Effect of UV Irradiation:

The UV/O_3 experiments were run at both acidic and alkaline pH. The data revealed that irradiation of the test solutions with UV light during ozonation remarkably enhanced the decay of the compounds, and the effect was enlarged as the pH was increased. The result of Kuo's research also verifies that the efficiency of the combined ozone/UV treatment increases as the pH of the reaction medium increases. This was attributed to the fact that the initiation of ozonation could be catalyzed by OH^- ions. The rate profiles in UV/O_3 experiments are presented in Figure 6.7, 6.8 for phenol and 2-CP, respectively. Estimated pseudo-first order decay rate coefficients for phenol and 2-CP for UV/O_3 experiments at acidic and basic pH are presented in Table 6.6.

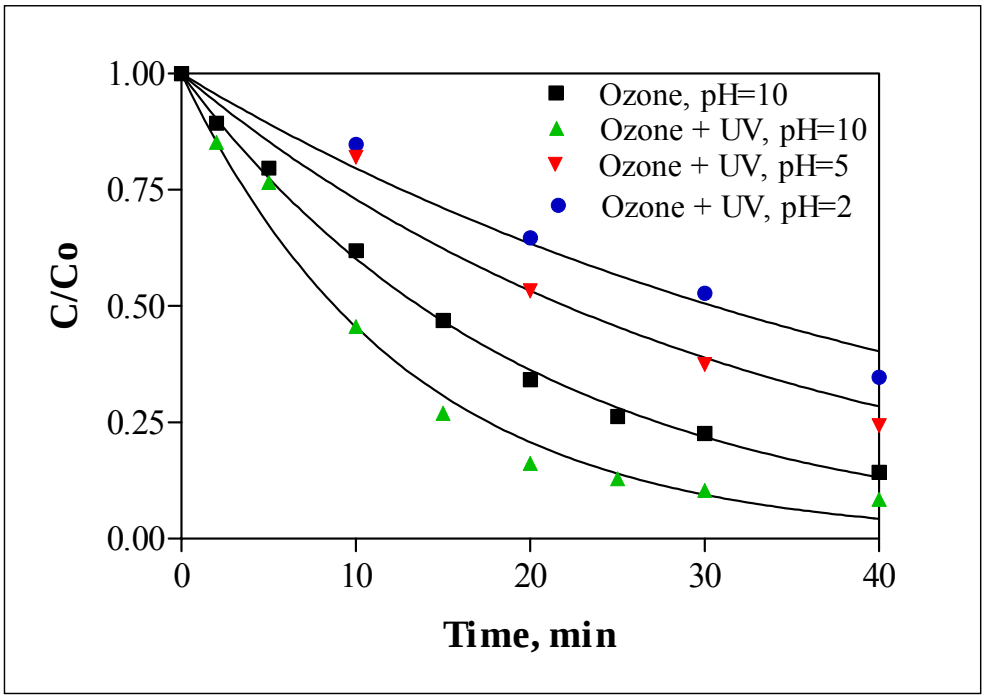

Figure 6.7. Degradation of 150 µM phenol by O_3/UV at various pH and 2 g O_3 m^{-3}.

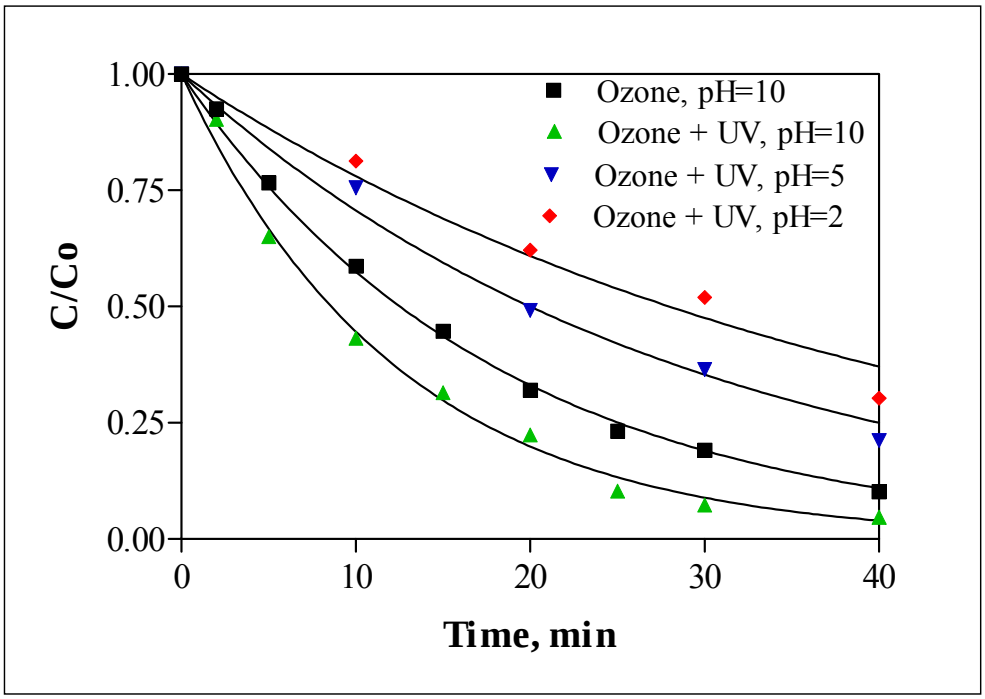

Figure 6.8. Degradation of 150 µM 2-CP by O_3/UV at various pH and 2 g O_3 m^{-3}.

Table 6.6. Estimated pseudo-first order decay rate coefficients for phenol and 2-CP for O_3/UV reactions.

Compound	-k' x 10^{-2} (min^{-1})			
	O_3 (pH=10)	**O_3/UV (pH=3)**	**O_3/UV (pH=5)**	**O_3/UV (pH=10)**
Phenol	5.03	2.74	3.30	8.06
2-CP	5.65	2.85	3.55	8.23

The enhancement of the reaction rates compared to direct photolysis or ozonation alone can be explained by the photolytic cleavage of O_3 to H_2O_2, which is further photolyzed to form excess hydroxyl radicals (OH•) as discussed Chapter 2.1.1.1.

It is also known that the extinction coeffiecient of ozone at 253.7 nm is also much higher than that of hydrogenperoxide. Glaze et al. (1991) showed that the decay rate of ozone is around 1000 times higher than that of hydrogenperoxide causing photolytic ozonation to be much more effective than ozonation or UV photolysis alone.

Gonzalez et al. (1995) have also demonstrated that the combination of ozone with UV had enhanced the efficiency of the single processes for 2-CP degradation. Esplugas et al. (1994) have indicated that pholoytic ozonation not only enhanced the degradation rates of phenolic compounds but also has led to a more effective mineralization.

6.1.3. Conclusions

The study showed that the efficiency of phenol and 2-CP destruction by O_3 is related to pH, initial contaminant concentration and the ozone input as: i) rate is accelerated by increased pH, due to decomposition of ozone at highly alkaline pH to •OH radicals; ii) the rate is accelerated by increased ozone input; iii) the rate is decelerated by increased initial contaminant concentration due to competition for •OH radicals. Irradiation of the solution with UV light at 254 nm was also an effective method of efficiency improvement upon production of excess OH radicals by photolysis of H_2O_2 produced by ozone decomposition.

6.2. Decomposition of Phenol and 2-Chlorophenol by Sonication

6.2.1. Background Information

The purpose of this part of the study was to investigate the destruction of phenol and 2- CP by ultrasonic irradiation and to assess the role of operating parameters on the rate of reaction. Experiments were run in Reactors 1, 2, 3 and 4 with consideration on the selection of the operation parameters such as frequency, pH, saturating gas (air, oxygen and argon) and initial contaminant concentration. A summary of the operating parameters considered is presented in Table 6.7. The impact of pH was assessed by monitoring the residual phenol and 2-CP at pH=2, 3, 5, 7, and 10. The role of initial contaminant concentration was determined by monitoring the rate of degradation of the compounds at 75, 150, 300, and 450 μM at pH 3. Single contaminants (phenol and 2-chlorophenol) as well as mixtures of both were investigated. The sparging gases considered include Argon, air and oxygen. The effect of coupling ultrasound with ozone was investigated by bubbling the solution with 2 g O_3 m^{-3}. The US/Ozone experimental set up was described in detail in Chapter 4.1.3.2.

Table 6.7. Operating parameters considered in the application of sonication to phenol and 2-chlorophenol.

Operating Conditions	Value
Frequency	20, 300, 520, 3x520 kHz
pH	2, 3, 5, 7, and 10
Initital Contaminant Concentrations	75, 150, 300, and 450 μM at pH=3
Saturating Gas	Ar, Air, O_2
Contaminant	Phenol, 2-Chlorophenol, Mixture
Effect of Ozone Input	2, g O_3 m^{-3} at pH=3, 7, and10

6.2.2. Results and Discussion

Effect of Applied Frequency:

The effect of applied frequency was investigated by sonication of 150 µM phenol and 150 µM 2-CP in Reactors 1, 2, 3 and 4 during bubbling with argon. The rate of degradation was found to follow pseudo-first order kinetics in accordance with Equation 6.2. The rate profiles and estimated pseudo-first order decay rate coefficients are presented in Figures 6.9-6.10 and Table 6.8, respectively.

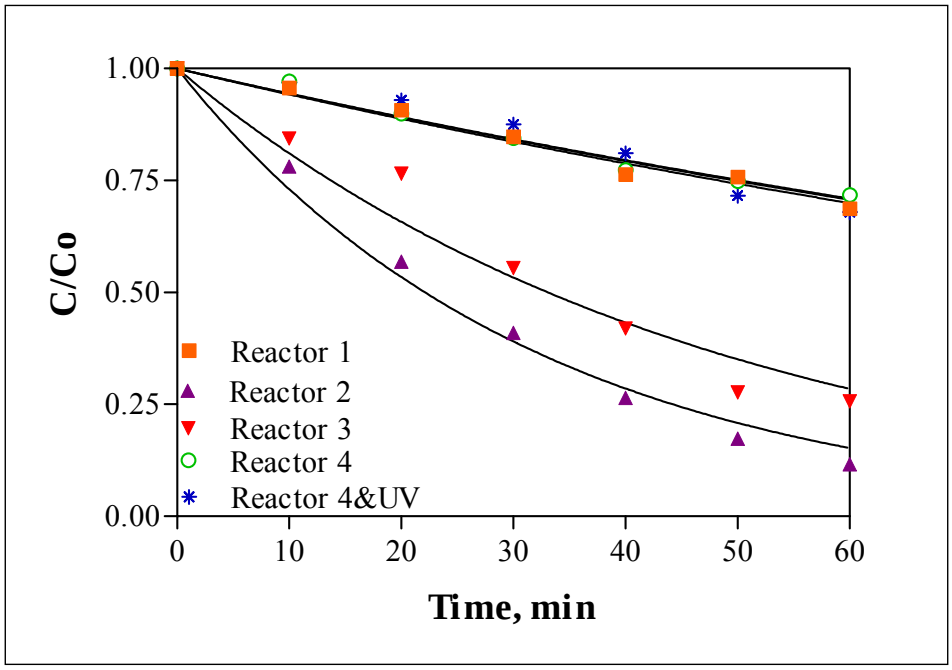

Figure 6.9. Effect of applied frequency on sonochemical degradation of phenol; C_0 =150 µM, sparge gas = Ar.

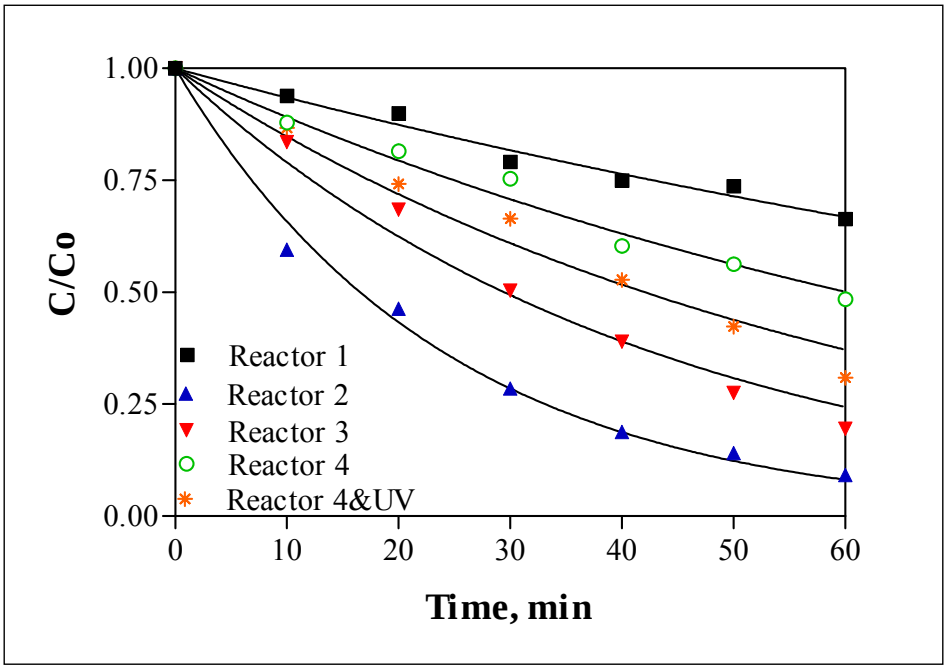

Figure 6.10. Effect of applied frequency on sonochemical degradation of 2-CP; C_0 =150 µM, sparge gas = Ar.

Table 6.8. Estimated pseudo-first order decay rate coefficients for phenol and 2-CP in different ultrasonic reactors.

Compound	-k' x 10^{-2} (min^{-1})				
	Reactor 1	**Reactor 2**	**Reactor 3**	**Reactor 4**	**Reactor 4&UV**
Phenol	0.62	3.24	2.22	0.59	0.61
2-CP	0.68	4.09	2.46	1.17	1.65

The data revealed that maximum ultrasonic destruction was achieved in 60 minutes exposure of the compounds to 300 kHz ultrasound, while sonication with 20 kHz was inefficient for destruction. The inefficiency of 20 kHz is due to (i) the interactive effects of long collapse duration leading to lower yield of OH radicals in the bulk liquid and (ii) low volatility of phenol that resists its diffusion into the gas phase, as reported by Ince and Kidak (2006). Hence, the explanation for higher reaction rates in Reactor 2 and 3 (higher

frequencies) can be explained by the longer-lived cavitation bubbles and shorter collapse durations at these frequencies.

The study of Petrier and Francony (1997), where the relative efficiencies of 20 kHz, 200 kHz and 500 kHz were compared, has shown that the highest rate of phenol destruction was achieved at 200 kHz, owing to the larger potential for ejection of radical species to the bulk solution. In a similar study by Ince and Kidak (2006), where the efficiencies of 300 and 520 kHz were compared, it was shown that 300 kHz was more efficient owing to longer lived bubble advantages over short lasting but less energetic cavity collapse at 520 kHz. Similarly, sonolysis of 4-CP at 20, 200, 500, and 800 kHz has been studied by Petrier et al. (2006) and reported that the most efficient frequency is 200 kHz.

Effect of pH:

The effect of pH was investigated by sonication of 150 μM of each test compound at pH=2.0, 3.0, 5.0, 7.0 and 10.0 during bubbling with argon in Reactor 2. The destruction rate profiles and estimated values of pseudo-first order rate coefficients are presented in Figures 6.11, 6.12 and Table 6.9, respectively.

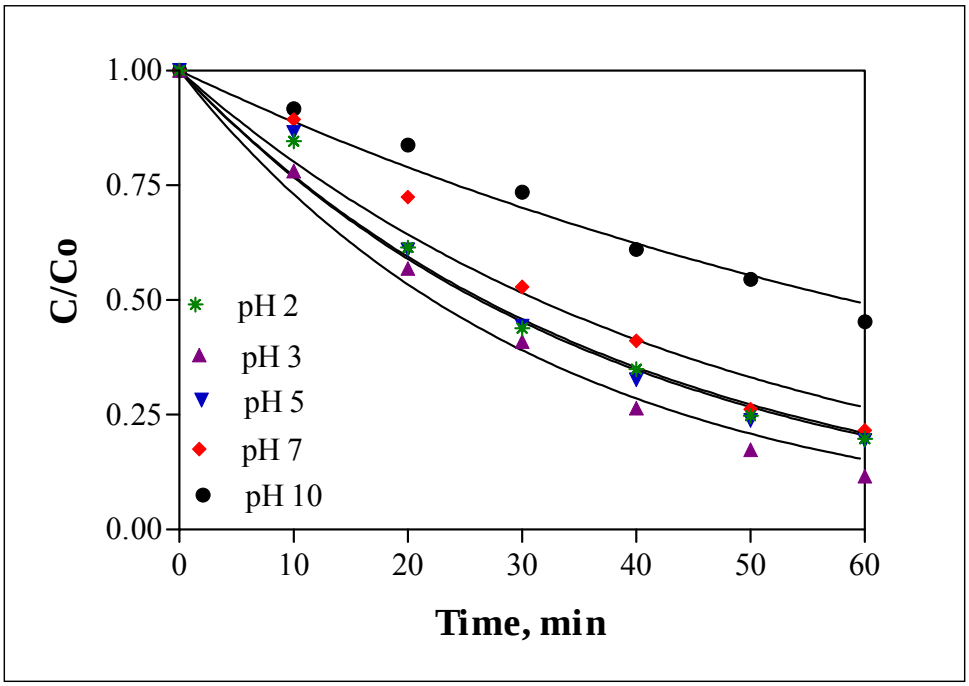

Figure 6.11. Effect of pH on sonochemical degradation of phenol in Reactor 2 (C_0 =150 µM, sparge gas=Ar).

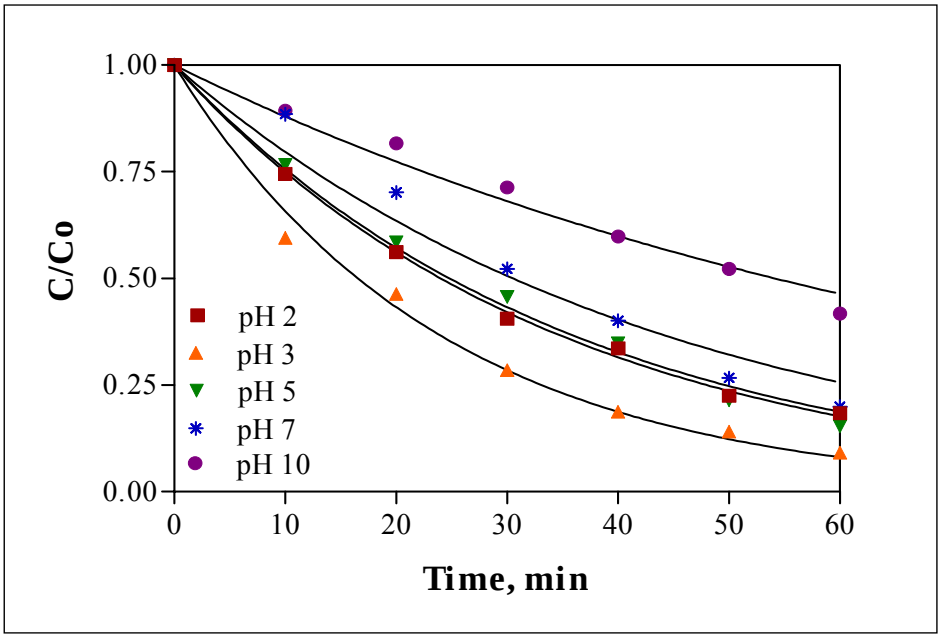

Figure 6.12. Effect of pH on sonochemical degradation of 2-CP in Reactor 2 (C_0 =150 µM, sparge gas=Ar).

Table 6.9. Estimated pseudo-first order decay rate coefficients for phenol and 2-CP at various pH values.

Compound	**-k' x 10^{-2} (min^{-1})**				
	pH 2	**pH 3**	**pH 5**	**pH 7**	**pH 10**
Phenol	2.71	3.24	2.78	2.39	1.26
2-CP	2.87	4.09	2.83	2.44	1.34

The dissociation constants for phenol and 2-CP are pK_a=9.99 and pK_a=8.48, respectively. As pH increases above pKa, the compounds ionize and therefore cannot approach the negatively-signed cavity bubbles or the interfacial area (Petrier and Francony, 1997). However, at acidic pH the compunds exist in molecular form and are more hydrophobic than ionized species, thus having a larger chance of moving towards the interfacial area, where the concentration of OH radicals is maximum (Ince and Kidak, 2006). Consistent with this phenomenon, it was observed that the maximum reaction rates were achieved at pH=3. On the other hand, the rate of reaction was found to be slightly lower at pH=2, which can be explained by the competition for OH radicals induced by a high concentration of SO_4^{2-} at this condition.

Effect of Saturating Gas:

The impact of saturating gas was determined by sparging air, oxygen or argon into the solution during exposure of the solutions to sonication in Reactor 2. Logarithmic variation of the residual phenol and 2-CP concentrations under each gas injection are presented in Figures 6.13 and 6.14, respectively while the estimated rate coefficients are listed in Table 6.10.

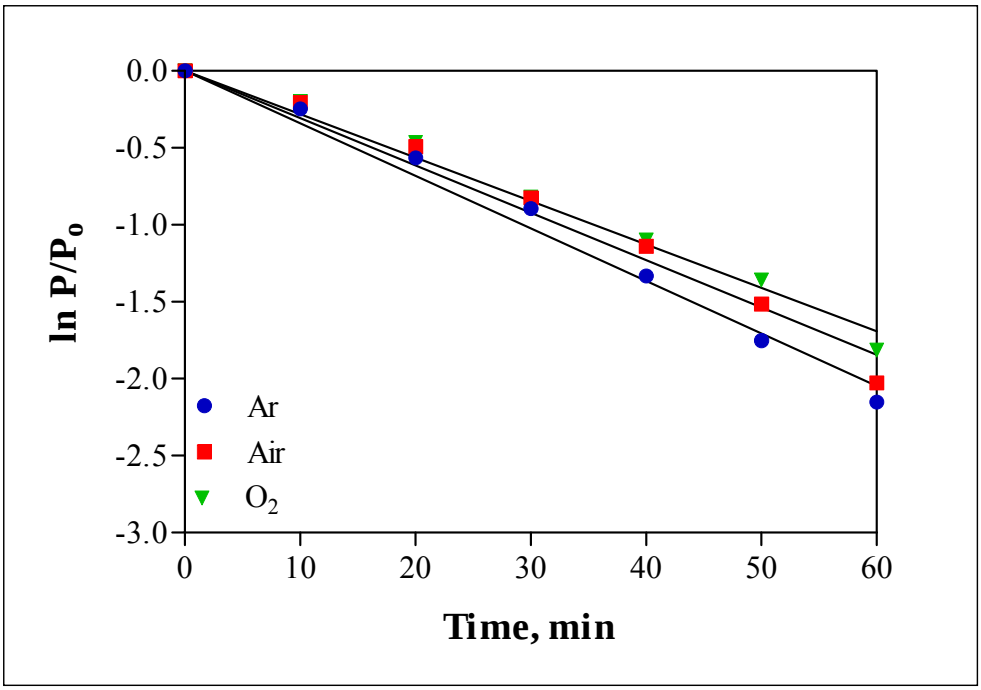

Figure 6.13. Ultrasonic destruction of phenol during air, oxygen, and argon bubbling at Reactor 2 (C_0=150 µM, pH=3).

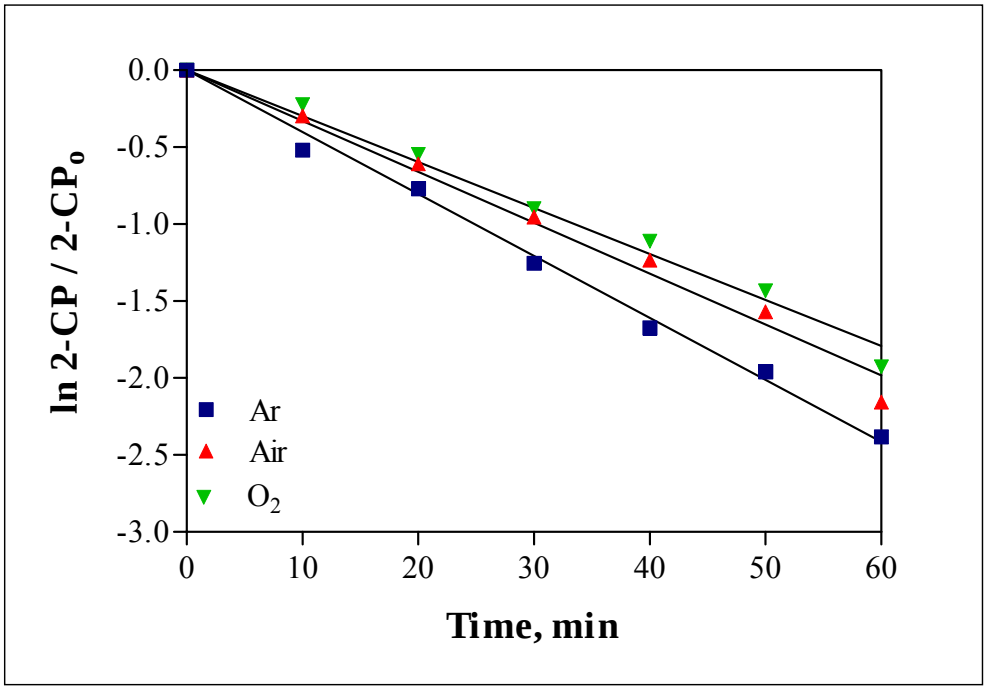

Figure 6.14. Ultrasonic destruction of 2-CP during air, oxygen, and argon bubbling at Reactor 2 (C_0=150 µM, pH=3).

Table 6.10. Estimated pseudo-first order decay rate coefficients for phenol and 2-CP at various sparge gases.

Compound	-k' x 10^{-2} (min^{-1})		
	Ar	**Air**	**O_2**
Phenol	3.24	3.07	2.82
2-CP	4.02	3.31	2.99

The data in Figures 6.13-6.14 and the rate constants given in Table 6.10 show that maximum destruction of the compounds occurs in the presence of argon gas and the rate decreases in the following order: Ar > Air > O_2. The most common explanation to this is found in the ratio of specific heats or the fact that Ar has the largest polytropic gas ratio, which allows much higher bubble temperatures. Consistently, in the study of Nagata et al. (2000), it has been reported that the degradation of 2-, 3-, and 4-CP at 200 kHz was most rapid under an argon atmosphere than air due to much higher cavitation effects obtained in the presence of the former. On the other hand, the study of Ku et al. (1997) has shown that the degradation of chlorophenols were unaffected by altering the sparge gas between oxygen and air, due to similar polytropic gas ratios.

H_2O_2 Formation:

The formation of H_2O_2 in sonicated solutions is a direct measure of the presence of OH radicals. Relative rates of H_2O_2 formation in pure water and in various concentrations of 2-CP solutions during 60 min sonication at 300 kHz is presented in Figure 6.15. It was found that H_2O_2 tended to accumulate in pure water, whereas it was rapidly depleted as the concentration of 2-CP was increased, indicating enhanced consumption of OH radicals by 2-CP with increasing initial concentration.

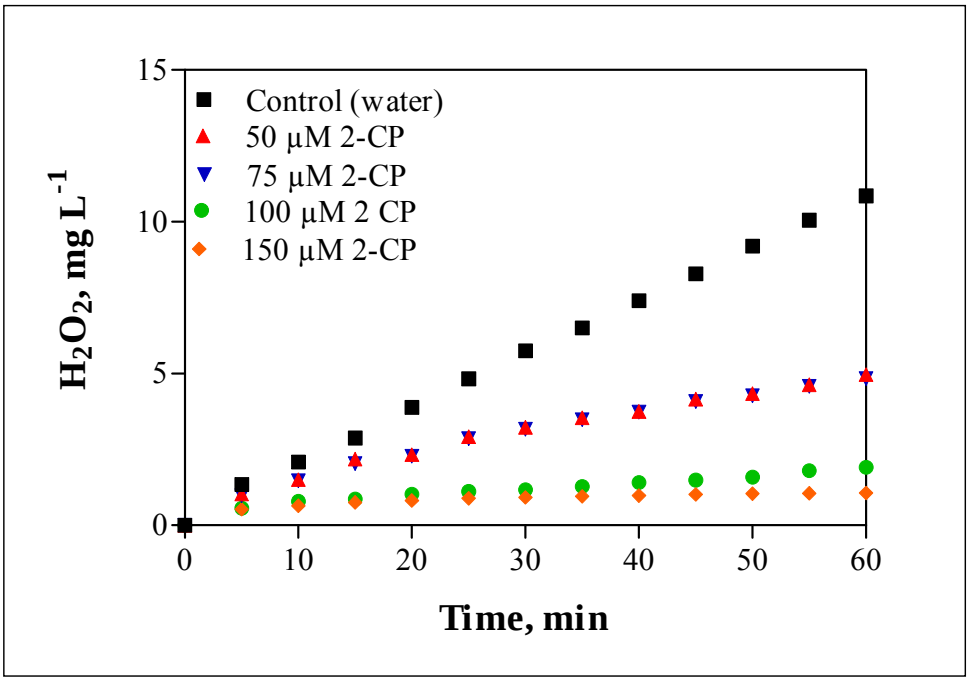

Figure 6.15. H_2O_2 formation/depletion during sonication of 2-CP in Reactor 2.

Effect of Initial Contaminant Concentration:

Effect of initial phenol and 2-CP concentrations was evaluated by exposing 75, 150, 300 and 450 µM phenol and 2-CP to sonication in Reactor 2 while continuously bubbling with Ar. The solution pH was adjusted to 3.0 to improve the efficiency. The impact of concentration on rates of phenol and 2-CP decay is presented in Figures 6.16 and 6.17, respectively and the estimated rate coefficients are listed in Table 6.11.

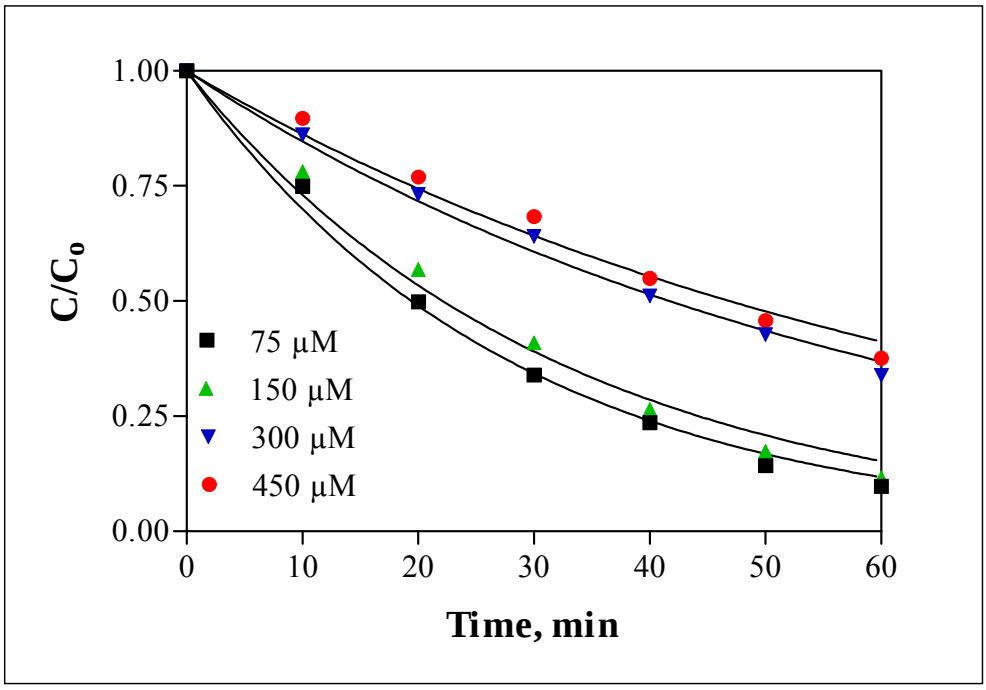

Figure 6.16. Effect of initial concentration on the rate of phenol degradation by ultrasound. (Sparge gas: Ar, pH=3, frequency=300 kHz.)

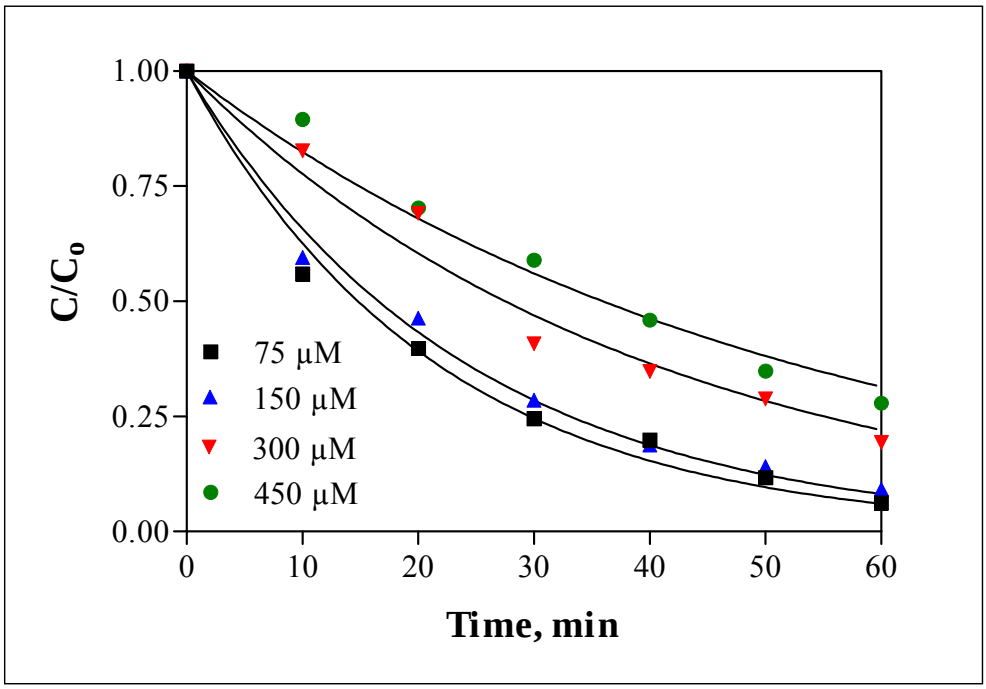

Figure 6.17. Effect of initial concentration on the rate of 2-CP degradation by ultrasound. (Sparge gas:Ar, pH=3, frequency=300 kHz.)

Table 6.11. Estimated pseudo-first order decay rate coefficients for phenol and 2-CP at various initial concentrations.

Compound	**-k' x 10^{-2} (min^{-1})**			
	75 µM	**150 µM**	**300 µM**	**450 µM**
Phenol	3.65	3.24	1.71	1.56
2-CP	4.55	4.09	2.63	2.05

It was found that as the initial concentrations of the compounds was increased, the rate of reaction decreased, as typical of saturation type of kinetics proposed by several authors. This is consistent with the study of Jiang et al. (2006), which also reports lower degradation rates with increasing contaminant concentration.

Product Yield:

"Product yield" in sonochemical reactions is defined as the change in chemical concentration in the experiment volume per power of the sonic energy deposited in that volume and can be estimated by the following equation (Tauber, 2000):

$$G = \frac{\Delta MV}{E} \tag{6.3}$$

where:

G = ultrasonic yield of products, mole J^{-1}

ΔM= change in molar concentration of the test compound at the end of sonication time, M

V: reactor volume, L

E: ultrasonic energy deposited in the reactor volume, J

The energy deposited in each reactor was calculated using the deposited power values that were found by calorimetric measurements descibed in Chapter 5. The product yields for test compound concentrations of 150 µM were estimated using Equation 6.3. The results are presented in Table 6.12. In addition, the relation of "product yield" to initial concentration is presented in Figure 6.18 for Reactor 2.

Table 6.12. The product yields (C_0=150 µM, t=60 min) in the test reactors.

REACTOR	$Gx10^{-10}$ (mol J^{-1})	
	Phenol	2-CP
1	0.28	0.30
2	1.94	1.99
3	2.37	2.57
4	1.61	1.95

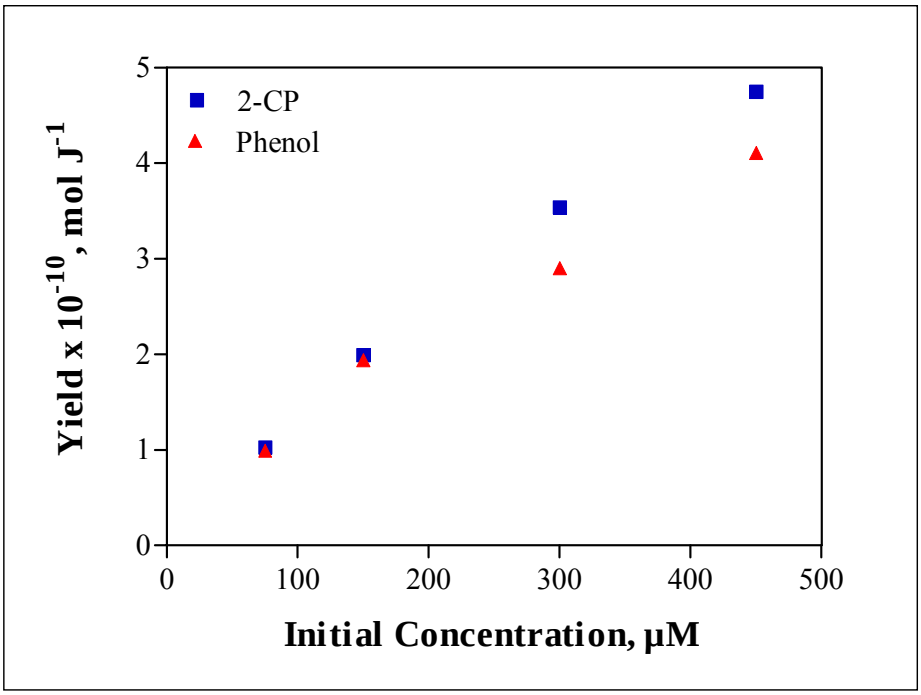

Figure 6.18. Variation of product yield in Reactor 1 with initial substrate concentration.

It was observed that the ultrasonic yield increased with the initial contaminant concentration, in contrast with the decrease in degradation rates with increasing initial concentrations. The decrease in the reaction rates can be attributed to the competition for hydroxyl radicals in the bulk liquid; whereas the increase in yield can be attributed to the reactions occurring in the bubble-liquid interface, in addition to the reactions in the bulk liquid.

Although the maximum degradation rate constants were achieved with Reactor 2 for both contaminants; the values of G followed the order of: Reactor 3 > Reactor 2 > Reactor 4 > Reactor 1 for phenol, and Reactor 3 > Reactor 2 > Reactor 4 > Reactor 1 for 2-CP. However, if the reactors are compared in terms of the percentage of power deposited in the solution over the applied power, then the power transfer efficiencies follow the order : Reactor 3 (98%) > Reactor 2 (76%) > Reactor 1 (69%) > Reactor 4 (22%).

Effect of Phenol: 2-CP Mixture:

Owing to the fact contaminated waters may contain a complex mixture of organic contaminants, the behavior of the test compounds in presence of a mixture were also tested for 60 min sonication in Reactor 2 at pH 3. The estimated rate constants in a 1:1 mixture (M/M) are listed in Table 6.13 together with the rate constants obtained for the single solutions. As can be seen from the table, the degradation rate constants of the mixture contaminants decreased compared to the mixture, due to the competition for OH radicals. Comparison of the rate constants of the mixture (150 μM: 150 μM) to those of the single compounds at 300 μM indicates that the 2-CP degradation by sonication at 300 kHz is slightly favored.

Table 6.13. Comparative rate constants in mixtures and single solutions corresponding to sonication for 60 min in Reactor 2.

Test Solution	-k' (min^{-1})
Mixture: (150 µM:150 µM)	Phenol: 2.00 2-CP: 2.54
Single (150 µM)	Phenol: 3.24 2-CP: 4.09
Single (300 µM)	Phenol: 1.71 2-CP: 2.63

Effect of Ozone:

To determine the effect of O_3 on the rate of sonochemical decomposition of the test compounds, the residual concentration of each was monitored during injection of ozone into Reactor 2 at pH=3, 7 and 10. The observed rate profiles (logarithmic) for phenol and 2-CP in the presence of O_3 at each test pH are presented in Figure 6.19 and 6.20, respectively. (Note that a control data set is included for ultrasound alone at pH 3 for comparison.) Values of the pseudo-first order decay rate constants corresponding to each fitted solid line are listed in Table 6.14.

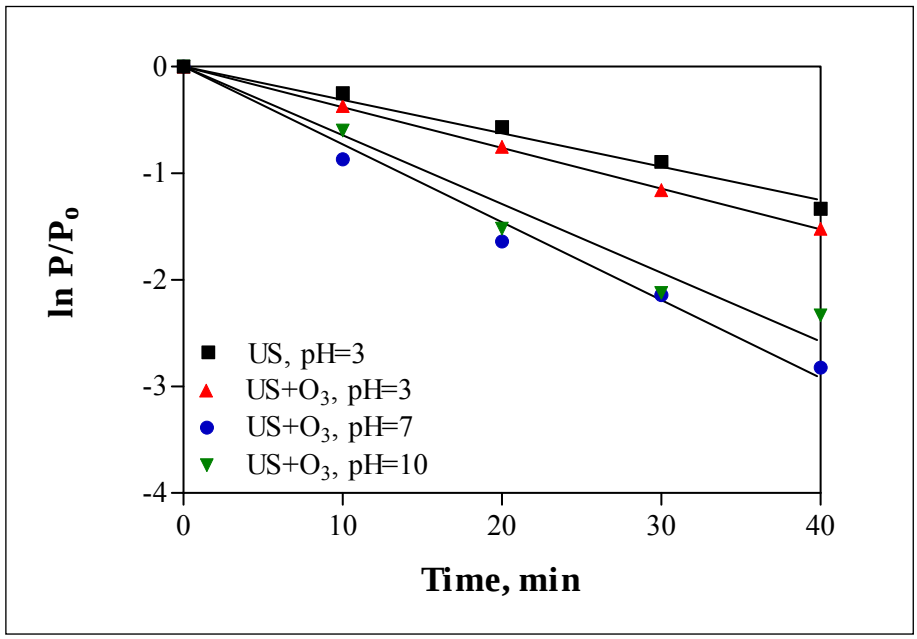

Figure 6.19. Variation in the rate of phenol degradation by US/O_3 with pH (C_0=150 µM, frequency=300 kHz; O_3 = 2 gm^{-3}).

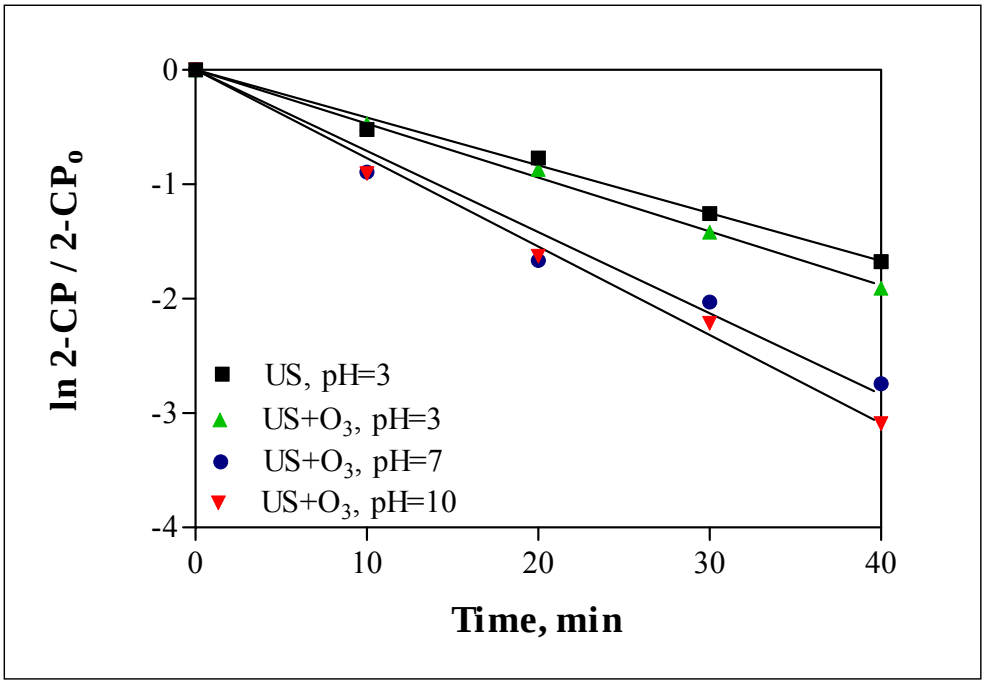

Figure 6.20. Variation in the rate of 2-CP degradation by US/O_3 with pH (C_0=150 µM, frequency=300 kHz; O_3 = 2 gm^{-3}).

Table 6.14. Estimated pseudo-first order decay rate coefficients for phenol and 2-CP for US/O_3 reactions.

Compound	**-k' x 10^{-2} (min^{-1})**			
	US (pH=3)	**US/O_3 (pH=3)**	**US/O_3 (pH=7)**	**US/O_3 (pH=10)**
Phenol	3.24	3.82	6.44	7.29
2-CP	4.09	4.70	7.09	7.72

The data revealed that injection of O_3 to the ultrasound reactor enhanced the rate of decay of both compounds as a consequence of thermal decomposition of ozone during bubble collapse to very reactive species as:

$$O_{3\,(g)} +))) \longrightarrow O_{2\,(g)} + O\,(^3P)_{(g)} \quad (6.4)$$

$$O\,(^3P)_{(g)} + H_2O_{(g)} +))) \longrightarrow 2\,\bullet OH(g) \quad (6.5)$$

The relative performances of individual and combined systems at various pH values for phenol and 2-CP removal are presented in Table 6.15 and 6.16, respectively.

Table 6.15. Estimated pseudo-first order decay rate coefficients of individual and combined systems at various pH for phenol removal.

pH	**-k' x 10^{-2} (min^{-1})**		
	US	**O_3**	**US/O_3**
3	3.24	2.10	3.82
7	2.39	2.89	6.44
10	1.26	5.03	7.29

Table 6.16. Estimated pseudo-first order decay rate coefficients of individual and combined systems at various pH for 2-CP removal.

pH	**-k' x 10^{-2} (min^{-1})**		
	US	**O_3**	**US/O_3**
3	4.09	2.61	4.70
7	2.44	3.57	7.09
10	1.34	5.65	7.72

The results indicate that the enhancement was much larger at pH 10, due to the generation of excess OH radicals at this condition by the decomposition of aqueous ozone. At pH 3, the sum of the individual rate constants for phenol (k'= -5.34x10^{-2} min^{-1}) and 2-CP (k'= -6.70x10^{-2} min^{-1}) were found to be greater than that of the combined system (k'= -3.82x10^{-2} min^{-1} for phenol and k'= -4.70x10^{-2} min^{-1} for 2-CP), indicating that the injection of O_3 did

not have a significant effect at this pH. However, the sum of the individual rate constants for phenol and 2-CP at pH 7 and 10 were less than the observed reaction rate constants, indicating a synergistic effect.

Mineralization:

The mineralization of the test compounds was investigated by taking samples in 15 minute time intervals from Reactor 2 and analyzing the residual total organic carbon (TOC) in solution. The data are presented in Figure 6.21. It was found that fractions of TOC removal in phenol (12.68%) and 2-CP (14.78%) in 60 minutes were relatively small compared to fractions of decay (88.37% and 90.77%, respectively). The study of Ince and Tezcanli (2001) reported that longer contact times are required for significant degrees of mineralization by ultrasound. It can be deduced that the major degradation reaction pathway is due to the OH radicals in the bulk liquid, not accumulating at the bubble-liquid interface.

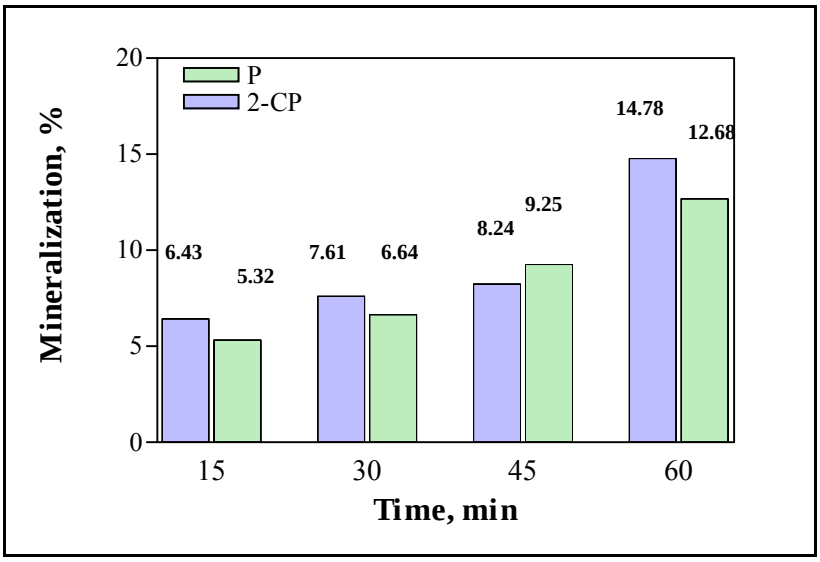

Figure 6.21. Mineralization of phenol and 2-CP by 60 min sonication at 300 kHz (C_0=150 μM).

6.2.3. Conclusions

The experimental study described herein has shown that ultrasonic destruction of phenol and 2-CP followed pseudo-first order kinetics, and the operating parameters that affected the rate of reaction were frequency, pH, saturating gas and initial substrate concentration. It was found that maximum decay was achieved in presence of Argon at 300 kHz and pH 3. Addition of O_3 to solution during sonication was found to enhance the rate of reaction via the production of additional reactive species. The effect of sonication of a phenol-2-CP mixture was to decelerate the rate of substrate degradation upon increased competition for OH radicals. Mineralization was relatively small, due to the reactions caused by the OH radicals in the bulk liquid. Moreover, the contact time was not sufficient for the significant conversion of TOC to CO_2.

6.3. Adsorption of 2-Chlorophenol on Nanoparticles

6.3.1. Background Information

The aim of the study was to investigate the adsorption capacity of 2-chlorophenol on nanoparticles. Fe (II,III) Oxide, FeNi Oxide, RNIP, Copper Oxide and TiO_2 nanoparticles were used as adsorbents. All adsorption runs were carried out in 50 mL flasks shaken at 100 RPM and 25 ºC. Memmert SV 1422 horizontal shaker was used throughout the experiments.

The adsorption isotherms were constructed by contacting different masses of nanoparticles (1, 3, 5, 7, and 10 g L^{-1}) with fixed concentration of 2-CP (150 μM) for 24 hours. Samples were collected periodically to monitor the reduction in 2-CP concentration. The data were evaluated by fitting them into the linearized forms of Freundlich and Langmuir Equations, defined by Equation 6.6 and 6.7, respectively.

Freundlich Isotherm

$\ln (q_e) = \ln K_f + (1/n) \ln C_e$

(6.6)

where;

q_e : mass of adsorbate adsorbed per unit mass of adsorbent

C_e : equilibrium concentration of adsorbate in solution

K_f and 1/n : empirical constants

Langmuir Isotherm

$1/ q_e = 1/b + (1/ab) (1/C_e)$

(6.7)

where;

q_e : mass of adsorbate adsorbed per unit mass of adsorbent

C_e : equilibrium concentration of adsorbate in solution

a, b : empirical constants

6.3.2. Results and Discussion

The adsorption experiments revealed that Fe (II,III) Oxide, Fe Ni Oxide and Copper Oxide nanoparticles were not suitable for 2-CP adsorption. However, when 2-CP was contacted with RNIP or TiO_2, adsorption was observed. Adsorption isotherms constructed for RNIP and TiO_2 are illustrated in Figures 6.22 through 6.25. It can be seen that data obtained from RNIP and TiO_2 adsorption fit better to the Freundlich isotherm.

The constant K_f in the Freundlich isotherm is related primarily to the strength of adsorption. For fixed values of C_e and 1/n, the larger the value of K_f, the larger the capacity q_e is. For fixed values of K_f and C_e, the smaller the value of 1/n, the stronger the adsorption

bond is. The constants ln K_f and 1/n were found to be -38.437 and 8.7962 for TiO_2 and -26.489 and 5.8509 for RNIP, respectively.

In the Langmuir isotherm, the constant a corresponds to the surface concentration at monolayer coverage and represent the value of qe, that can be achieved as Ce is increased. The constant b is related to the energy of adsorption and increases as the strength of the adsorption bond increases (Pontius, 1990).

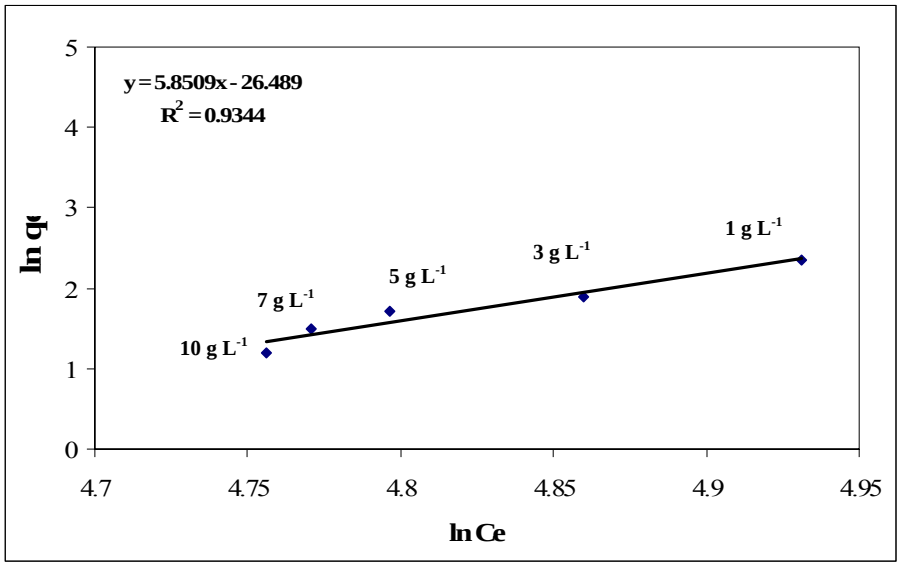

Figure 6.22. Adsorption of 2-CP on RNIP and the linearized best fit Freundlich isotherm.

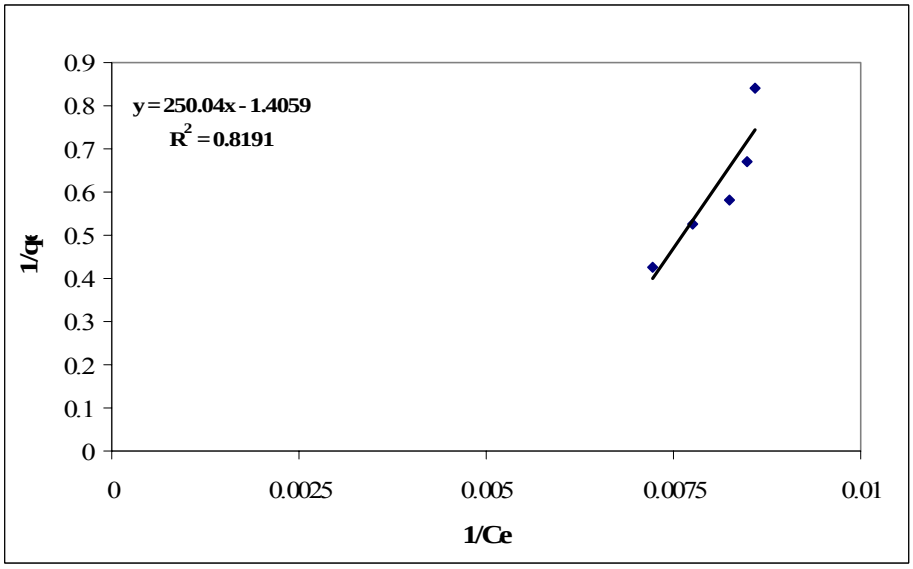

Figure 6.23. Adsorption of 2-CP on RNIP and the linearized best fit Langmuir isotherm.

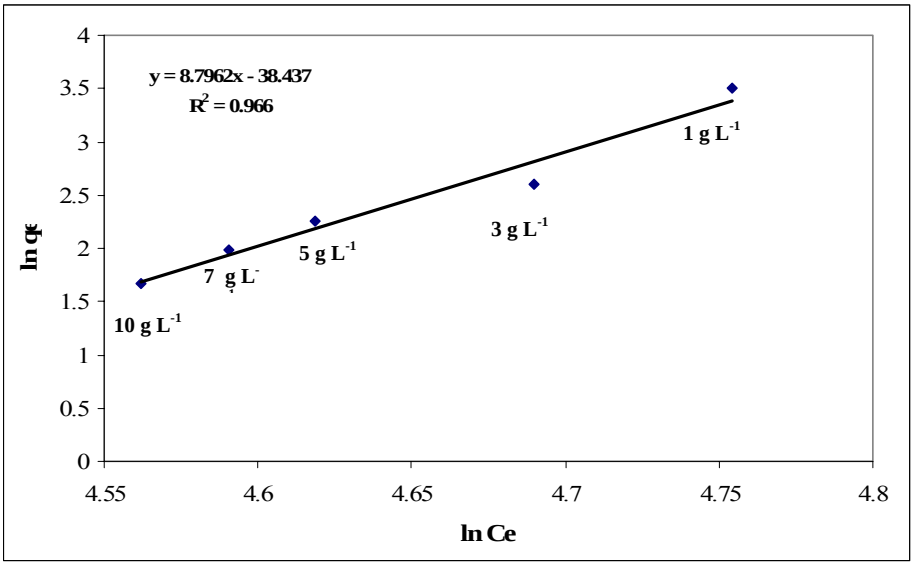

Figure 6.24. Adsorption of 2-CP on TiO_2 and the linearized best fit Freundlich isotherm.

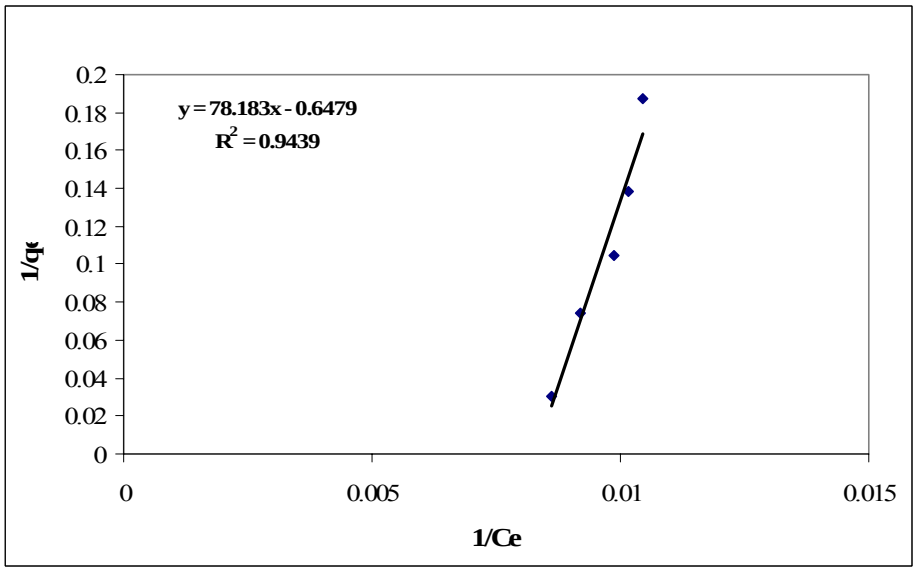

Figure 6.25. Adsorption of 2-CP on TiO_2 and the linearized best fit Langmuir isotherm.

6.4. The Use of Nano and Micro Particles in Combination with Ultrasound

6.4.1. Background Information

In this section results of the degradation of 2-Chlorophenol (2-CP) by the application of ultrasound alone and in combination with nanoparticles in powder form and in suspensions are presented. All experiments were run in Reactor 2 at pH 3. The nanoparticles considered include zero valent iron, as well as various iron, cupper and titanium oxides. To assess the optimal nanoparticle dose, a range of concentrations was investigated.

The particles used in these experiments are listed below:

Particle Suspensions:

- Fe^{2+} suspension prepared by using reagent grade Iron (II) Sulfate Heptahydrate, $FeSO_4.7H_2O$ (Merck, Germany) (Fenton type reagent)
- Cu^{2+} suspension prepared by using reagent grade Cupric Sulfate, $CuSO_4.5H_2O$ (EMD Chemicals, Germany) (Fenton-like type reagent)
- H-200 Zero Valent Iron (Hepure, USA)
- HC15 Zero Valent Iron (Hepure, USA)
- Ancor M-30/80 Zero Valent Iron (Hepure, USA)
- MD 24 Iron Oxide Particles (Koç University, Istanbul)

Nanoparticles :

- Ti(IV) Oxide Nanoparticles (99.7 % purity, Aldrich, Istanbul)
- Copper (II) Oxide Nanoparticles (Sigma-Aldrich, Istanbul)

Test samples of 150 μM 2-CP were prepared from the stock using ultra-pure milli-Q water. The effect of particle addition was tested by sonicating 2-CP solutions at concentrations of 0.025, 0.05, 0.10, 0.25 and 0.35 mM of Fenton type reagent, Fenton-like type reagent, H-200, HC15, and Ancor M-30/80. TiO_2 and CuO nanoparticles were added

in 1 g L^{-1}, 3 g L^{-1} and 5 g L^{-1} concentrations. The MD 24 concentrations synthesized at Koc University and added to the ultrasonic reactor were 0.0016, 0.016, 0.12, 0.40, 1.68 and 3.19 mg L^{-1}. In all experiments, the pH of the test solutions were adjusted to pH=3 after the addition of particles. The effect of hydrogen peroxide addition was tested by sonicating the test samples in the presence of H_2O_2/Fe^{2+} and H_2O_2/Cu^{2+} molar ratios of 2:1 and 4:1. Samples were withdrawn from the reactor for GC analysis.

6.4.2. Results and Discussion

Addition of a Fenton Type Reagent:

Argon-saturated solutions of 150 μM 2-CP were sonicated in the presence of 0.025, 0.05, 0.1, 0.25 and 0.35 mM Fe^{2+} for 45 minutes, and samples were collected in 5 minute intervals for GC analysis. The pH of the test samples were adjusted to pH=3 to eliminate the precipitation of $Fe(OH)_3$. The study of Kim and Vogelpohl (1996) reports the influence of pH on the decomposition of chlorophenols, stating that the rate of decomposition was significantly slowed down with pH increase as a consequence of lower dissolved fraction of iron species. The rate of ultrasonic decomposition of 2-CP in varying concentrations of Fe^{+2} and the estimated reaction rate constants are presented in Figure 6.26 and Table 6.17, respectively.

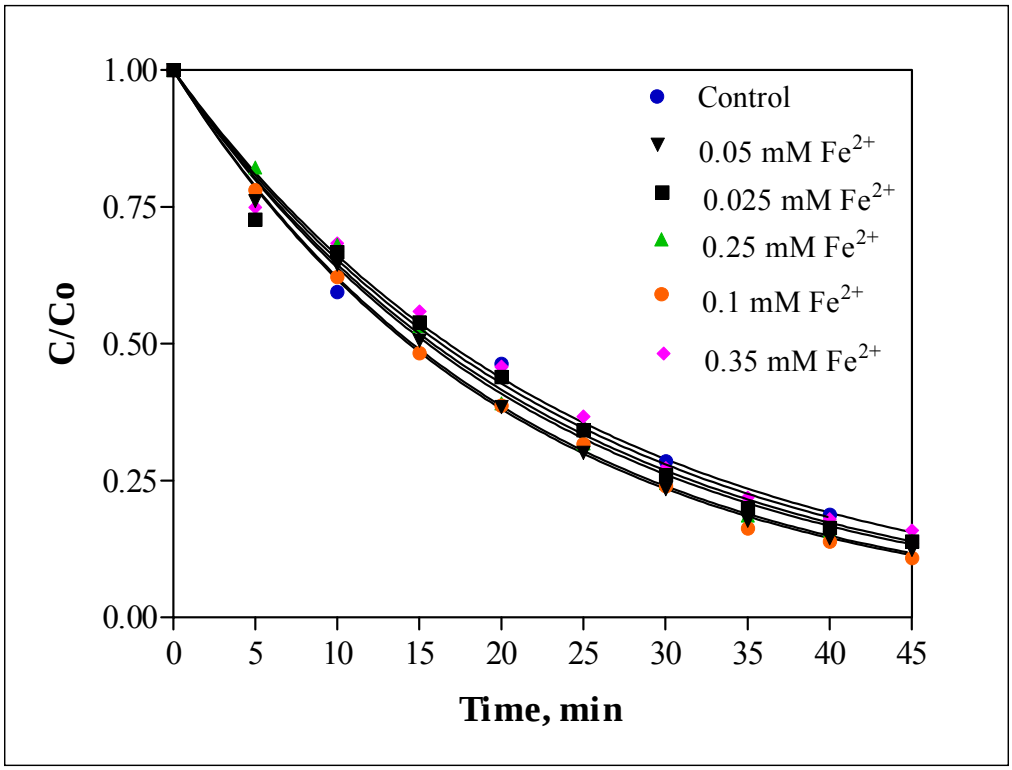

Figure 6.26. Variation of sonochemical decomposition rate of 2-CP with Fe^{2+} concentration. (Fe^{2+}=0 in Control, pH=3).

Table 6.17. The pseudo-first order decay rate coefficients for the data in Figure 6.26.

-k' x 10^{-2} (min^{-1})					
Control	**0.025 mM Fe^{2+}**	**0.05 mM Fe^{2+}**	**0.10 mM Fe^{2+}**	**0.25 mM Fe^{2+}**	**0.35 mM Fe^{2+}**
4.09	4.38	4.76	**4.82**	4.47	4.13

The reaction chemistry expected to occur during these experiments is as follows:

$$H_2O \xrightarrow{)))))} \bullet OH + \bullet H \quad (6.9)$$

$$2\bullet OH \longrightarrow H_2O_2 \quad (6.10)$$

$$Fe\ (II) + H_2O_2 \longrightarrow Fe\ (III) + OH^- + \bullet OH \quad (6.11)$$

$$\bullet OH + Fe\ (II) \longrightarrow Fe\ (III) + OH^- \quad (6.12)$$

$$Fe\ (III) + H_2O_2 \longrightarrow Fe\ (II) + \bullet HO_2 + H^+ \quad (6.13)$$

$$\bullet HO_2 + Fe\ (III) \longrightarrow Fe\ (II) + H^+ + O_2 \quad (6.14)$$

The •OH radicals formed during the sonolysis of water recombine to form hydrogen peroxide. Upon the addition of $FeSO_4.7H_2O$, decomposition of sonochemically produced H_2O_2 is accelerated through Fenton's reaction (Equation 6.11), resulting in the formation of additional •OH radicals.

The data show that Fe^{2+} addition between 0.025 and 0.1 mM slightly enhanced the rate of 2-CP degradation, but the enhancement ceased when the concentration exceeded 1 mM. This can be explained by the reaction of excess Fe^{2+} with •OH to produce Fe^{3+} as in Equation 6.12. The feature of an optimal dose range for iron catalyst is a characteristic of Fenton's reagent (Pera-Titus et al., 2004).

Previous work of Esplugas et al. (2004) confirms the efficiency of Fenton reactions in the reduction of chemical oxygen demand (COD) and total organic carbon (TOC) of chlorophenols. The study of Perz-Moya et al. (2007) that involves the application of Fenton, Fenton-like and Photo-Fenton processes for 2-Chlorophenol degradation has also shown that the selection of the correct Fenton reagent load is the most important aspect for the treatment process. They also pointed out that excess of Fe^{2+} or H_2O_2 causes detrimental effects due to their reactions with •OH radicals that are required for the direct oxidation of contaminants.

Addition of H-200 Zero Valent Iron Suspension:

In these experiments argon-saturated solutions of 150 μM 2-CP were sonicated in the presence of 0.025, 0.05, 0.10, 0.25 and 0.35 mM H-200 for 45 minutes, and samples were collected at 5 min intervals for GC analysis. The pH of the test samples were 3. Ultrasonic decomposition profiles of 2-CP as a function of H-200 zero-valent iron concentration and the corresponding rate constants are presented in Figure 6.27 and Table 6.18, respectively.

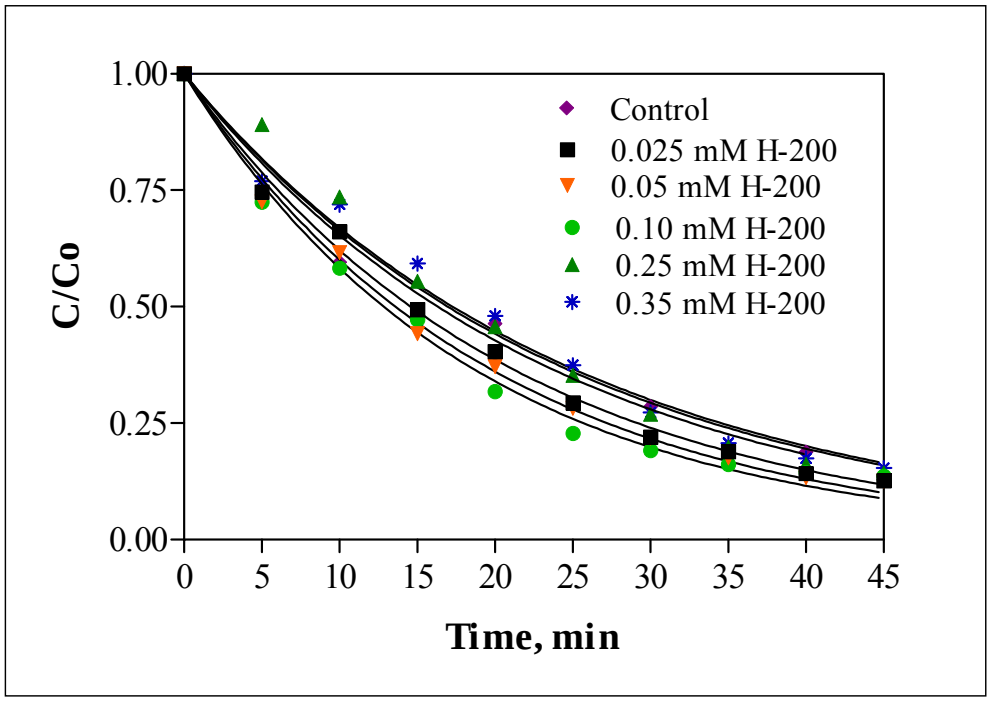

Figure 6.27. Variation of sonochemical decomposition rate of 2-CP with H-200 zero valent iron concentration (H-200=0 in Control, pH=3).

Table 6.18. The pseudo-first order decay rate coefficients for the data in Figure 6.27.

-k' x 10^{-2} (min^{-1})					
Control	**0.025 mM H-200**	**0.05 mM H-200**	**0.10 mM H-H-200**	**0.25 mM H-200**	**0.35 mM H-200**
4.09	4.75	5.10	**5.39**	4.08	4.01

It was found that addition of H-200 at 0.025-0.10 mM enhanced the rate of degradation, but further increases in H-200 reduced it. Comparison of 2-CP degradation rate in the presence of H-200 and Fe^{2+} shows that in both cases the highest reaction rate constants were obtained at 0.1 mM of the reagent. However, the enhancement in presence of H-200 was greater than that in the presence of Fe^{2+}.

The study of Chung et al. (2007) that focused on the treatment of pentachlorophenol-contaminated soil using nanosacle ZVI with H_2O_2 has also shown that increase in the amount of ZVI added resulted in an increase in the reaction rate of the contaminant. This is

explained by the increase in the quantity of Fe^{2+} ions released by oxidation of Fe^{0} and the enhancement in OH radicals by the catalytic action of Fe^{2+}.

A study has also been completed by ARS Technologies (Hepure, web) to compare the reactivity of several different ZVI powders. They included the H-200 sponge iron, cast iron, and other proprietary ZVI powders of very fine particle sizes. The study was conducted using both sediments and actual groundwater contaminated with TCE. They found that H-200 showed the most significant reduction, and generated little or no daughter products such as cis-1,2-DCE and vinyl chloride compared to the other irons (Hepure, web). They also concluded that the internal porosities, the carbon molecules and other inclusions found within H-200's structural matrix further enhanced its reactivity exceeding that of more commonly used granular iron powders (Hepure, web).

Addition of HC15 Zero Valent Iron Suspension:

In these experiments, argon-saturated solutions of 150 μM 2-CP were sonicated in the presence of 0.025, 0.05, 0.10, 0.25 and 0.35 mM HC15 for 45 minutes, and samples collected at 5 min intervals were analyzed by GC. All test samples were adjusted to pH 3.0 before sonication. The rate of ultrasonic decomposition of 2-CP in varying concentrations of HC15 and the estimated reaction rate constants are presented in Figure 6.28 and Table 6.19, respectively.

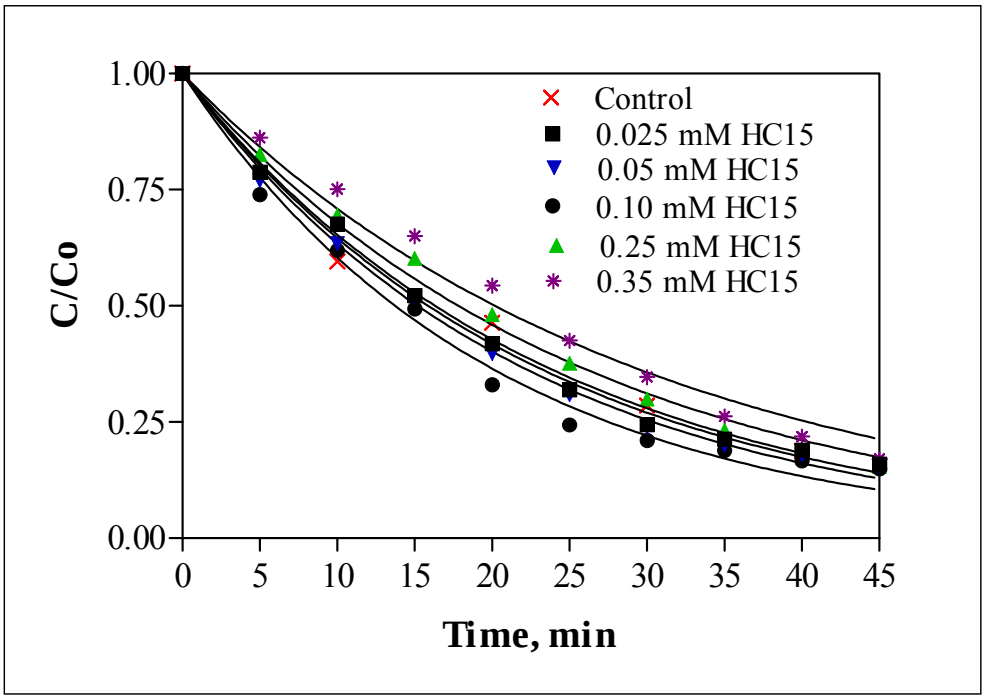

Figure 6.28. Variation of sonochemical decomposition rate of 2-CP with HC15 zero valent iron concentration (HC15=0 in Control, pH=3).

Table 6.19. The pseudo-first order decay rate coefficients for the data in Figure 6.28.

-k' x 10^{-2} (min^{-1})					
Control	**0.025 mM HC15**	**0.05 mM HC15**	**0.10 mM HC15**	**0.25 mM HC15**	**0.35 mM HC15**
4.09	4.36	4.56	**5.04**	3.89	3.43

It was found again that maximum rate of decomposition occurred in the presence of 0.10 mM HC15, and the rate was slowed down with further increases in the reagent dose. Surprisingly, the rate of reaction at 0.25 mM and 0.35 mM HC15 was even lower than that in the Control having no iron. This must be due to inhibition of the reaction by the excess of some interfering agents (i.e. the organic impurities used in the manufacture of HC15, or the byproducts of oxidation that may scavenge some of the OH radicals at the interfacial area.

Addition of Ancor M-30/80 Zero Valent Iron Suspension:

In these experiments argon saturated solutions (pH=3.0) of 150 µM 2-CP were sonicated in the presence of 0.025, 0.05, 0.10, 0.25 and 0.35 mM Ancor for 45 minutes, and samples analyzed in the GC. The rate of ultrasonic decomposition of 2-CP in varying concentrations of Ancor and the estimated reaction rate constants are presented in Figure 6.29 and Table 6.20, respectively.

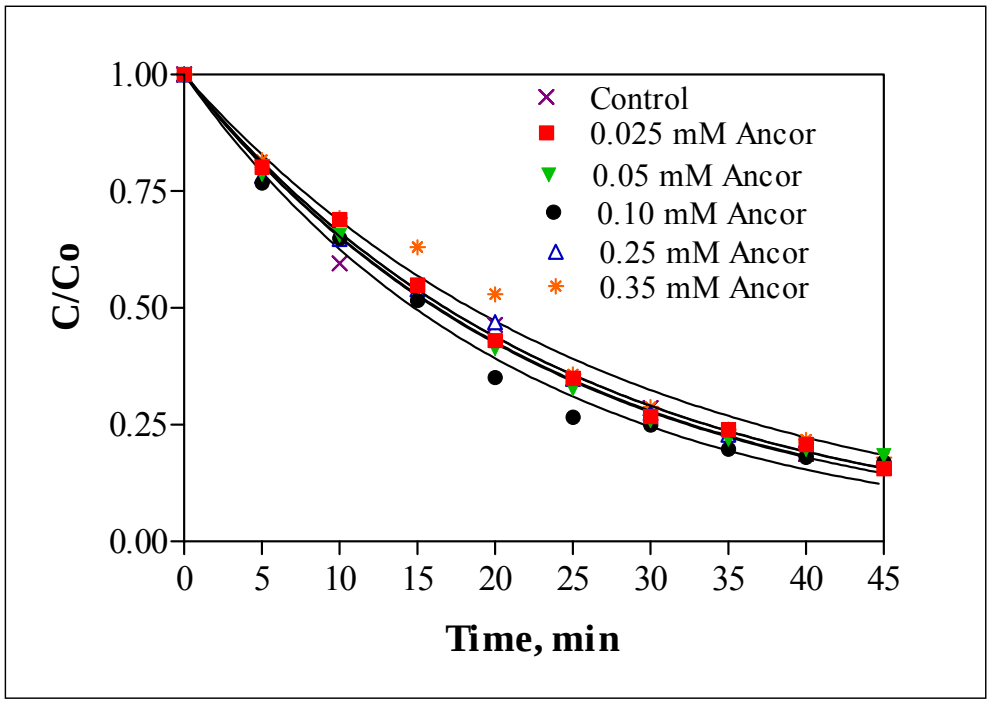

Figure 6.29. Variation of sonochemical decomposition rate of 2-CP with Ancor zero valent iron concentration (Ancor=0 in Control, pH=3).

Table 6.20. The pseudo-first order decay rate coefficients for the data in Figure 6.29.

-k' x 10^{-2} (min^{-1})					
Control	**0.025 mM Ancor**	**0.05 mM Ancor**	**0.10 mM Ancor**	**0.25 mM Ancor**	**0.35 mM Ancor**
4.09	4.12	4.28	**4.68**	4.12	3.75

It was found that the rate of 2-CP decomposition in the presence of Ancor was similar to that observed with the previous reagents. The highest rate of reaction was

achieved in the presence of 0.10 mM Ancor and the rate was reduced below that of the Control when the dose of Ancor was 0.35 mM.

Addition of a Fenton-Like Reagent:

To investigate the impact of Fenton-like reagents on the efficiency of ultrasonic decomposition of 2-CP, experiments were conducted in the presence of a Cu^{2+} suspension prepared with Cupric Sulfate, $CuSO_4.5H_2O$. The impact of reagent dose was tested by sonicating argon-saturated solutions of 2-CP (pH=3.0) in the presence of 0.025, 0.05, 0.10, 0.25 and 0.35 mM of Cu^{2+}. The rate of ultrasonic decomposition of 2-CP in varying concentrations of Cu^{2+} and the estimated reaction rate constants are presented in Figure 6.30 and Table 6.21, respectively.

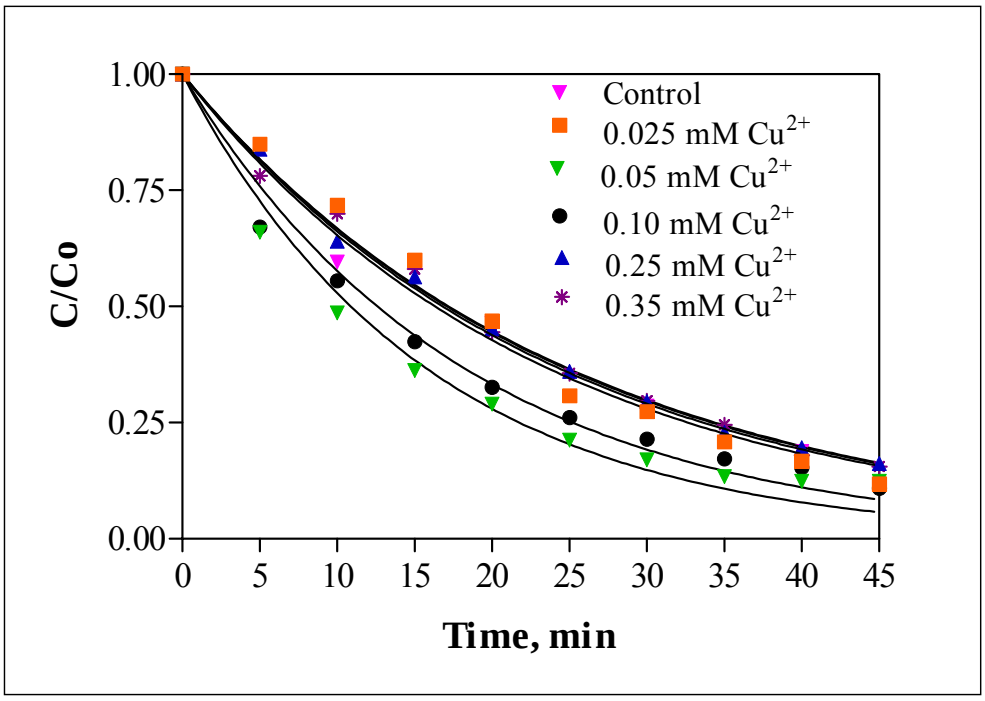

Figure 6.30. Variation of sonochemical decomposition rate of 2-CP with Cu^{2+} concentration (Cu^{2+}=0 in Control, pH=3).

Table 6.21. The pseudo-first order decay rate coefficients for the data in Figure 6.30.

-k' x 10^{-2} (min^{-1})					
Control	**0.025 mM Cu^{2+}**	**0.05 mM Cu^{2+}**	**0.10 mM Cu^{2+}**	**0.25 mM Cu^{2+}**	**0.35 mM Cu^{2+}**
4.09	4.12	**6.37**	5.50	4.05	4.03

The reaction chemistry expected to occur in these experiments is as follows:

$$Cu(II) + H_2O_2 \longrightarrow Cu\ (I) + \bullet HO_2 + H^+ \quad (6.15)$$

$$Cu\ (I) + H_2O_2 \longrightarrow Cu\ (II) + \bullet HO + OH^- \quad (6.16)$$

$$Cu\ (II) + \bullet HO_2 \longrightarrow Cu\ (I) + O_2 + H^+ \quad (6.17)$$

Principally, cuprous ions react with H_2O_2 to form OH radicals that readily attack the contaminants in the solution. It was found that unlike with the impact of Fenton and ZVI nanoparticles, the optimum Cu^{2+} concentration that yielded maximum degradation of 2-CP was 0.05 mM.

The study of Ozawa and Hanaki (1991) also confirms the production of •OH radicals by homogeneous copper catalysts in the presence of hydrogen peroxide. Moreover, Mantzavinos (2003) reports in his study that the use of heterogeneous copper catalysts in the presence of hydrogen peroxide enhances the removal of organic pollutants.

Comparison of the Fenton and Fenton-like Catalysts:

Comparison of sonochemical degradation rate constants of 2-CP in presence of Fenton and Fenton-like reagents is presented in Figure 6.31.

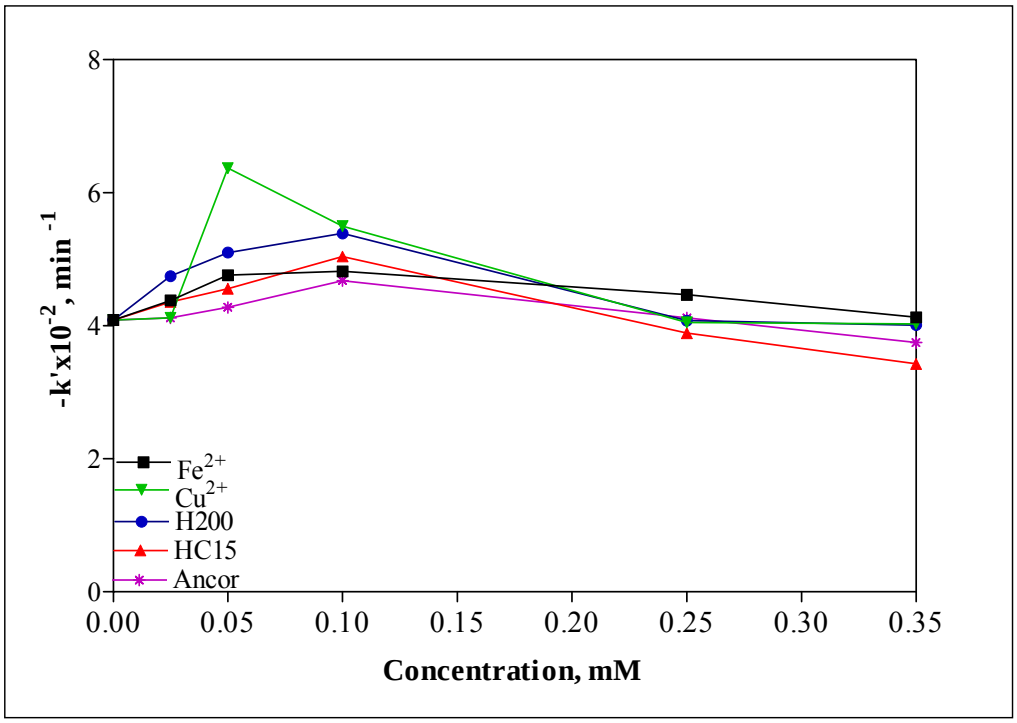

Figure 6.31. Variation of the pseudo-1st order decomposition rate constant of 2-CP with the type and concentration of Fenton and Fenton-like catalysts.

Effect of Hydrogen Peroxide Addition:

H_2O_2 plays a major role in Fenton and Fenton-like reactions in accordance with the reaction schemes in Equations 6.13-6.16. In the previous experiments using Fe and Cu particles, no H_2O_2 was added based on the basic principle that H_2O_2 is in-situ generated during water sonolysis. In this section, we report the impact of external H_2O_2 addition on the sono-Fenton decomposition of 2-CP. The mode of addition was such that a molar ratio of 2:1 and 4:1 was fixed as H_2O_2/Fe^{2+} and H_2O_2/Cu^{2+} in each set of experiment. The results are plotted in Figure 6.32 and 6.33 for Fe and Cu, respectively. The estimated reaction rate constants in presence of external and internal H_2O_2 are given in Table 6.22 and 6.23 for Fe^{2+} and Cu^{2+}, respectively.

It was found that doubling the quantity of external H_2O_2 provided a 10-fold increase in the rate of sono-fenton reactions and a 7-fold increase in that of sono-Fenton-like reactions with Cu^{2+}. The data also show that the quantity of internal H_2O_2 (arising from

insitu generation by water sonolysis) is insufficient to induce effective Fenton and Fenton-like reactions in solution.

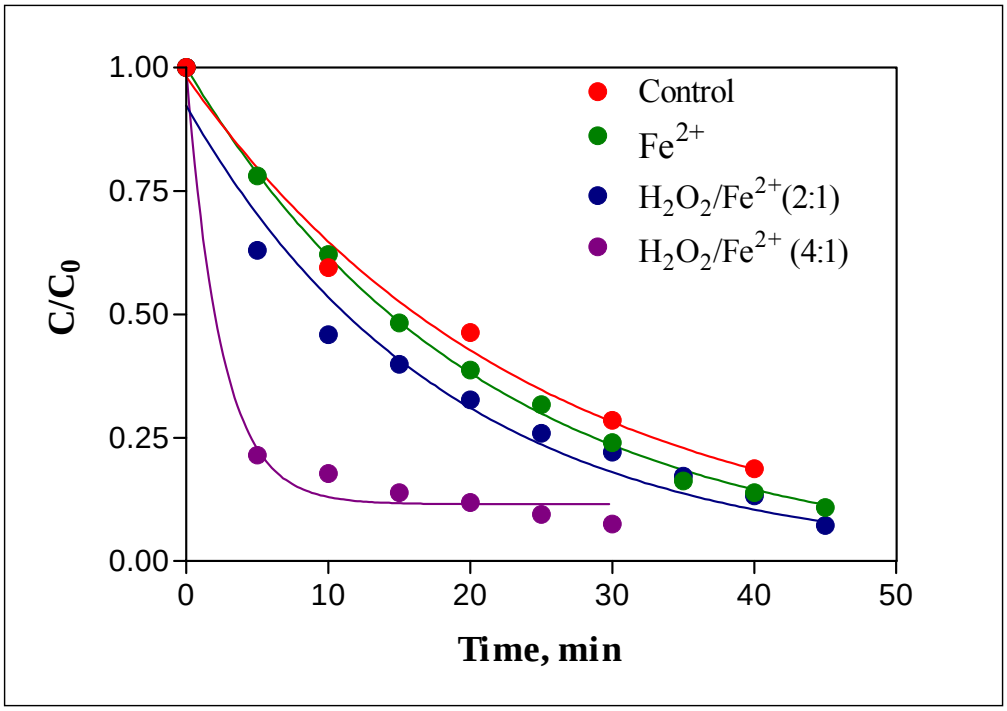

Figure 6.32. Impact of H_2O_2 addition on sono-Fenton decomposition of 2-CP. The concentration of Fe^{+2} in all sets is 0.10 mM. ("Control" refers to ultrasound without Fe^{+2})

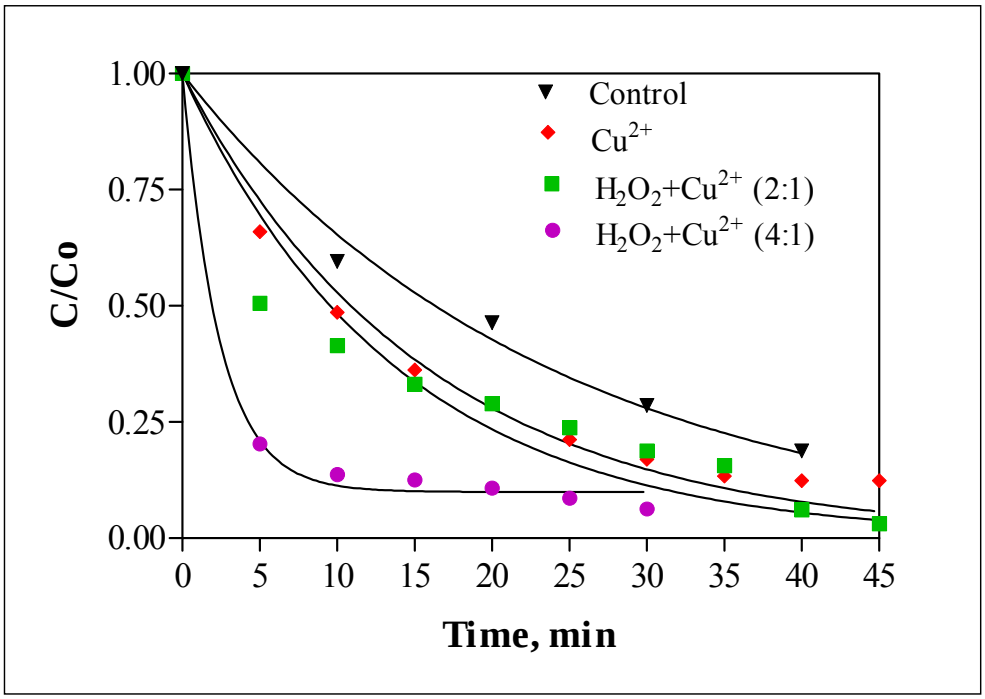

Figure 6.33. Impact of H_2O_2 addition on sono-Fenton-like decomposition of 2-CP. The concentration of Cu^{2+} in all sets is 0.05 mM. ("Control" refers to ultrasound without Cu^{2+})

Table 6.22. Sono-Fenton reaction rate constants for the decay of 2-CP in presence of external and internal H_2O_2.

-k' x 10^{-2} (min^{-1})			
Control	**Fe^{2+}**	**Fe^{2+}/H_2O_2 (2:1)**	**Fe^{2+}/H_2O_2 (4:1)**
4.09	4.82	5.45	41.0

Table 6.23. Sono-Fenton-like reaction rate constants for the decay of 2-CP in presence of external and internal H_2O_2.

-k' x 10^{-2} (min^{-1})			
Control	**Cu^{2+}**	**Cu^{2+}/H_2O_2 (2:1)**	**Cu^{2+}/H_2O_2 (4:1)**
4.09	6.37	7.25	41.95

Addition of MD 24 Nanoparticles:

In these experiments the effect of MD 24 nanoparticles (also used in mobility experiments) were tested on sonochemical decomposition of 2-CP (C0=150 µM) by adding 0.0016, 0.016, 0.12, 0.40, 1.68 and 3.19 mg L^{-1} MD 24 into the test solutions at pH 3.0. 2-CP degradation rate profiles and the corresponding rate constants resulting from the addition of MD 24 is presented in Figure 6.34 and Table 6.24, respectively.

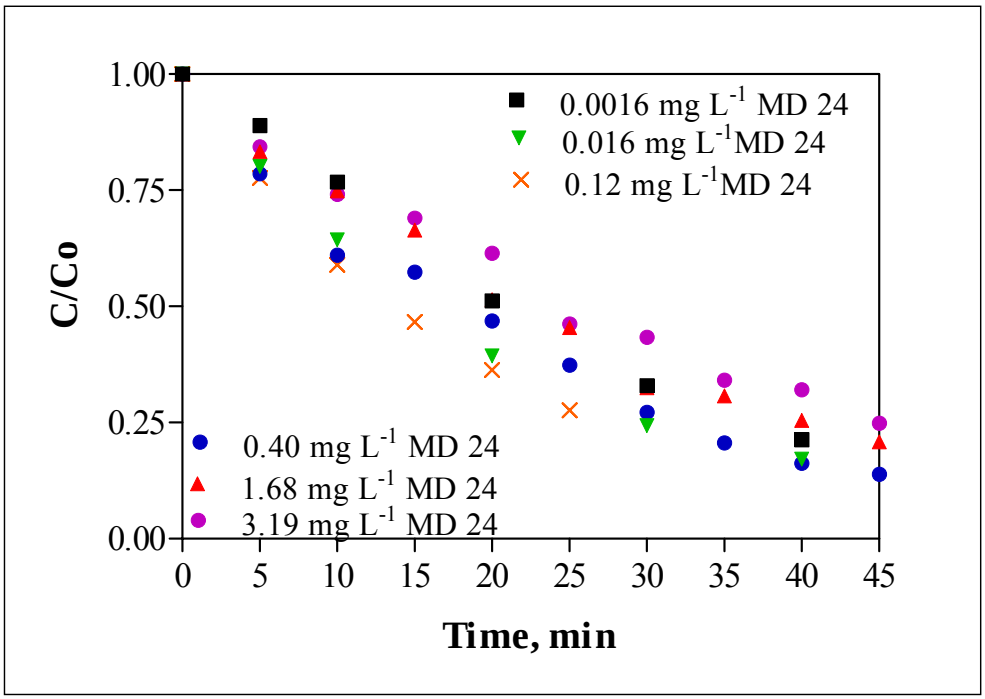

Figure 6.34. The rate of sonochemical decomposition of 2-CP as a function of MD 24 concentration.

Table 6.24. The pseudo-first order decay rate coefficients for the data in Figure 6.34.

-k' x 10^{-2} (min^{-1})						
Control (MD 24=0)	**0.0016 mg L^{-1}**	**0.016 mg L^{-1}**	**0.12 mg L^{-1}**	**0.40 mg L^{-1}**	**1.68 mg L^{-1}**	**3.19 mg L^{-1}**
4.09	3.43	4.57	**5.13**	4.25	3.22	2.87

It was found that the rate of decomposition at the lowest test concentration of MD 24 was lower than the rate at no MD 24 (Control), but it increased with further additions up to 0.12 mg L^{-1}. At higher doses, the rate was found to slow down again reaching much lower values than that of Control when MD 24 was ≥1.68 mg L^{-1}. The observed profile might be due to a variety of factors such as different impacts of the solution matrix at different concentrations of the particles and different particle size distributions at different dilution rates.

Addition of Titanium Dioxide:

The impact of TiO_2 nanoparticles on sonochemical decay of 2-CP was tested in a solution of 150 µM 2-CP at pH 3.0 by adding 1, 3, and 5 g L^{-1} TiO_2. The data and the estimated rate constants are presented in Figure 6.35 and Table 6.25, respectively.

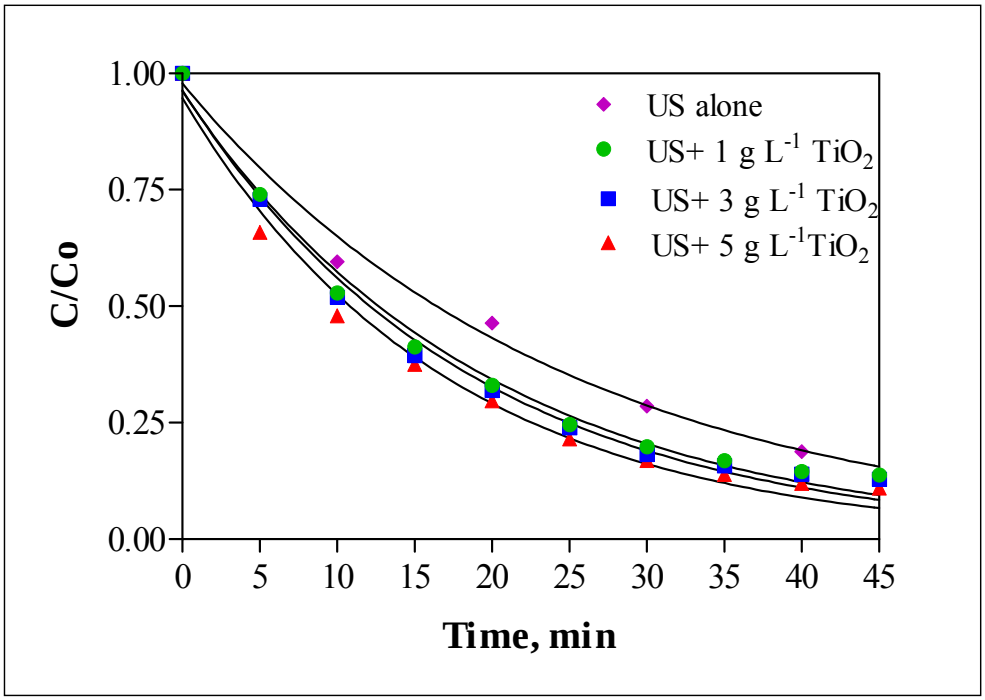

Figure 6.35. Sonochemical rate of 2-CP decomposition in presence of varying concentrations of TiO_2 nanoparticles.

Table 6.25. The pseudo-first order decay rate constants for the data in Figure 6.35.

-k' x 10^{-2} (min^{-1})			
TiO_2 concentration			
0 g L^{-1}	**1 g L^{-1}**	**3 g L^{-1}**	**5 g L^{-1}**
4.09	5.38	5.63	6.25

It was found that addition of TiO_2 catalyzes the sonochemical decomposition of 2-CP as was also reported by Shirgaonkar and Pandit (1998) in a study with chlorophenols. However, Ragaini et al. (2001) have found that the efficiency of sonochemical reactions carried out under low frequency (20 kHz) and low sonication power could not be improved by the addition of suspended particles. In our case, the improvement must be due to higher applied frequency, yielding shorter bubble collapse duration and larger rate of radical ejection to the interface. In addition, we observed good adsorption properties of 2-CP on TiO_2 surfaces (Chapter 6.3) that must have enhanced the rate of interfacial reactions.

Addition of Copper Oxide:

The impact of CuO nanoparticles on sonochemical decay of 2-CP was tested in a solution of 150 μM 2-CP at pH 3.0 by adding 1, 3, and 5 g L^{-1} CuO. The data and the estimated rate constants are presented in Figure 6.36 and Table 6.26, respectively.

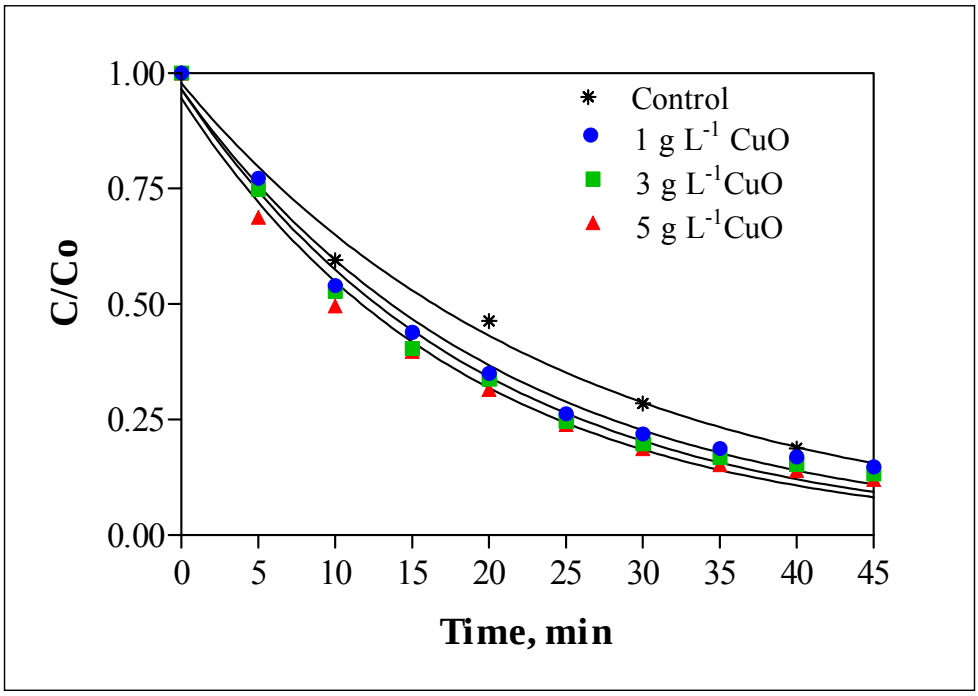

Figure 6.36. Sonochemical rate of 2-CP decomposition in presence of varying concentrations of CuO nanoparticles.

Table 6.26. The pseudo-first order decay rate constants for the data in Figure 6.36.

-k' x 10^{-2} (min^{-1})			
CuO concentration			
0 g L^{-1}	**1 g L^{-1}**	**3 g L^{-1}**	**5 g L^{-1}**
4.09	5.02	5.39	5.78

Generation of hydroxyl radicals and their oxidative role in the presence of heterogeneous copper catalysts was also investigated recently by Kim and Metcalfe (2007). The copper oxide (CuO) they used was either in powder form, supported over γ-alumina or a in mixture of ZnO supported on γ –alumina. They found that each form of the catalyst was capable of generating OH radicals in combination with H_2O_2. They concluded OH radicals were abundant near the surface of the catalysts leading to non-selective oxidation of both target compounds and the oxidation products.

7. CONTINUOUS-FLOW EXPERIMENTS FOR THE IN-SITU REMEDIATION OF GROUNDWATER USING NANOPARTICLES

The aim of this part of the study was to investigate the fate and transport of the nanoparticles in the subsurface, and the applicability of ultrasound in combination with nanoparticles for groundwater remediation. In the past few years, engineered nanoparticles have found their way into various applications such as electronics and biomedical engineering. The rapid rise in the synthesis of these nanoparticles will inevitably lead to their advert or inadvertent release into the subsurface environment. Reactive nanoparticles are also being considered as a promising technology for the in-situ remediation of contaminated groundwater resources. A brief review of recent studies that used reactive nanoparticles for the remediation of groundwater contaminated by organic compounds was presented in Chapter 3.3. Understanding the processes responsible for the mobility of these particles in porous media is an essential step in assessing the risks of exposure to these engineered materials and in the development of reactive transport models that can be used as tools for the evaluation and optimization of in-situ groundwater remediation with nanoparticles.

7.1. Selection of the Nanoparticles

Controlling particle size and preventing aggregation between particles have received considerable attention with the increasing need of applications for well-dispersed nanoparticles with uniform size, uniform physical and chemical properties. One method of nanoparticle stabilization is through surface coating with polymeric materials. Carboxylic acid groups offer multiple adsorption sites while other free groups provide water solubility and surface functionality to the particle. These free carboxylic acid groups on the surface also maintain electrostatic repulsion that prevents aggregation. The stability of the polymer coating on the surface is very important for particles to resist agglomeration.

As mentioned in Chapter 4.1, several nano and microparticles were purchased to be used in the continuous flow experiments. The nanoparticles used in the continuous flow transport experiments were MD 24, MD 59 and MD 60 ironoxide particles obtained from

Koç University, Istanbul. These particles were selected due to their low reactivity and readily measurable size by our nanoparticle size analyzer (Brookhaven 90Plus). The latter property is due to the use of poly acrylic acid sodium in its manufacture as a polymeric stabilizer to provide electrostatic and steric repulsion against particle aggregation.

To investigate the change in particle sizes with dilution; 1/10, 1/20, 1/100, 1/200, 1/500, 1/1000 and 1/10000 dilutions of MD 24, MD 59, and MD 60 were prepared and analyzed by the nanoparticle size analyzer. The measurements were conducted after the nanoparticle suspensions were exposed to sonication in an ultrasonic bath for 8 minutes. The results are given in Table 7.1. The yellow color indicates immeasurable runs. Generally, the effective particle size did not change significantly with dilution. Among the three nanoparticles considered, the measurements of MD 60 were the most reliable. Moreover, MD 60 was found to be the most stable nanoparticle and, hence, was chosen as the model nanoparticle to be used throughout the flow-through experiments.

Table 7.1. Effect of dilution factor on stability of nanoparticles and particle sizes.

Dilution Factor	Runs	MD 24 Effective Diameter, nm	MD 59 Effective Diameter, nm	MD 60 Effective Diameter, nm
Stock - 1:1 After Sonication	1	79.9	458.5	158.8
	2	72.8	451.8	148.5
	3	70.4	726.7	147
1:10	1	73.5		145.1
	2	69.1		146.4
	3	70.2		140.5
1:20	1	76.4	475.6	156.8
	2	72.9	365.5	145.9
	3	73.3	290.8	137.5
1:100	1	79.8	0	161.5
	2	73.8	663.2	151.6
	3	73.6		144.9
1:200	1	79.9	62.1	163.9
	2	77.7	0	151.1
	3	75.4		146.9
1:500	1	89.3	187.6	175
	2	84.5	175.4	166.7
	3	82.7	165	156.7
1:1000	1	97.9	459.5	173.8
	2	94.0	175.4	162.6
	3	80.7	165	155.9
1:10000	1			188.4
	2			287.7
	3			390.7

Figure 7.1 through 7.7 show the nanoparticle size distribution of the stock suspension at different levels of dilution. It is seen that the size distribution is bimodal with two distinct populations. For the stock suspension, the average sizes of these two distributions are about 72 nm and 280 nm with an effective size of 150 nm. We also observed a trend of size increase with dilution, but the change was relatively small due to the presence acrylic acid that acted as a stabilizer. Size distributions of the stock MD 60 suspension before and after various dilution rates are presented in Figure 7.8 as fractions by volume.

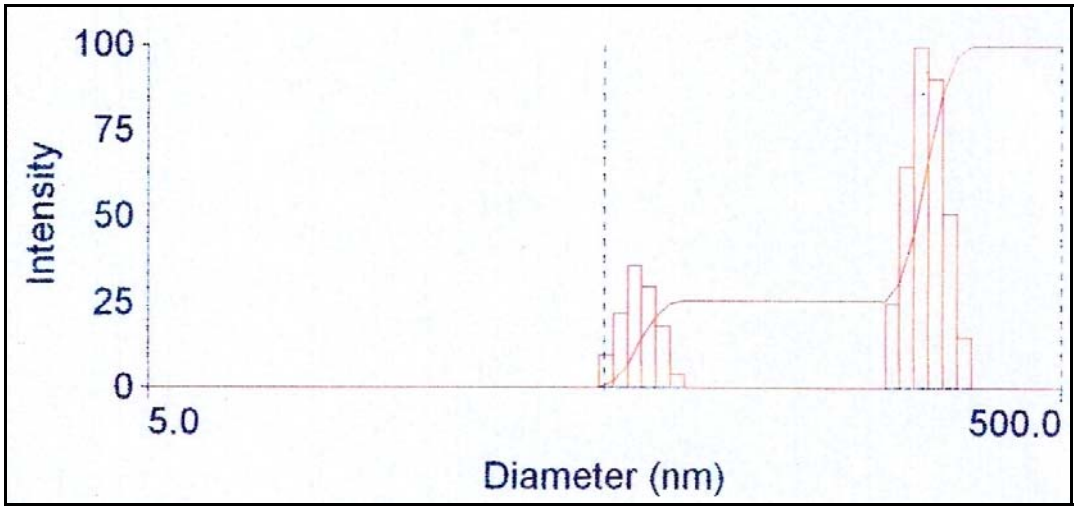

Figure 7.1. Particle size distribution of stock MD 60.

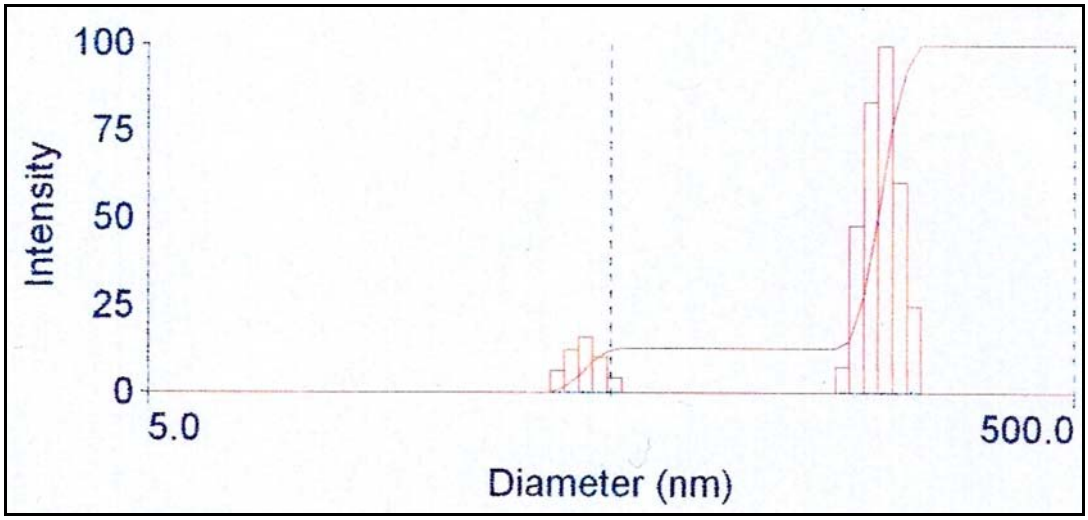

Figure7.2. Particle size distribution of 1/10 diluted MD 60.

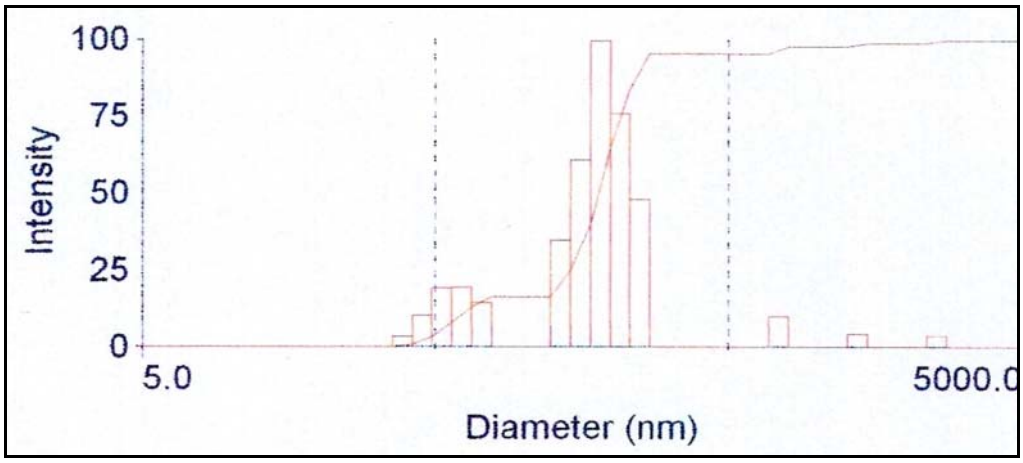

Figure 7.3. Particle size distribution of 1/20 diluted MD 60.

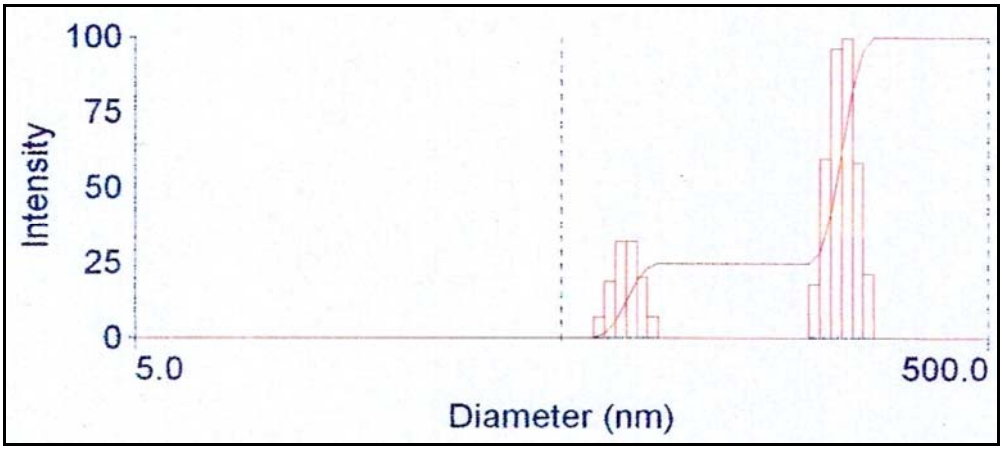

Figure 7.4. Particle size distribution of 1/100 diluted MD 60.

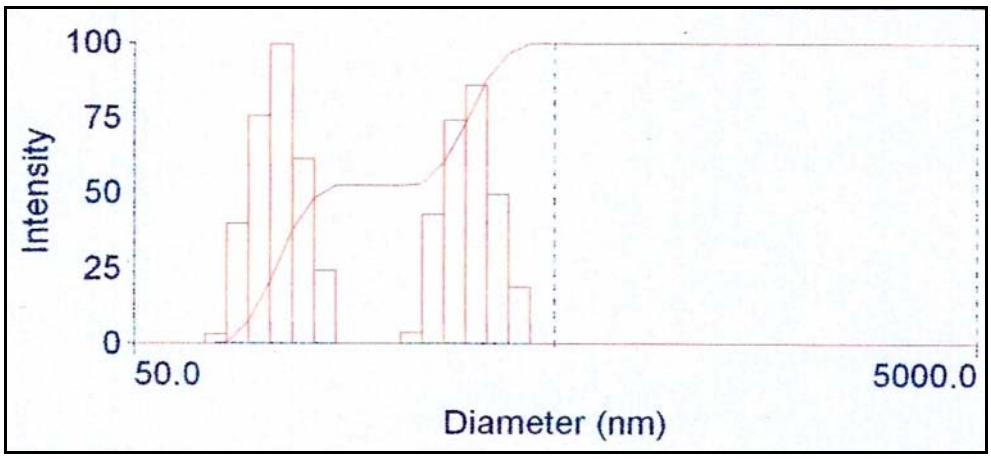

Figure 7.5. Particle size distribution of 1/200 diluted MD 60.

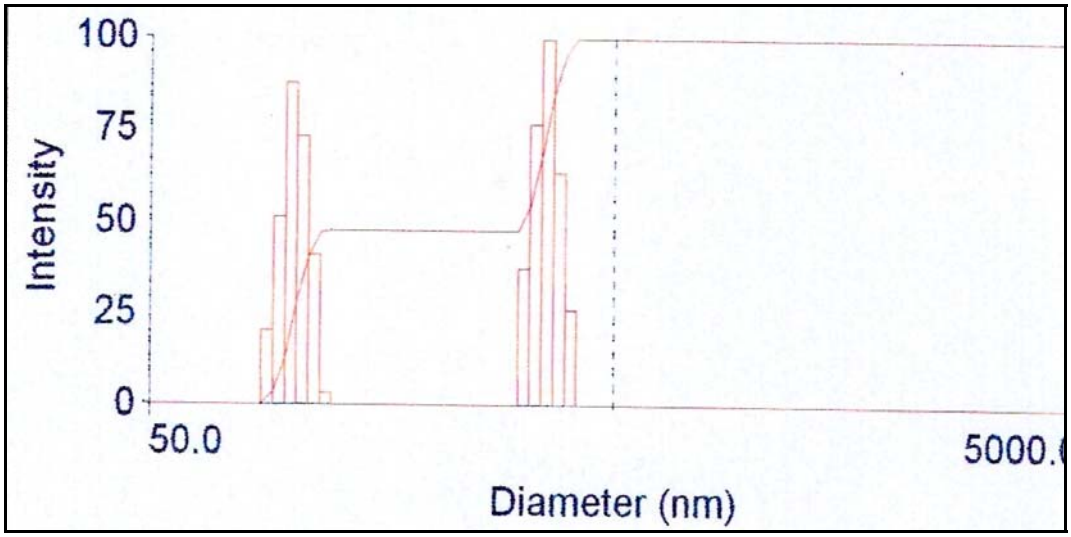

Figure 7.6. Particle size distribution of 1/500 diluted MD 60.

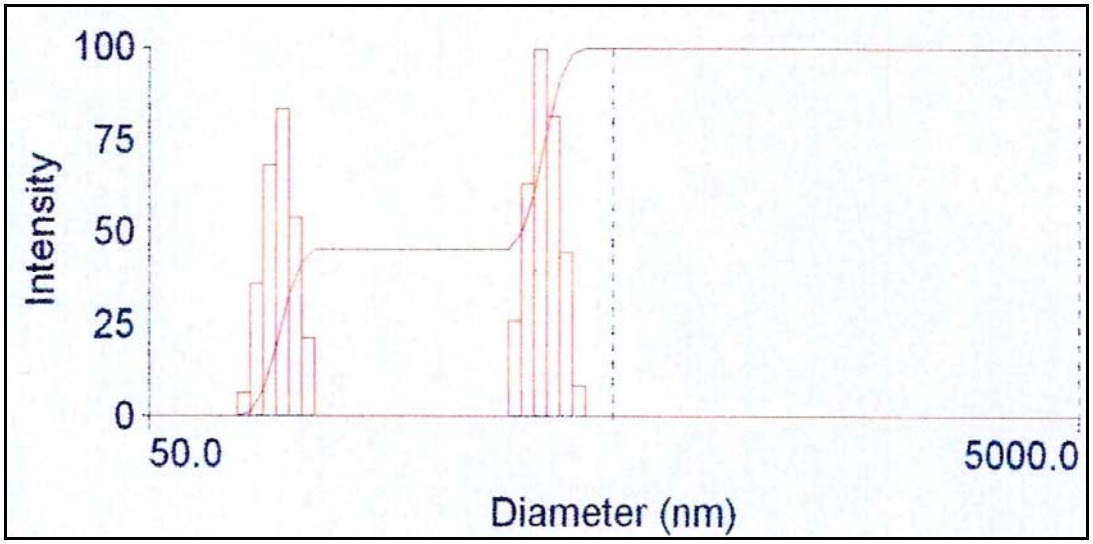

Figure 7.7. Particle size distribution of 1/1000 diluted MD 60.

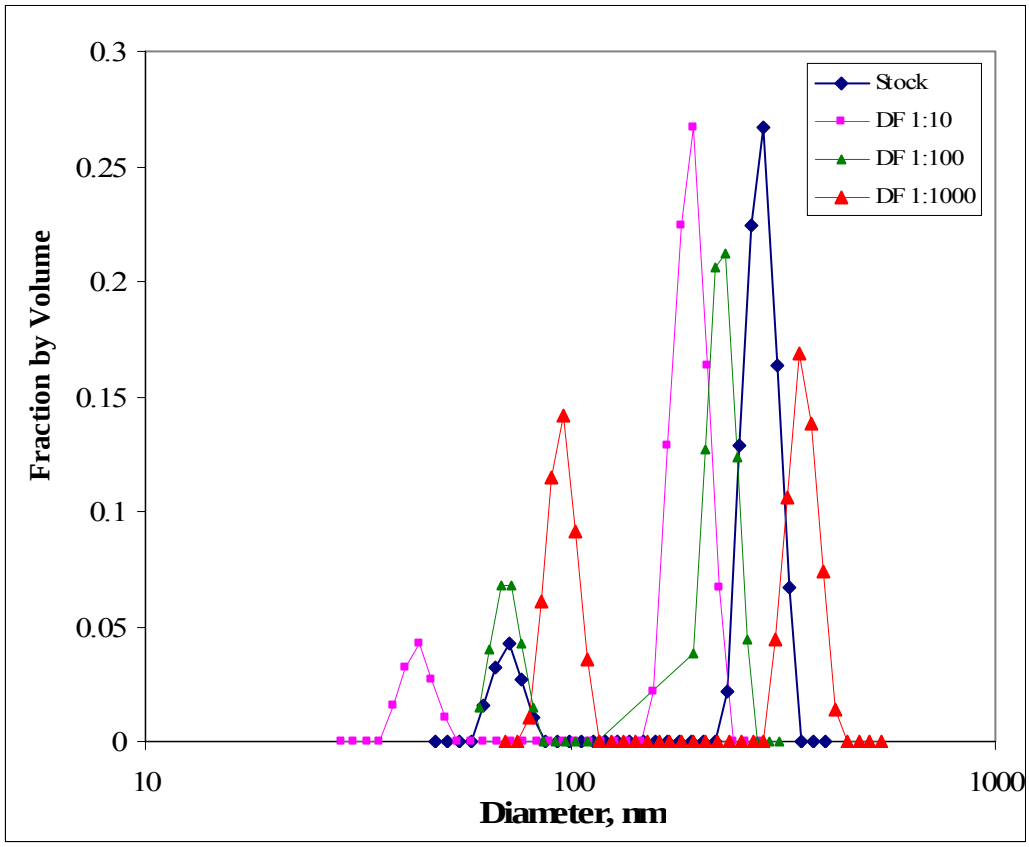

Figure 7.8. Particle size distribution of MD 60 and its diluted suspensions as fraction by volume.

The reliability of the data was checked by running the MD 60 measurements with another version of Brookhaven 90 Plus Size Analyzer at Boğaziçi University Advanced Technologies Research and Development Center. The results are presented in Table 7.2. The size distributions of the stock and the diluted suspensions are also given as fractions by volume in Figure 7.9.

Table 7.2. Results of MD 60 particle size analysis in another lab (B.U. Advanced Technologies, Research and Development Center).

Dilution Factor	**Runs**	**MD60 Effective Diameter, nm**
Stock - 1:1 After Sonication	1	147.8
	2	147.6
	3	147.3
1:10	1	145.9
	2	144.3
	3	140.6
1:100	1	148.5
	2	145.2
	3	144.8
1:1000	1	145.0
	2	146.2
	3	145.4
1:10000	1	160.5
	2	160.3
	3	176.8

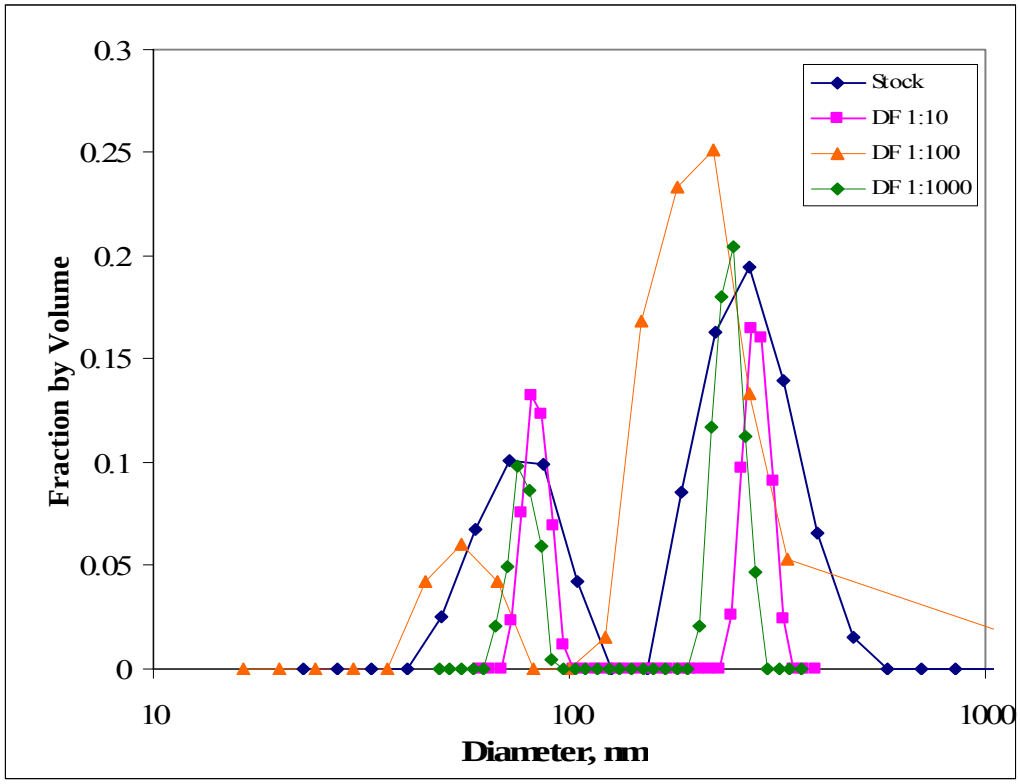

Figure 7.9. Particle size distribution of MD 60 and its diluted suspensions as fraction by volume (analysis carried at B.U. Advanced Technologies, Research and Development Center).

Attempts to measure the size of other nanoparticles with the Brookhaven 90 Plus were only partially successful. As a result, we decided to use only MD 60 ironoxide particles in mobility experiments due to the importance of the size on the transport of nanoparticles.

Milli-Q water that has been in contact with the sand in the CF tank and column was also analyzed by the Nanoparticle Size Analyzer and no measurable nanoparticles were observed in the samples. Hence, it is assumed that the ironoxide nanoparticles are the only nanoparticles present in the solutions transported through the tank and column.

Since the nanoparticles used in mobility tests were of ironoxide origin, their iron content was determined as described in Chapter 4.3. The results are given in Table 7.3.

Table 7.3. Iron concentrations of nanoparticle suspensions.

Nanoparticle Suspension	Iron, mg L^{-1}
MD 24	1597
MD 59	1168
MD 60	3884

7.2. Tracer Mobility Experiments

The purpose of the mobility experiments was to investigate the mobility of nanoparticles in porous media and to compare the relative transport of their suspensions with that of a tracer. These experiments were conducted both in the continuous flow sand-filled pressurized column and the two-dimensional continuous flow tank that were described in Chapter 4.1. The tracer used was $CaCl_2.2H_2O$. The mobility of the tracer was monitored by measuring the electrical conductivity of the column and tank effluents. 100 ml of $CaCl_2.2H_2O$ with an initial conductivity of 712 μSiemens cm^{-1} was used in the pressurized column and 500 mL of $CaCl_2.2H_2O$ with an initial conductivity of 719 μSiemens cm^{-1} was used in the continuous flow tank. The flow rate in the column was 2.4 ml/min and that in the flow-through tank was 16 mL min^{-1}. Samples were collected for 200 minutes in the column and 315 minutes in the tank. The results of column tests are given in Figure 7.10. The mobility test in the tank was also performed with the first compartment was filled with pebbles instead of sand. The curves for mobility experiments in the tank are given in Figure 7.11. The cumulative tracer mass recovered from the column and tank were calculated using the Trapezoidal Rule for the estimation of integrals (Burdens and Frank, 2003). The results are given in Figure 7.12.

$$M = \int_t QCdt = Q\sum_{i=1}^{N} \frac{C_i + C_{i+1}}{2} \Delta t_i \quad (7.1)$$

where;

Q : flowrate, L min^{-1}

Δt : time interval, min

C : concentration, mg L^{-1}

N : number of samples

The cumulative effluent mass was also calculated using the Simpson's Rule which is more accurate but requires equal time intervals between successive concentration measurements (Burden and Faires, 2003).

$$M = \int_t QCdt = Q\sum_{i=1}^{N/2} \Delta t_{2i} \frac{C_{2i-1} + 4C_{2i} + C_{2i+1}}{6} \quad (7.2)$$

Differences between the two procedures for the estimation of the integrals were minor.

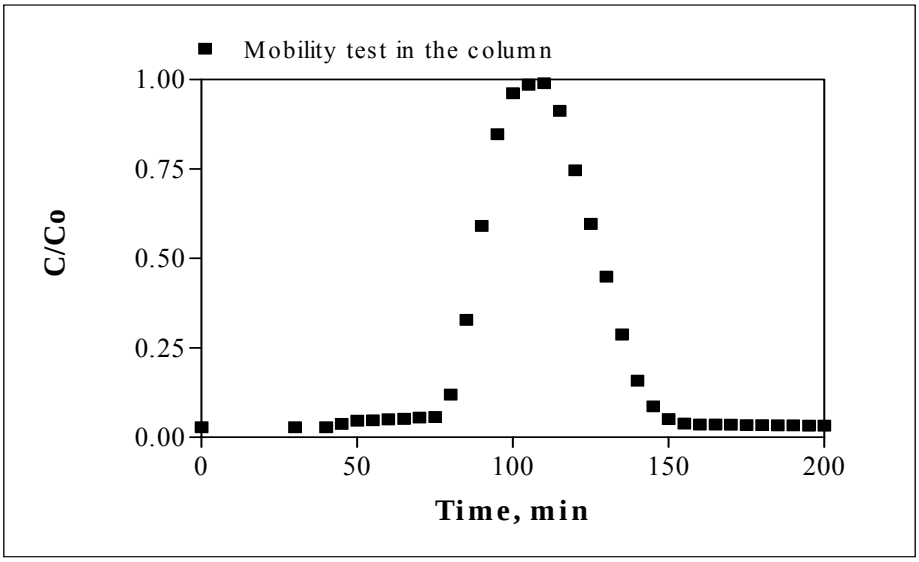

Figure 7.10. Mobility of $CaCl_2.2H_2O$ in the column; volume of tracer=100 mL, initial conductivity=712 μSiemens cm^{-1}, flowrate=2.4 mL min^{-1}.

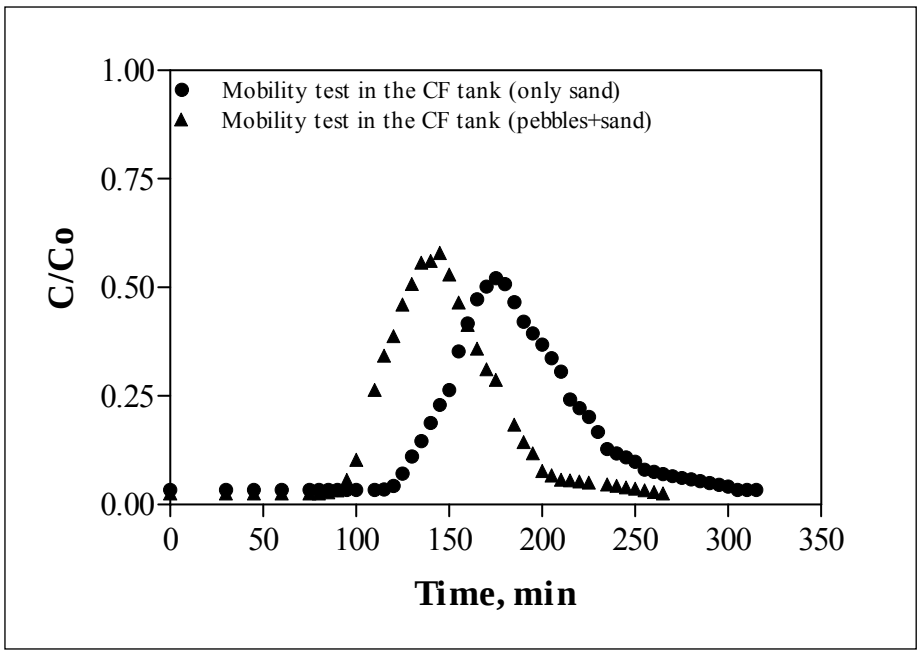

Figure 7.11. Mobility of $CaCl_2.2H_2O$ in the CF tank; volume of tracer=500 mL, initial conductivity=719 µSiemens cm^{-1}, flowrate=16 mL min^{-1}.

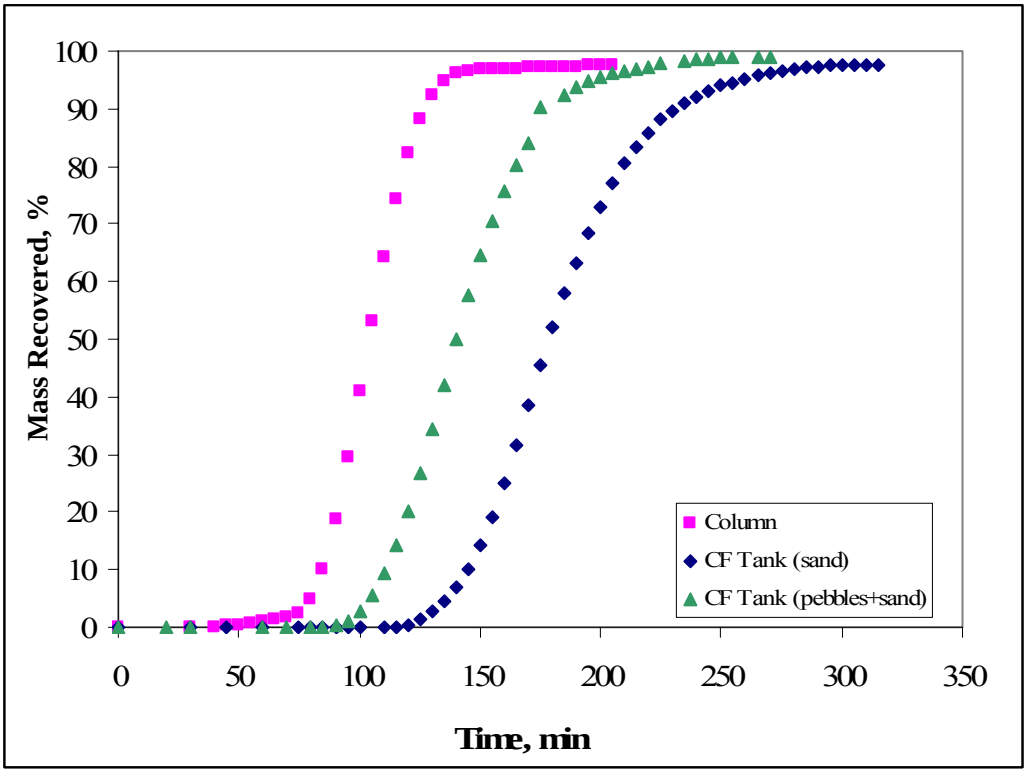

Figure 7.12. The cumulative tracer mass recovered from the column and tank as a percentage of the injected tracer mass.

As can be seen from the figures, the maximum conductivity was at t=110 min in the column, at t=175 min in the tank filled only with sand, and at t=145 min in the tank having the first compartment filled with pebbles. There was a 30 minute delay of the tracer when the first compartment was also filled with sand. The calculated effluent cumulative tracer masses were 97.45 %, 97.47 % and 99 % for the column, tank without pebble and tank with pebbles, respectively. The maximum effluent concentration observed with the column was almost equal to the influent tracer concentration. On the other hand, because of the two-dimensional nature of the flow in the tank and relatively smaller tracer suspension volume relative to the pore volume, dilution effects were higher in the tank and consequently, the maximum effluent concentration was about 50 % of the influent concentration.

7.3. Adsorption of Nanoparticles on Sand

Before performing the nanoparticle transport experiments, it is necessary to evaluate the sorption of the nanoparticles on the sand used in the tank and column. For this purpose, batch adsorption tests were conducted with MD 24 and MD 60 on the sand. Adsorption studies were performed in 50 mL flasks shaken at 100 RPM and 25°C. Memmert SV 1422 horizontal shaker was used in all adsorption experiments throughout the study. Different concentrations of MD 24 (1, 5, and 10 mg L^{-1}) and MD 60 (10, 20, 50, and 85 mg L^{-1}) were contacted with fixed masses of sand and the mixture was agitated for 1 hour. Control samples were left in the shaker for 24 h to determine the effect of time on adsorption. To represent the experimental setup of the flow through tank, 15 mL nanoparticle suspensions were added on 35 mL of sand. The sand was compacted with a downward force to obtain the same compaction ratio in the tank. The initial and final iron concentrations of the nanoparticles in the flasks were measured. The results of the adsorption tests are given in Tables 7.4 and 7.5. Overall, no significant adsorption of nanoparticles on sand was observed.

Table 7.4. Adsorption of MD 24 on sand.

MD 24 Concentration, mg L^{-1}	**t=0 (Initial Concentration), mg L^{-1}**	**t=1 h (Final Concentration), mg L^{-1}**	**t=24 h (Final Concentration), mg L^{-1}**
1.0	1.218	0.782	
5.0	4.774	4.247	4.221
10.0	10.14	8.913	

Table 7.5. Adsorption of MD 60 on sand.

MD 60 Concentration, mg L^{-1}	**t=0 (Initial Concentration), mg L^{-1}**	**t=1 h (Final Concentration), mg L^{-1}**	**t=24 h (Final Concentration), mg L^{-1}**
10.0	9.248	8.855	
20.0	20.05	18.00	
50.0	44.47	44.35	43.45
85.0	86.65	82.02	

7.4. Mobility of Nanoparticles

Mobility of nanoparticles was investigated by running mobility experiments with 100 mg L^{-1}, 300 mg $L^{-1}$and 500 mg L^{-1} MD 60 in the column and in the CF tank. Samples were collected within 5 minute time intervals for the analysis of Fe and particle size. The photographs of samples collected during 100 mg L^{-1}, 300 mg L^{-1} and 500 mg L-1 MD 60 mobility tests in the column are shown in Figures 7.13, 7.14 and 7.15. The results of the iron analysis are given in Figures 7.16 and 7.17.

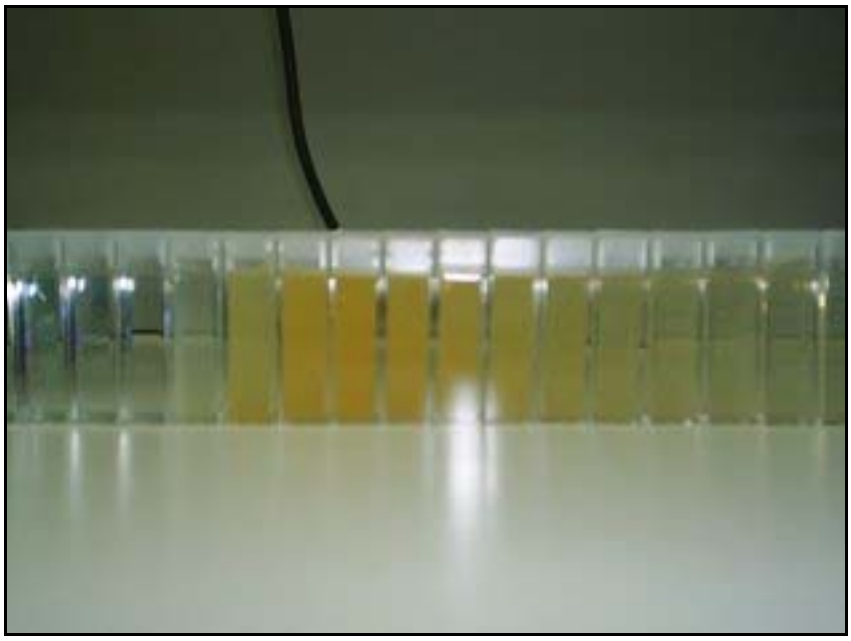

Figure 7.13. Samples taken during 100 mg L^{-1} MD 60 mobility in the column.

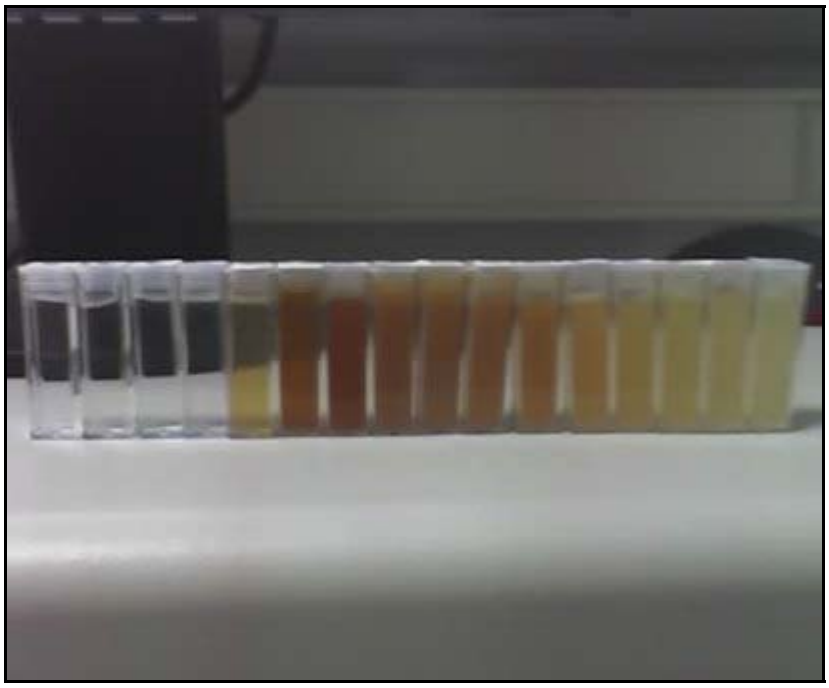

Figure 7.14. Samples taken during 300 mg L^{-1} MD 60 mobility in the column.

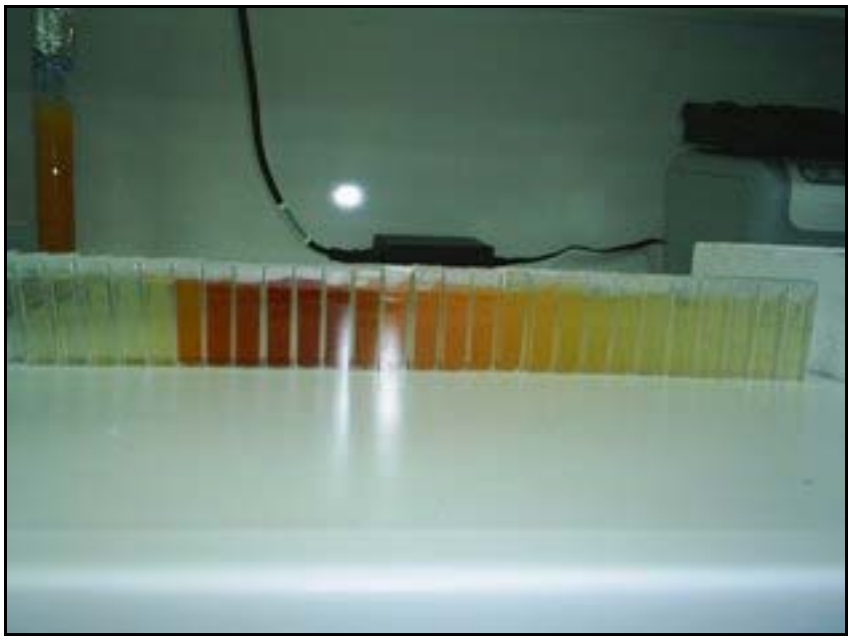

Figure 7.15. Samples taken during 500 mg L^{-1} MD 60 mobility in the column.

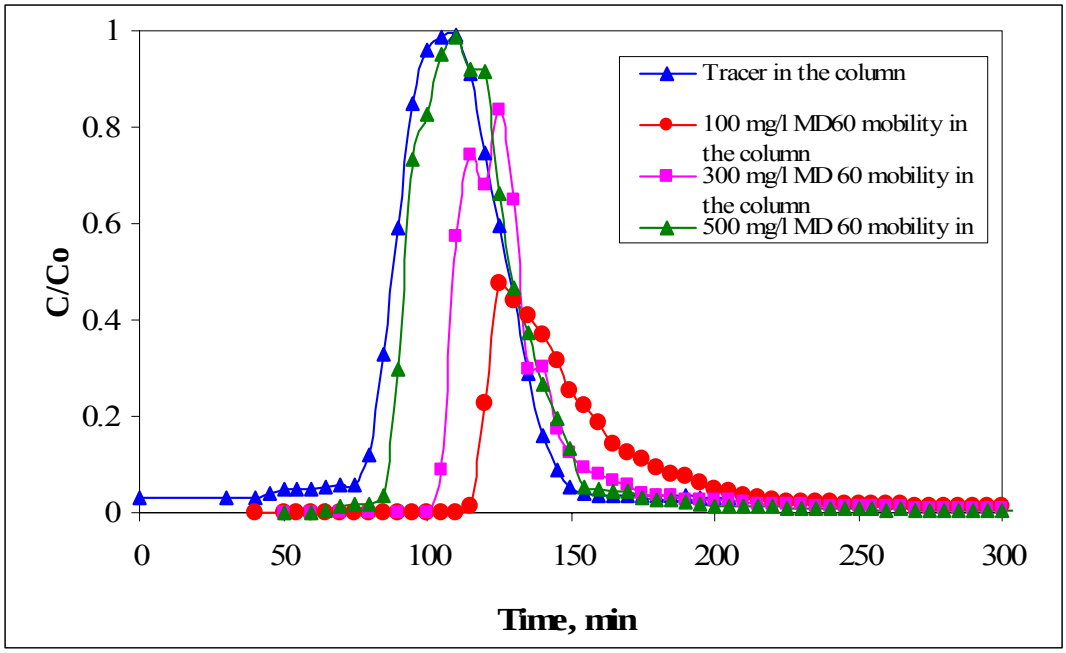

Figure 7.16. Mobility of MD 60 nanoparticles in the column.

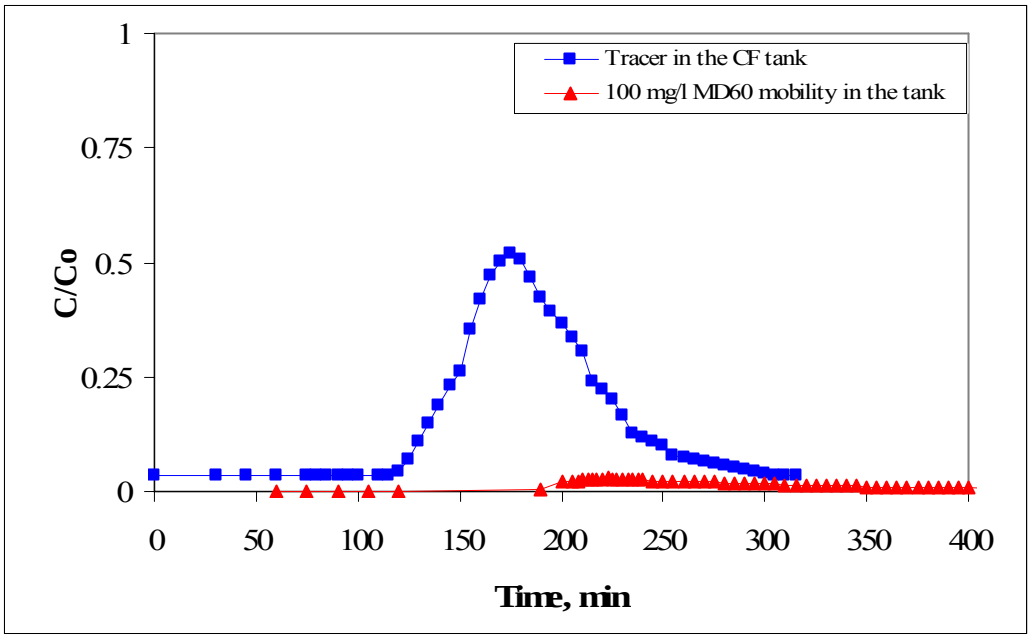

Figure 7.17. Mobility of MD 60 nanoparticles in the CF tank.

The cumulative mass of iron recovered at the exit of the column and tank as a percentage of the injected mass of iron was calculated using the Trapezoidal Rule for the estimation of integrals (Burdens and Frank, 2003). The results are given in Figure 7.18. The calculated effluent cumulative MD 60 masses were 7.99 %, 48.74 %, 59.17 % and 99.72 % for 100 mg L^{-1} in tank, 100 mg L^{-1} in column, 300 mg L-1 in column and 500 mg L^{-1} in column, respectively.

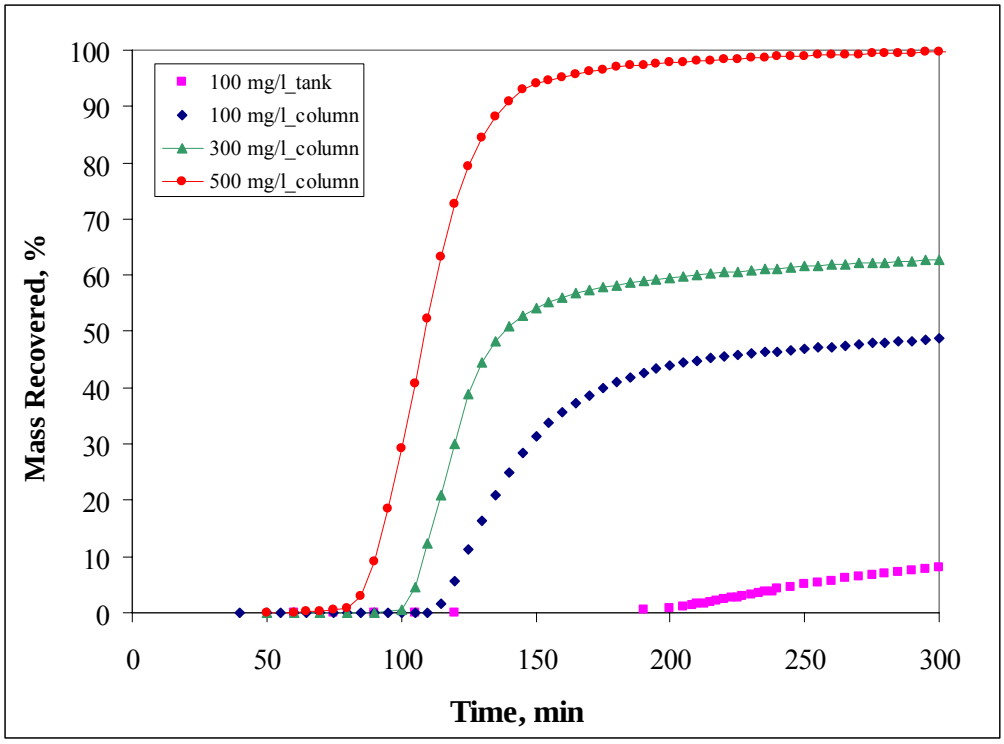

Figure 7.18. The cumulative mass of iron recovered from the column and tank as a percentage of the injected mass.

The major transport mechanisms dominant in the mobility of nanoparticles were found to be advection and dispersion. Because little sorption of nanoparticles on sand was observed in the batch tests, retardation or delay in the breakthrough curves due to sorption was negligible. Advection and Dispersion were also the dominant transport processes for the tracer. However, the transport of the nanoparticles was also influenced by the size of these particles as noted below, in contrast with the transport of dissolved species such as the tracer $CaCl_2.2H_2O$, where particle size has no impact on the transport mechanism.

It was observed that in the 100 mg L^{-1} mobility experiments, most of the nanoparticles were filtered out (92%), leading to a significant decrease in the recovery of nanoparticles both in the column and CF tank. Two possible reasons for this low transport fraction are: (i) settling of nanoparticles due to density effects since the density of the nanoparticle suspension is slightly higher than that of the resident water, or (ii) filtering out of the nanoparticles due to aggregation. The mobility experiment conducted with 500 mg

L^{-1} MD 60, showed a much high transport fraction. This indicates that density effects, which would be higher in the case of 500 mg/L nanoparticle suspension compared to 100 mg L^{-1} suspensions, are not significant. Therefore, aggregation due to dilution is the major mechanism decreasing the mobility of the MD 60 particles. The change in particle size and iron concentration of the samples collected in the 500 mg L^{-1} mobility experiment is illustrated in Figure 7.19.

An interesting feature of the transport experiments is the relatively sharp front of the rising portion (front portion) of the elution curves. This can be explained by noting that the front of dissolved plumes which moves in front of the bulk suspension is characterized by low concentration due to hydrodynamic dispersion. In the case of nanoparticle suspensions, low concentrations lead to aggregation and hence reduced mobility of the nanoparticles. Only when the concentration of the nanoparticles is sufficiently high will the nanoparticles be transported. The result is a sharper front than that observed in the tracer experiments under the same flow conditions.

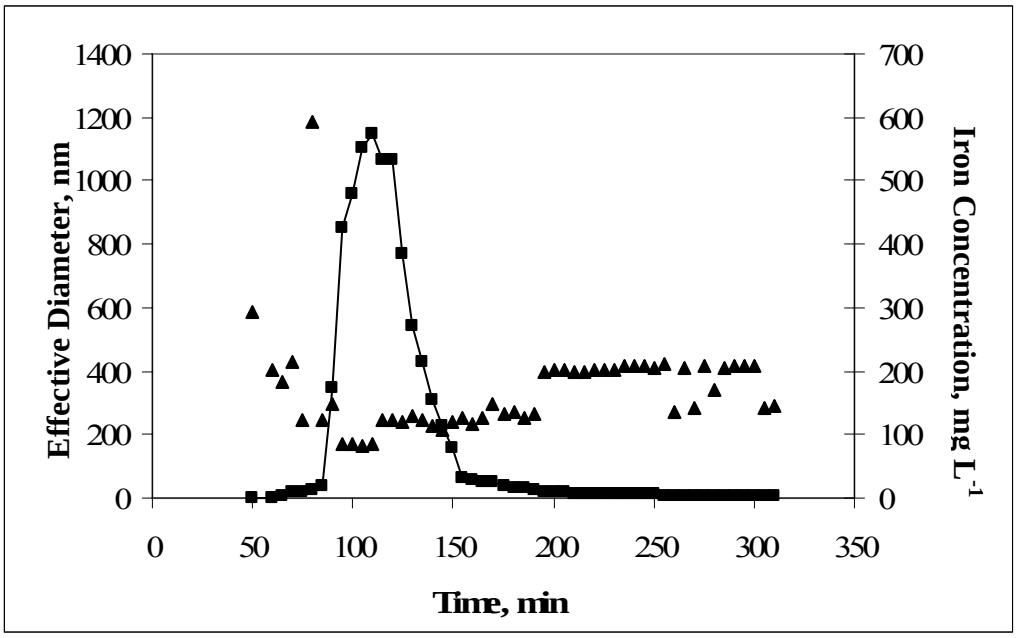

Figure 7.19. Change in particle size and iron concentration of samples collected during 500 mg L^{-1} MD 60 mobility experiment in the column.

Nanoparticle deposition due to aggregation and the maximum travel distance are also calculated by Equation 7.3, 7.4 and 7.5 (Guzman et al., 2006). The results are presented in Table 7.6.

$$\partial / \partial x \ (\mathrm{D}.\partial C / \partial x) - \mathrm{v}.\partial C / \partial x - \mathrm{k}.C = \partial C / \partial t \qquad (7.3)$$

where;

D : dispersion coefficient
v : groundwater velocity
C : concentration of the solute
x : spatial coordinate
k : deposition rate coefficient
t : time

$$k = -1 / t_p \ln \left[Q / N_o \int_0^t C(t)\,dt \right] \qquad (7.4)$$

where;

t_p : average travel time of the particles
Q : flux
N_0 : total amount of particles

$$L_{max} = -v/k \ln (C/C_0) \qquad (7.5)$$

where;

L_{max} : maximum travel distance (distance at which 99.9 % of the particles have been removed from the solution)

Table 7.6. Deposition rates and maximum travel distances.

Mobility Test	Deposition Rate (min^{-1})	Maximum Travel Distance (cm)*
100 mg L^{-1} (tank)	1.40×10^{-2}	0.002×10^{3}
100 mg L^{-1} (column)	8.60×10^{-3}	0.28×10^{3}
300 mg L^{-1} (column)	5.60×10^{-3}	0.43×10^{3}
500 mg L^{-1} (column)	2.80×10^{-5}	85.0×10^{3}

*$C/C_0 = 0.001$

In addition to the elution curves and fraction of transported mass, evolution of the particle size distribution of the transported suspension was also examined. Particle size distributions of the samples collected in the 500 mg L^{-1} mobility experiment were compared to the size distributions of the diluted MD 60 nanoparticle solution presented in Table 7.1, of Section 7.1. The results are presented in Figures 7.20 through 7.25.

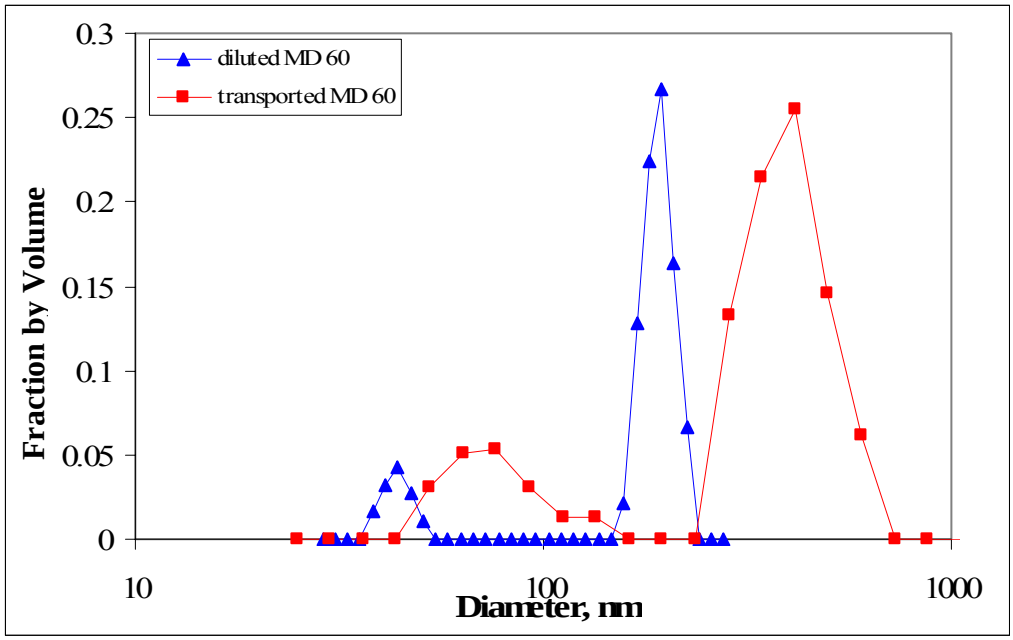

Figure 7.20. Particle size distribution of 1:10 diluted MD 60 versus an effluent sample with similar iron content.

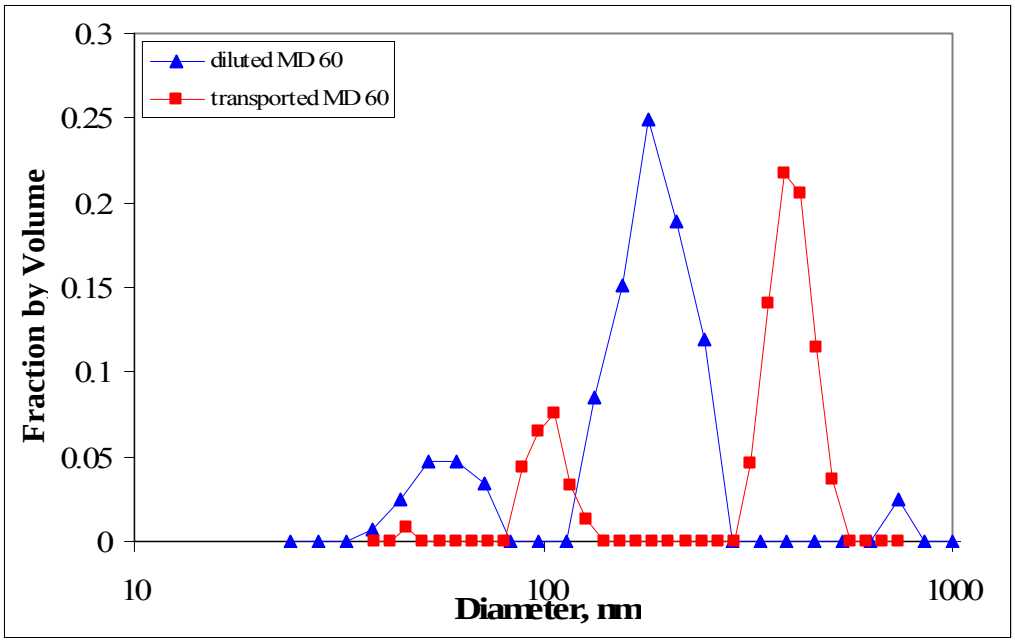

Figure 7.21. Particle size distribution of 1:20 diluted MD 60 versus an effluent sample with similar iron content.

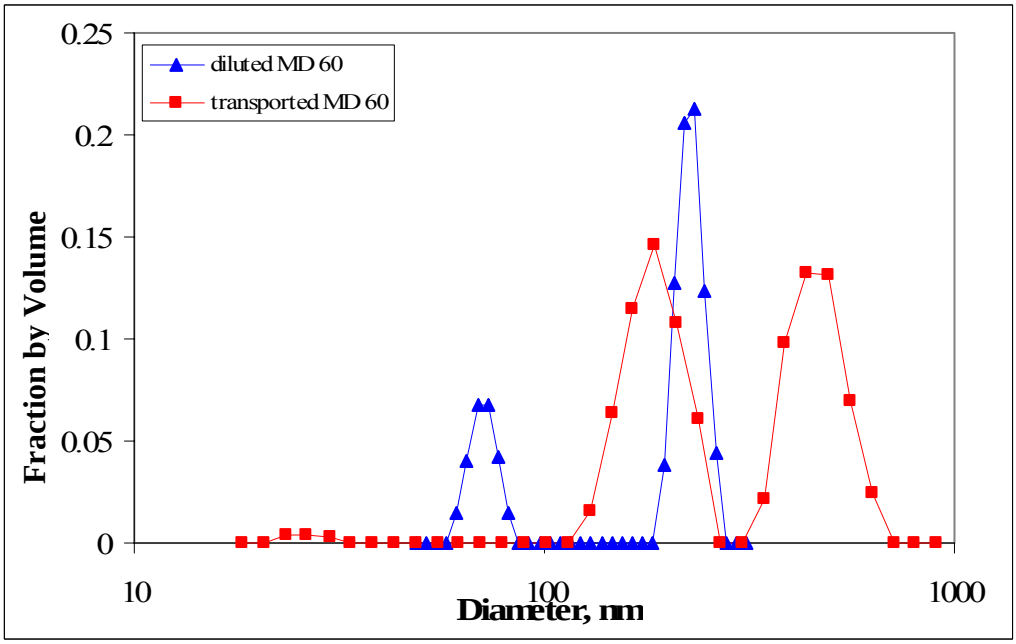

Figure 7.22. Particle size distribution of 1:100 diluted MD 60 versus an effluent sample with similar iron content.

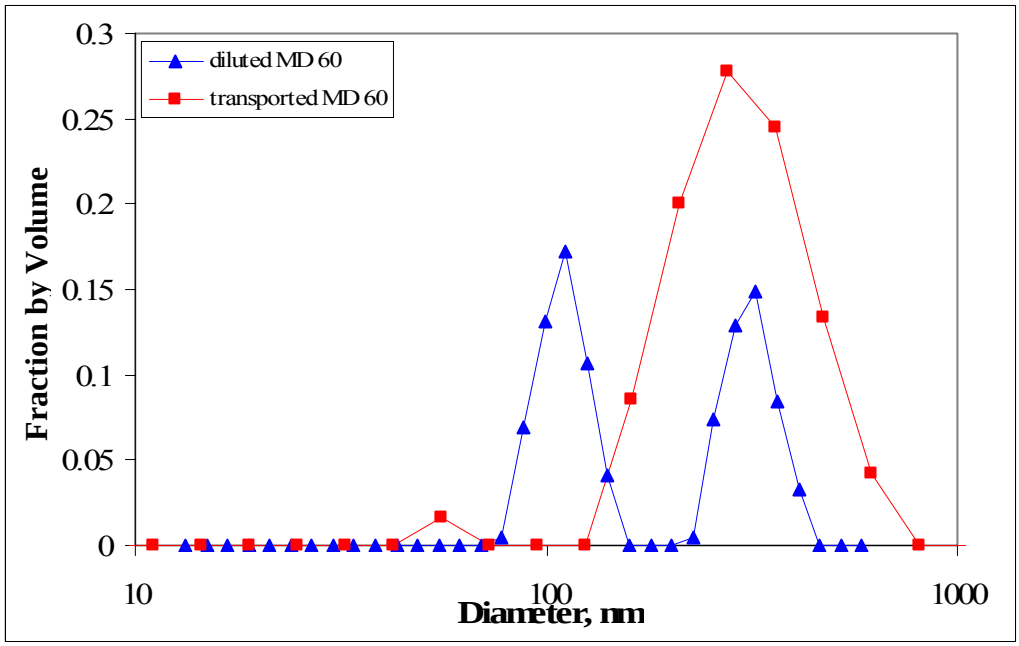

Figure 7.23. Particle size distribution of 1:200 diluted MD 60 versus an effluent sample with similar iron content.

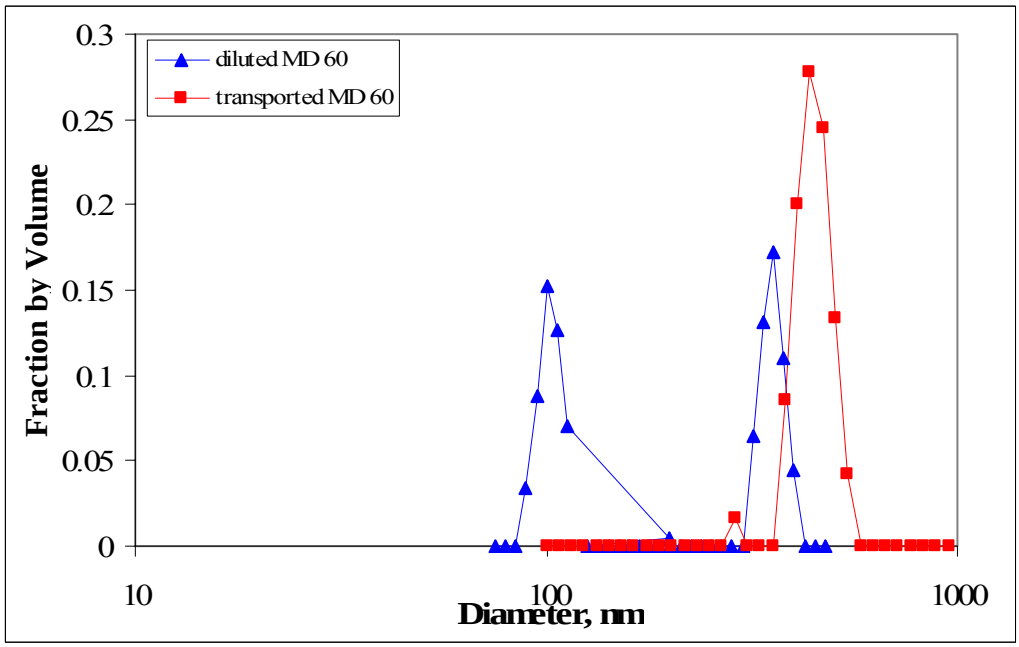

Figure 7.24. Particle size distribution of 1:500 diluted MD 60 versus an effluent sample with similar iron content.

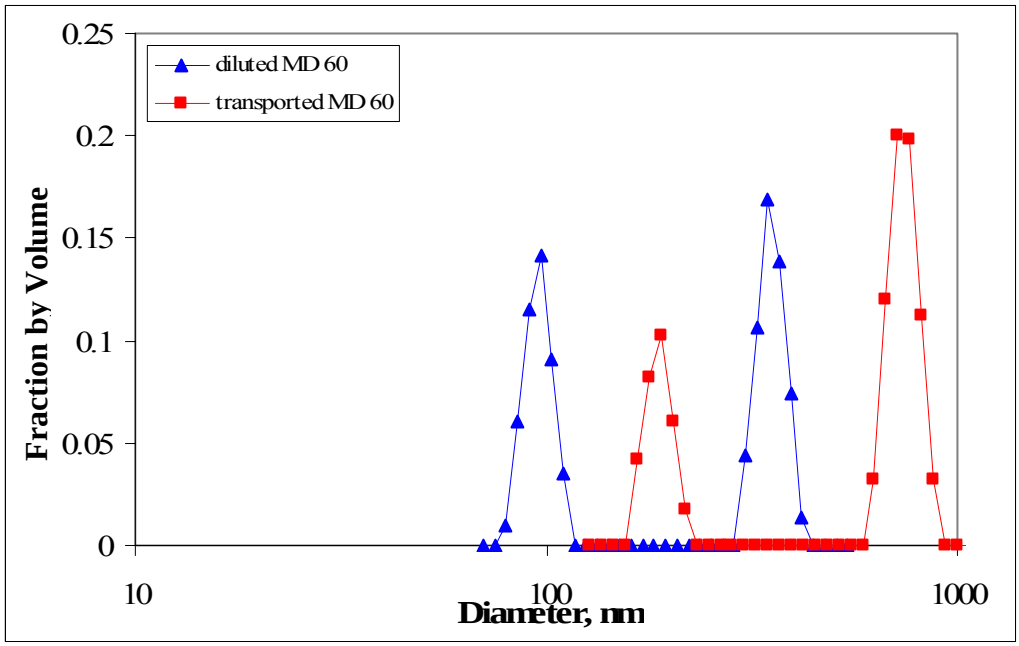

Figure 7.25. Particle size distribution of 1:1000 diluted MD 60 versus an effluent sample with similar iron content.

It was found that in both sample sets there was a tendency for an increase in particle size with dilution. However, the transported particles showed slightly higher level of aggregation possibly due to the added mixing resulting from the flow through the sand, namely the hydrodynamic dispersion.

Overall, these results demonstrate that the size distributions of nanoparticles may change as they are transported in the porous media. This can have an important effect on the mobility of these engineered particles if released into the subsurface. This is also important in applying these nanoparticles for in-situ groundwater remediation, where the reactivity of the nanoparticle (such as zero valent iron) is directly proportional to its specific surface area. The results also indicate that, provide the nanoparticle concentration in solution does not decrease substantially, the poly (acrylic acid) is a viable stabilizer for groundwater remediation applications which can limit the effects of dilution on the size of nanoparticles.

8. CONCLUSION AND RECOMMENDATIONS FOR FUTURE STUDIES

Contamination of surface and subsurface water bodies with organic compounds such as aromatic and chlorinated hydrocarbons is a widely encountered environmental problem. Because of the persistence of these compounds in the environment and the difficulty of treating water bodies contaminated with them, numerous alternative treatment technologies have been lately developed for removing them from water environment.

Advanced Oxidation Processes (AOP) and nanoparticle technologies have emerged as such alternative methods for the treatment of recalcitrant organic contaminants in water. The study presented herein is thus an evaluation of these two processes/methods for the destruction of phenol and 2-chlorophenol in water and groundwater systems. Specifically, the processes investigated were ozonation, sonolysis, sonolytic adsorption on selected nano/micro-particles and some hybrid techniques such as ozone/UV irradiation, ozone/ultrasonic irradiation, and sono-Fenton processes. All Advanced Oxidation and the related hybrid processes were tested in batch reactors to assess the impact of operational parameters on the rate of destruction of the selected test compounds, while the applicability of nanoparticles for the in-situ treatment of contaminated groundwater was assessed in completely mixed continuous flow reactors that simulated the hydraulic regime in groundwater systems. A summary of the main findings of the study is as the following:

Ozone and Ozone/UV Applications

1. The rate of degradation of the test compounds followed pseudo-first order kinetics.
2. The efficiency was much higher at alkaline conditions due to the instability or the decomposition of ozone (to more reactive and non-selective OH radicals) at this condition.
3. The rate of degradation increased with increased ozone input and decreased with increased concentration of the test compounds.

4. Degradation of 2-chlorophenol was slightly faster than that of phenol, leading to a larger fraction of 2-chlorophenol destruction in a mixture of the two compounds.
5. UV irradiation during ozonation enhanced the degree of contaminant removel upon photolytic decompositon of ozone to hydrogenperoxide followed by photolysis of hydrogenperoxide to OH radicals.

Ultrasound and Ozone/Ultrasound Processes

1. Ultrasonic reactor parameters such as frequency and ultrasonic power were important factors affecting the efficiency of sonochemical degradation of the test compounds. Although reaction rates were faster in Reactor 2 (f=300 kHz, power density=0.19 W mL^{-1} owing to longer-lived cavitation bubbles and shorter collapse durations at these condition that allowed a larger fraction of OH radicals to be ejected to the bulk solution, higher sonochemical yields were observed in Reactor 3.
2. Maximum rate of destruction was observed at highly acidic conditions (enriched hydrophobicity) that allowed a larger fraction of the compounds to move towards the gas-liquid interface, where OH radical concentration is a maximum.
3. The effect of the injected gas was such that the rate increased in the following order: Ar > Air > O_2.
4. Despite a significant fraction of compound destruction, sonolysis provided only a marginal reduction in Total Organic Carbon of the test compounds.
5. Combined sonolysis and ozonation was more effective than sonolysis alone due to enhanced mass transfer of ozone by mechanical effects of ultrasound, and the thermal decomposition of ozone to produce excess OH radicals and additional reactive species such as ozonide and peroxy radicals.

Sono-Fenton, and Sono-Nanoparticle Processes

Both processes were tested only on 2-chlorophenol. The first one was tested using various forms of iron and copper in micro suspensions or particles of $FeSO_4.7H_2O$, $CuSO_4.5H_2O$, zero valent iron, iron oxide. The sono-nanoparticle process was tested using two different nanoparticles, titanium dioxide (TiO_2) and copper oxide (CuO).
The results showed that:

1. All sono-Fenton processes were faster than sonochemical processes, but the dose of the reagent was critical such that the rate was a maximum at a threshold and slowed down above it. Addition of H_2O_2 enhanced the rate of 2-chlorophenol decay in accordance with the Fenton and Fenton-like reactions.
2. Sono-nanoparticle processes involving TiO_2 and CuO accelerated the degradation rate of 2-chlorophenol as a result of catalytic effects.

Applicability for In-situ Treatment (Flow-through Tests)

It was found that an important step in the successful application of the investigated processes for the in-situ treatment of groundwater is the ability of the nanoparticles to efficiently travel through the subsurface system. To mimic groundwater flow through porous media, two configurations of continuous flow reactors were used. The first one was a sand-filled column, where the flow was confined and one–dimensional, while the second one was a sand-filled tank with two-dimensional unconfined flow in a vertical plane. The particles tested were super paramagnetic iron oxide nanoparticles, namely MD 24, MD 59 and MD 60.

The results showed that:

1. A critical factor controlling the mobility of nanoparticles in porous media was size stabilization. In general, the tested particles showed a small increasing trend in their effective size with dilution. The limited increase in size was due to the surface coating of the particles with acrylic acid.

2. No significant adsorption of nanoparticles on sand was observed. Hence, retardation due to sorption was not a significant parameter in the mobility of the tested particles.
3. Transport of a conservative tracer monitored prior to the mobility experiments showed that practically all the injected tracer mass was recovered. Higher dilution effects were observed in the tank because of the two dimensional nature of the flow.
4. Comparison of the nanoparticle breakthrough curves to that of the tracers showed that while advection and dispersion are the two main mechanisms responsible for the tracer transport, nanoparticle transport is more complex. The transport of the nanoparticles is also influenced by their concentration which strongly controls the size of these particles, and, hence, their mobility. Specifically, at low concentrations (injected concentration 100 mg L^{-1} MD 60) the high levels of dilution mean that only a small portion of the nanoparticles get transported due to their larger effective size.
5. It was also observed that the breakthrough curves of nanoparticle solutions had a sharper front as compared to that of the tracer. This was explained by the low concentrations at the leading edge of the nanoparticle plume, which leads to larger effective size of the nanoparticles and lower mobility.

Recommendations for Future Studies

Future extension of this study may focus on the following issues:

1. Running mobility experiments with nanoparticles having different physical and chemical properties to compare property-related mobility profiles.
2. Selection (or manufacturing) of nanoparticles that are reactive in contaminant degradation and have stable size distributions.
3. Using ultrasound and reactive nanoparticles together in flow-through reactors for the optimization of system parameters,
4. Development of a model representing the fate and transport of groundwater contaminants and nanoparticles in the subsurface to assess the feasibility of these systems in real-life applications.

REFERENCES

Abe, K. I., Tanaka, K., 1996. Degradation of phenol, asulam and lignin in aqueous solution by ozonation. Toxicological and Environmental Chemistry, 54, 187-193.

Akata, A., Gurol, M. D., 1992. Oxidation of Nitrobenzene by Ozone and Ozone/UV Processes, Proceedings of the International Symposium on Chemical Oxidation Technology for the Nineties, Nashville, 1992.

Alegria, E., Lion, Y., Kondo, T., Riesz, P., 1989. Sonolysis of aqueous surfactant solutions-probing the interfacial region of cavitation bubbles by spin trapping. Journal of Physical Chemistry, 93, 4908-4913.

Argonne National Laboratory
http://www.anl.gov/

Augugliaro, V., Rizzuti, L., 1978. The pH dependence of the ozone absorption kinetics in aqueous phenol solutions. Chemical Engineering Science, 33 (11), 1441-1447.

Barbier, P. F., Petrier, C., 1996. Study at 20 kHz and 500 kHz of the ultrasound-ozone advanced oxidation system: 4-nitrophenol degradation. Journal of Advanced Oxidation Technologies, 1, 154-159.

Beckett, M. A., Hua, I., 2001. Impact of ultrasonic frequency on aqueous sonoluminescence and sonochemistry. Journal of Physical Chemistry A, 105(15), 3796-3802.

Benitez, F. J., Beltran-Heredia, J., Acero, J. L., Rubio, F. J., 2000. Rate constants for the reactions of ozone with chlorophenols in aqueous solutions. Journal of Hazardous Materials, 79, 271-285.

Bremner, D. H., Burgess, A. E., Houllemare, D., Namkung, K., 2006. Phenol degradation using hydroxyl radicals generated from zero-valent iron hydrogen peroxide. Applied Catalysis B: Environmental, 63, 15-19.

Bremner, M. P., Hilgenfeldt, S., Lohse, D., 2001. Single bubble sonoluminscence, Reviews of Modern Physics.

Brookhaven National Laboratory
http://www.brookhaven.co.uk/

Burden, R., Faires, J. D., 1997. Numerical Analysis, Brooks/Coles Publishing.

Carey, H. J., 1992. An introduction to AOP for destruction of organics in wastewater. Water Quality Research Journal of Canada, 27, 1-21.

Chiou, C., T., Peters, L. J., Freed, V. H., 1979. A physical concept of soil-water equilibria for nonionic organic compounds. Science, 206, 831-832.

Chung, T., Liao, C., Chen, W., Kuo, S., 2006. Treatment of pentachlorophenol-contaminated soil using nano-scale zero-valent iron with hydrogen peroxide. Journal of Molecular Catalysis A: Chemical, 265, 189-194.

Colarusso, P., Serpone, N., 1996. Sonochemistry effects of ultrasound on homogeneous chemical reactions and in environmental detoxification. Research on Chemical Intermediates, 22(1), 61-89.

Cooper, W. J., Curry, R. D., O'Shea, K. E., 1998. Environmental Applications of Ionizing Radiation, John Wiley and Sons, Inc., U.S.A.

Criddle, C. S., deWitt, J. T., Grbi-Gali, D., McCarty, P. L., 1990. Transformation of carbon tetrachloride by *Pseudomonas sp strain ILC* under denitrification conditions. Applied and Environmental Micobiology, 56, 3240-3246.

Czaplicka, M., 2006. Photo-degradation of chlorophenols in the aqueous solution. Journal of Hazardous Materials, B134, 45–59.

Dahlem, O., Demaiffe, V., Halloin, V., Reisse, J., 1998. Direct sonication system suitable for medium-scale sonochemical reactors. AICHE Journal, 44, 2724-2730.

Demirer, M., 2006. Controlled synthesis of superparamagnetic iron oxide nanoparticles in the presence of poly(acrylic acid), M.S. Thesis, Koç University.

Dendritic Nanotechnologies, Inc.
http://dnanotech.com/index.php

Drijvers, D., Van Langenhove, H., Beckers, M., 1999. Decomposition of phenol and trichloroethylene by the ultrasound/H_2O_2/CuO process. Water Research, 33(5), 1187-1194.

Elliott D., Zhang,W., 2001. Field assessment of nanoparticles for groundwater treatment. Environmental Science and Technology, 35, 4922–4926.

European Society of Sonochemistry
http://www.europeansocietysonochemistry.eu/

Fenton, H.J.H., 1894. Oxidation of tartaric acid in presence of iron. Journal of Chemical Society, 65, 899.

Fischer, C. H., Hart, E. J., Henglein, A., 1986. Ultrasonic irradiation of water in the presence of oxygen 18, $^{18}O_2$: isotope exchange and isotopic distribution of hydrogen peroxide. Journal of Physical Chemistry, 90, 1954-1956.

Fortner, J. D., Lyon, D. Y., Sayes, C. M., Boyd, A. M., Falkner, J. C., Hotze, E. M., Alemany, L. B., Tao, Y. J., Guo, W., Ausman, K. D., Colvin, V. L., Hughes, J. B., 2005. C60 in water: nanocrystal formation and microbial response. Environmental Science and Technology, 39, 4307-4316.

Freeze, R. A., Cherry, J. A., 1979. Groundwater. Prentice-Hall, Inc., Englewood Cliffs, NJ.

Gaitan, D. F., Crum, L.A., Church, C. C., Roy, R. A., 1992. Sonoluminescence and bubble dynamics for a single, stable, cavitation bubble. Journal of the Acoustical Society of America, 91, 3166-3183.

Gaw Lin, J., Shih Ma, Y., 2000. Oxidation of 2-chlorophenol in water by ultrasound/fenton method. Journal Of Environmental Engineering, 130-137.

Gillham, R. W., Cherry, J. A., 1982. Contaminant migration in saturated unconsolidated geologic deposits. Geological Society of America, 189, 31-62.

Glaze W. H., Kang, J. W., Chapin, D. H., 1987. The chemistry of water treatment processes involving ozone, hydrogen peroxide, and ultraviolet radiation. Ozone Science and Engineering, 9, 335-352.

Glaze, W. H., Guittoneau, S., Duguet, J. P., Wable, O., 1991. Characterization of natural waters for potential to oxidize organic pollutants with ozone in Proceedings of the 10th ozone world congress, Switzerland.

Gong, C., Hart, D. P., 1998. Ultrasound induced cavitation and sonochemical yields. Journal of Acoustical Society of America, 104, 2675-2682.

Gonzalez, E., Mansilla, H. D., Casa, S., Freer, J., Rodriguez, J., Baeza, J., 1995. The decomposition of chlorophenols by ozone/UV, in Proceedings of the 12th ozone world congress, France, 743-746.

Gottschalk, C., Libra, J. A., Saupe, A., 2000. Ozonation of Water and Waste Water, Wiley-VCH.

Guzman, D. K., Finnegan, M. P., Banfield, J. F., 2006. Influence of surface potential on aggregation and transport of titania nanoparticles. Environmental Science and Technology, 40, 7688-7693.

Haertel, G., Ghaly, M. Y., Mayer, R., Haseneder, R., 2001. Photochemical oxidation of p-chlorophenol by UV/H_2O_2 and photo-Fenton process: a comparative study. Waste Management, 21, 41-47.

Helz, G. R., Zepp, R. G., 1994. Aquatic and Surface Photochemistry. Bolton, J. R., Cater, S. R., Homogenous Photodegradation of Pollutants in Contaminated Water: An Introduction, 467-490, CRC Press, Inc., U.S.A.

Helz, G. R., Zepp, R. G., 1994. Aquatic and Surface Photochemistry. Yao, C. D., Mill, T., Reaction Pathways in Advanced Oxidation Processes, 499-515, CRC Press, Inc., U.S.A.

Henglein, A., 1987. Sonochemistry: historical developments and modern aspects. Ultrasonics, 25(1), 6-16.

Hepure Technologies
http://www.hepure.com/

Hoigne, J., Bader, H., 1983. Rate constants of reactions of ozone with organic and inorganic compounds in water. Water Research, 17, 185-194.

Holister P., Weener, J. W., Vas, C. R., Harper, T., 2003. Nanoparticles-Technology White Papers, No:3, 2-11.

Hua, I., Hoffmann, M.R., 1996. Kinetics and mechanisms of the sonolytic degradation of CCl_4: intermediates and byproducts. Environmental Science and Technology, 30, 864-861.

Hua I., Hoffmann M. R., 1997. Optimization of ultrasonic irradiation as an advanced oxidation technology. Environmental Science and Technology, 31, 2237-2243.

In, R. J., Ku, Y., 1995. Ozonation of 2-chlorophenol in aqueous solution in: Proceedings of the 12th ozone world congress, 1, France, International Ozone Association, 737-740.

Ince, N. H., Gonenc, D. T., 1997. Treatability of textile azo dye by UV/H_2O_2, Environmental Technology, 18, 179-185.

Ince, N. H., Tezcanli, G., 2001. Reactive dyestuff degradation by combined sonolysis and ozonation. Dyes and Pigments, 49, 145-153.

Ince, N. H., Tezcanli, G., Belen, R K., Apikyan, I. G., 2001. Ultrasound as a catalyzer of aqueous reaction systems: the state of the art and environmental applications. Applied Catalysis B: Environmental, 29, 167-176.

Ince N. H., Kidak, R., 2006. Ultrasonic destruction of phenol and substituted phenols: A review of current research. Ultrasonics Sonochemistry, 13, 195-199.

Ince, N. H., Kidak, R., 2006. Effects of operating parameters on sonochemical decomposition of phenol. Journal of Hazardous Materials, B137, 1453-1457.

Jardim, W. F., Moraes, S. G., Takiyama, M. M. K., 1997. Photocatalytic degradation of aromatic chlorinated compounds using TiO_2: toxicity of intermediates. Water Research, 31(7), 1728-1732.

Jiang, J. Q., Yin, Q., Zhou, J. l., Pearce, P., 2005. Occurrence and treatment trials of endocrine disrupting chemicals in wastewaters. Chemosphere, 61, 544-550.

Klabunde, K. J., Lagadic, I., Dieken, L., Boronina, T. N., 1998. Zinc-silver, zinc-palladium, and zinc-gold as bimetallic systems for carbontetrachloride dechlorination in water. Journal of Hazardous Substance Research, 1, 6.1-6.15.

Kim, S. M., Geissen, S. U., Vogelpohl, A., 1997. Landfill leachate treatment by a photoassisted fenton reaction. Water Science and Technology, 35, 239-248.

Kim, J. K., Metcalfe, I. S., 2007. Investigation of the generation of hydroxyl radicals and their oxidative role in the presence of heterogeneous copper catalysts. Chemosphere, Article in Press.

Klassen, N. V., Marchington, D., McGowan, H. C. E., 1994. H_2O_2 Deteremination by the I_3^- Method and by the KMnO4 Titration, Anal. Chem. 66, 2921-2925.

Kontronarou, A., Mills, G., Hoffmann, M. R., 1991. Ultrasonic irradiation of p-nitrophenol in aqueous solution. Journal of Physical Chemistry, 95, 3630-3638.
Ku, Y., Chen, K. y., Lee, K. K., 1997. Ultrasonic destruction of 2-chlorophenol in aqueous solution. Water Research, 31, 929-935.

Lawrence Berkeley National Laboratory
http://www.lbl.gov/

Lecoanet, H. F., Wiesner, M. R., 2004. Velocity effects on fullerene and oxide nanoparticle deposition in porous media. Environmental Science and Technology, 38, 4377-4382.

Liao, L., Wang, Y., Huang, B., Wang, S., 2006. Comparison of enhancement of pentachlorophenol sonolysis at 20 kHz by dual-frequency sonication. Ultrasonics Sonochemistry, 13, 506–510.

Loung Chen, C., Wang, R., Gratzl, J. S., 2005. Dechlorination of chlorophenols found in pulp bleach plant E-1 effluents by advanced oxidation processes. Bioresource Technology, 96, 897–906.

Ma, C., Tu, Y., Ku, Y., 2005. Effect of hydrogen peroxide on the decomposition of monochlorophenols by sonolysis in aqueous solution. Water Research, 39, 1093–1098.

Makkino, K., Mossoba, M., Riesz, P., 1982. Chemical effects of ultrasound on aqueous solutions. Journal of American Chemical Society,104 (12), 3537-3539.

Mallouk, T. E., Schrick B., Blough, J., Jones, A., 2002. Hydrodechlorination of trichloroethylene to hydrocarbons using bimetallic nickel-iron nanoparticles. Chem. Mater.14(12), 5140–5147.

Mallouk, T. E., Hydutsky, B. W., Mack, E. J., Beckerman, B. B., Skluzacek, J. M., 2007. Optimization of nano- and microiron transport through sand columns using polyelectrolyte mixtures. Environmental Science and Technology, 41, 6418-6424.

Mark, G., Tauber, A., Laupert, R., Schechmann, H. P., Schulz, D., Mues, A., Von Sonntag, C. 1998. OH-radical formation by ultrasound in aqueous solution - part II: terephthalate and fricke dosimetry and the influence of various conditions on the sonolytic yield. Ultrasonics Sonochemistry, 5, 41-52.

Mason, T. J., Lorimer, J. P., Walton, D. J., 1990. Sonoelectrochemisry. Ultrasonics, 28, 333-337.

Mason, T. J., Lorimer, J. P., Bates, D. M., Zhao, Y., 1994. Dosimetry in sonochemistry: the use of aqueous terephthalate ion as a fluorescence monitor. Ultrasonics Sonochemistry, 1(2), 91-95.

Mason, T. J., Cordemans, E.D., 1998. Practical consideration for process optimization, J. L. Luche (Ed), Synthetic Organic Sonochemistry, 301-331, Plenum Press

Mason, T.J., 1999. Sonochemistry, Oxford University Press Inc., New York.

Matthews, R. W., 1986. Photo-oxidation of organic material in aqueous suspensions of titaniumdioxide. Water Research, 20, 569–578.

McKeown, J., Cl, Lawrence, C. B., Singh, A., 1998. Environmental Applications of Ionizing Radiation: Engineering Studies for Soil Detoxification and Sludge Disinfection with the Impela Accelerator, John Wiley and Sons, Inc., U.S.A., 537-555.

Moore, M. N., 2006. Do nanoparticles present ecotoxicological risks for the health of the aquatic environment. Environment Int. 32(8), 967-976.

Munter, R., 2001. Advanced oxidation processes-current status and prospects. Proceedings of the Estonian Academy of Sciences Chemistry, 50, 59-80.

Nagata, Y., Nakagawa, M., Okuno, H., Mizukoshi, Y., Yim, B., Maeda, Y., 2000. Sonochemical degradation of chlorophenols in water. Ultrasonics Sonochemistry, 7, 115-120.

Nanolab, Inc.
http://www.nano-lab.com/

Neppiras, E. A., 1980. Acoustic Cavitation Thresholds and Cyclic Processes, Ultrasonics, 18, 201-209.

Noltingk, B. E., Neppiras, E. A., 1950. Cavitation Induced by Ultrasonics, Proc. Phys. Soc. B63, 674-678.

Nurmi, J. T., Tratnyek, P. G., Sarathy, V., Baer, D. R., Amonette, J. E., Pecher, K., Wang, C., Linehan, J. C., Matson, D. W., Penn, R. L., Driessen, M. D., 2005. Characterization and properties of metallic iron nanoparticles: spectroscopy, electrochemistry, and kinetics. Environmental Science and Technology, 39 (5), 1221-1230.

Oberdörster, G., Oberdörster, E., Oberdörster, J., 2005. Nanotoxicology: an emerging discipline evolving from studies of ultrafine particles. Environmental Health Perspective, 113 (7), 823-839.

O'Hannesin, S. F., 1993. A field demonstration of a permeable well for the in-situ abiotic degradation of halogenated aliphatic organic compounds. M. S. Thesis, University of Waterloo.

Olson, T. M., Barbier, P. F., 1994. Oxidation kinetics of natural organic matter by sonolysis and ozonation. Water Research, 28, 1383-1391.

Pelizetti, E., Barbeni, M., Minero, C., 1987. Chemical degradation of chlorophenols with fenton's reagent. Chemosphere, 16, 2225-2237.

Pera-Titus, M., Molina, V., Banos, M. A., Gimenez, J., Esplugas, S., 2004. Degradation of chlorophenols by means of advanced oxidation processes : a general review. Applied Catalysis B: Environmental, 47, 219-256.

Petrier, C., Lamy, M. F., Francony, A., Benahcene, A., David, B., 1994. Sonochemical degradation of phenol in dilute aqueous solutions: comparison of the reaction rates at 20 and 487 kHz. Journal of. Physical Chemistry, 98, 10514-10520.

Petrier, C., Francony, A., 1997. Ultrasonic Waste-Water Treatment: Incidence of Ultrasonic Frequency on the Rate of Phenol and Carbon Tetrachloride Degradation" Ultrason. Sonochem.. 4, 295-300.

Pontius, F. W., 1990. Water Quality and Treatment, Mc-Graw-Hill Inc., USA, 781-785.

Riesz, P., Mason T. J., 1991. Advances in Sonochemistry, JAI Press, London, 23.

Ruppert, G., Bauer, R., 1993. The photo-fenton reaction-an effective photochemical wastewater treatment process. Journal of Photochemistry and Photobiology A: Chemistry, 73, 75-78.

Schwarzenbach, R. P., Gschwend, P. M., Imboden, D. M., 1993. Environmental Organic Chemistry, John Wiley and Sons, Inc., U.S.A., 681.

Shirgaonkar, I. Z., Pandit, A. B., 1998. Sonophotochemical destruction of aqueous solution of 2,4,6-trichlorophenol. Ultrasonics Sonochemistry, 5, 53-61.

Semprini, L., Hopkins, G. D., McCarty, P. L., Roberts, P. V., 1992. In-situ transformation of carbon tetrachloride and other halogenated compounds resulting from biostimulation under anoxic conditions. Environmental Science and Technology, 26 (12), 2454-2461.

Solarchem Environmental Systems, 1994. The UV/Oxidation Handbook, Ontario Canada,.

Song-Hu, Y., Xiao-Hua, L., 2005. Comparison treatment of various chlorophenols by electro-fenton method: relationship between chlorine content and degradation. Journal of Hazardous Materials, 118(1-3), 85-92.

Staehelin, J., Hoigné, J., 1982. Decomposition of ozone in water: rate of initiation by hydroxide ions and hydrogen peroxide. Environmental Science and Technology, 16, 676-681.

Storey, B. D., Szeri A. J., 2002. Inertially driven pressure inhomogeneities in violently collapsing bubbles: the validity of the Rayleigh-Plesset equation. Journal of Fluid Mechanics, 452, 145-162.

Sung, M., Huang, C. P., 2007. Kinetics of the degradation of 2-chlorophenol by ozonation at pH 3. Journal of Hazardous Materials, 141, 140–147.

Suressh, S., Patel, U. D., 2007. Dechlorination of chlorophenols using magnesium-palladium bimetallic system. Journal of Hazardous Materials, 147, 431-438.

Suslick, K. S., 1990. Sonochemistry, Science, 247, 1439-1445.

Suslick, K. S., 1994. The Chemistry of Ultrasound, http://www.scs.uiuc.edu//~suslick/britannica.html

Suslick, K.S., Didenko, Y., Fang, M.F., Hyeon, T., Kolbeck, K.J., McNamara, W.B., Mdleleni, M.M., Wong, M. 1999. Acoustic cavitation and its chemical consequences. Philosophical Transactions of the Royal Society A, 357, 335-353.

Tarr, M. A., Maurin, M., Zheng, W., 2005. Enhancement of sonochemical degradation of phenol using hydrogen atom scavengers. Ultrasonics Sonochemistry, 12, 313–317.

Tatara, G. M., Dybos, M. J., Criddle, C. S., 1993. Effects of medium and trace metals on the kinetics of carbon tetra chloride transformation by pseudomonas sp strain ILC, Applied and Environmental Microbiology, 59 (7), 2126-2131.

Tezcanlı, G., 1998. Reuse of Textile Dyebaths by Treatment with Advanced Oxidation, M.S. Thesis, Boğaziçi University.

The National Nanotechnology Initiative
http://www.nano.gov/

Trapido, M., Hivroren, A., Veressinina, Y., Hentunen, J., Munter, R., 1997. Ozonation, ozone/UV and UV/H_2O_2 degradation of chlorophenols. Ozone: Science and Engineering, 19, 75-96.

U.S. Environmental Protection Agency (EPA), 1998. Advanced Photochemical Oxidation Processes, U.S.A.

U.S. Environmental Protection Agency (EPA), 2001. Handbook on NonPhotochemical Oxidation Processes, Tetra Tech EM, Inc., U.S.A.

U.S. Environmental Protection Agency, 2005a. Semivolatile Organic Compounds By Gas Chromatography / Mass Spectrometry (GC/MS) Method 8270D.
www.epa.gov/SW-846/pdfs/8270d.pdf.

U.S. Environmental Protection Agency, 2005b. Appendix A To Part 136 Methods For Organic Chemical Analysis Of Municipal And Industrial Wastewater Method 604 - Phenols, www.epa.gov/waterscience/methods/guide/604.pdf.

U.S. Environmental Protection Agency, 2007. Nanotechnology White Paper.

Walling, C., 1975. Fenton's reagent revisited, Accounts of Chemical Research, 8, 125-131.

Wang C., Zhang, W. "Nanoscale metal particles for dechlorination of PCE and PCBs", Environ. Sci. Technol.31(7), 2154–2156, 1997.

Weathers, L.J., and G.F. Parkin, “Metallic Iron-Enhanced Biotransformation of CarbonTetrachloride and Chloroform Under Methanogenic Conditions,” pp. 117-122 in Bioremediation of Chlorinated Solvents, R.E. Hinchee et al., (Eds.) Battelle Press, Columbus, OH 1995.

Weavers, L. K., Ling, F. H., Hoffmann, M. R., 1998. Aromatic compound degradation in water using a combination of sonolysis and ozonolysis. Environmental Science and Technology, 32, 2727-2733.

Wiesner, M. R., Lecoanet, H. F., Bottero, J., 2004. Laboratory assessment of the mobility of nanomaterials in porous media. Environmental Science and Technology, 38, 5164-5169.

Wiesner, M. R., Lowry, G. V., Alvarez, P., Dionysiou, D., Bisawas, P., 2006. Assessing the risks of manufactured nanomaterials. Environmental Science and Technology, 40 (14), 4336-4345.

Wong, M. S., Nutt, M. O., Heck, K. N., Alvarez, P., 2006. Improved Pd-on-Au bimetallic nanoparticle catalysts for aqueous trichloroethene hydrodechlorination. Applied Catalysis B: Environmental, 69, 115-125.

Wu, J. R., Chang, C. N., Lin, J. G., 1996. Decomposition of 2-chlorophenol in aqueous solution by ultrasound/H_2O_2 process. Water Science and Technology, 33, 75-81.

Wu, C., Liu, X., Wei, D., Fan, J., Wang, L., 2001. Photosonochemical degradation of phenol in water. Water Research, 35, 3927–3933.

Zhang, W., Elliott, D. W., 2001. Field assessment of nanoscale bimetallic particles for groundwater treatment. Environmental Science and Technology, 35, 4922-4926.

Zhang, W., Lien, H., 2001. Nanoscale iron particles for complete reduction of chlorinated ethenes. Colloids and Surfaces A: Physicochemical and Engineering Aspects, 191, 97-105.

Zhang, W., 2003. Nanoscale iron particles for environmental remediation: an overview. Journal of Nanoparticle Research, 5, 323-332.

Zhang, W., Masciangioli T., 2003. Environmental nanotechnology: potential and pitfalls. Environmental Science and Technology, 37, 102A–108A.

Zhang, W., Quan, X., Zhang, Z., 2007. Catalytic reductive dechlorination of *p*-chlorophenol in water using Ni/Fe nanoscale particles. Journal of Environmental Sciences, 19, 362-366.

Zhao, D., He, F., 2004. In-situ destruction of PCBs, PCE, and TCE in Alabama soils and groundwater using a new nanoscale sorptive catalyst unclassified. Report for 2003 ALB8B.

APPENDIX A

CHEMICAL ANALYSIS OF SAND USED IN CONTINUOUS FLOW EXPERIMENTS

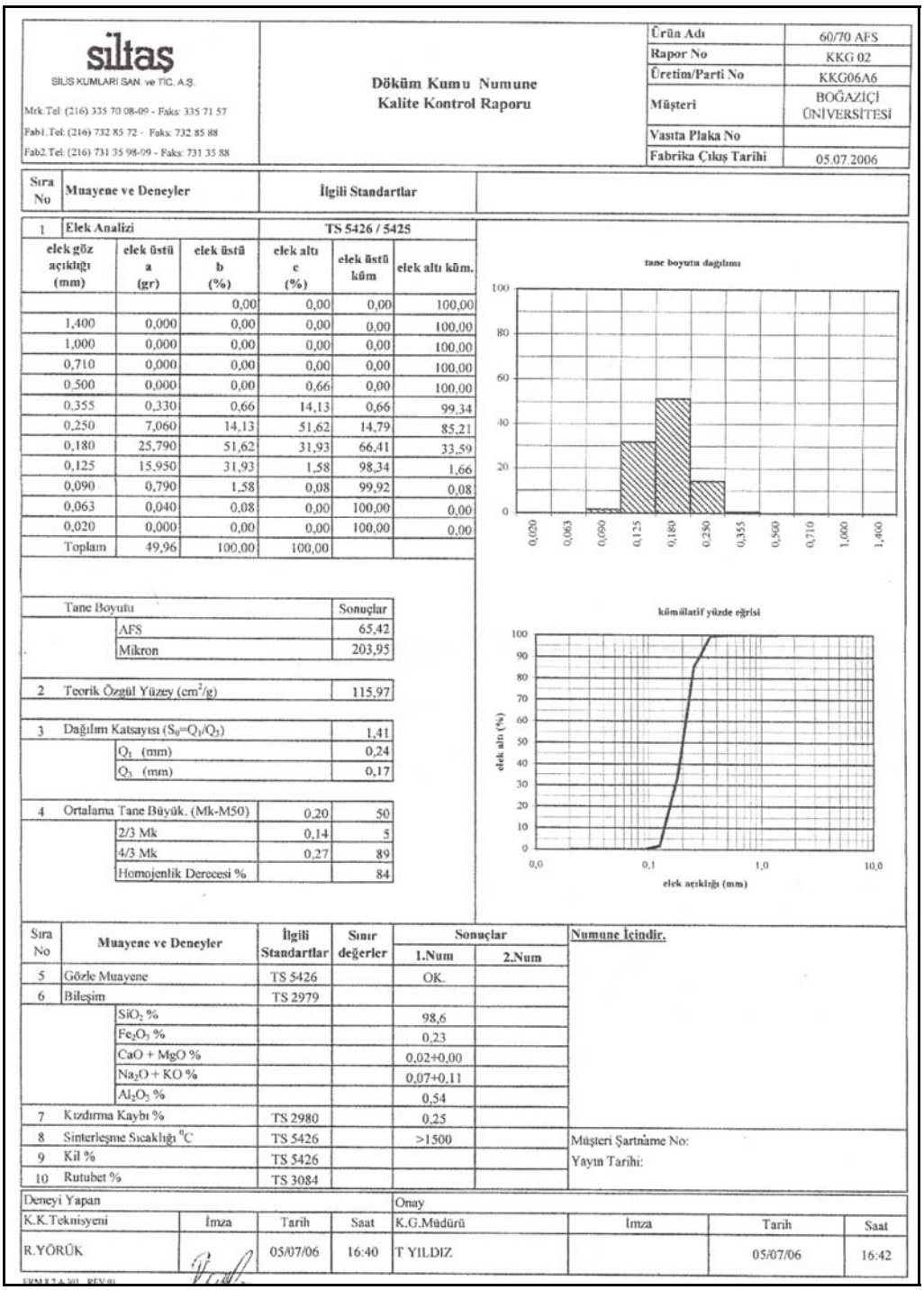

siltaş
SİLİS KUMLARI SAN. ve TİC. A.Ş.
Mrk.Tel: (216) 335 70 08-09 - Faks: 335 71 57
Fab1.Tel: (216) 732 85 72 - Faks: 732 85 88
Fab2.Tel: (216) 731 35 98-09 - Faks: 731 35 88

Döküm Kumu Numune Kalite Kontrol Raporu

Ürün Adı	60/70 AFS
Rapor No	KKG 02
Üretim/Parti No	KKG06A6
Müşteri	BOĞAZİÇİ ÜNİVERSİTESİ
Vasıta Plaka No	
Fabrika Çıkış Tarihi	05.07.2006

Sıra No	Muayene ve Deneyler	İlgili Standartlar
1	Elek Analizi	TS 5426 / 5425

elek göz açıklığı (mm)	elek üstü a (gr)	elek üstü b (%)	elek altı c (%)	elek üstü küm	elek altı küm.
		0,00	0,00	0,00	100,00
1,400	0,000	0,00	0,00	0,00	100,00
1,000	0,000	0,00	0,00	0,00	100,00
0,710	0,000	0,00	0,00	0,00	100,00
0,500	0,000	0,00	0,66	0,00	100,00
0,355	0,330	0,66	14,13	0,66	99,34
0,250	7,060	14,13	51,62	14,79	85,21
0,180	25,790	51,62	31,93	66,41	33,59
0,125	15,950	31,93	1,58	98,34	1,66
0,090	0,790	1,58	0,08	99,92	0,08
0,063	0,040	0,08	0,00	100,00	0,00
0,020	0,000	0,00	0,00	100,00	0,00
Toplam	49,96	100,00	100,00		

Tane Boyutu		Sonuçlar
	AFS	65,42
	Mikron	203,95
2	Teorik Özgül Yüzey (cm^2/g)	115,97
3	Dağılım Katsayısı ($S_0=Q_1/Q_3$)	1,41
	Q_1 (mm)	0,24
	Q_3 (mm)	0,17
4	Ortalama Tane Büyük. (Mk-M50)	0,20
	2/3 Mk	0,14
	4/3 Mk	0,27
	Homojenlik Derecesi %	

50
5
89
84

Sıra No	Muayene ve Deneyler	İlgili Standartlar	Sınır değerler	Sonuçlar 1.Num	Sonuçlar 2.Num	Numune İçindir.
5	Gözle Muayene	TS 5426		OK.		
6	Bileşim	TS 2979				
	SiO_2 %			98,6		
	Fe_2O_3 %			0,23		
	CaO + MgO %			0,02+0,00		
	Na_2O + KO %			0,07+0,11		
	Al_2O_3 %			0,54		
7	Kızdırma Kaybı %	TS 2980		0,25		
8	Sinterleşme Sıcaklığı °C	TS 5426		>1500		Müşteri Şartname No:
9	Kil %	TS 5426				Yayın Tarihi:
10	Rutubet %	TS 3084				

Deneyi Yapan				Onay			
K.K.Teknisyeni	İmza	Tarih	Saat	K.G.Müdürü	İmza	Tarih	Saat
R.YÖRÜK		05/07/06	16:40	T YILDIZ		05/07/06	16:42

FRM.8.7.A.503 REV.01

Figure A.1. Chemical analysis of sand used in continuous flow experiments.

APPENDIX B

CALIBRATION CURVES FOR GC ANALYSIS

B.1. Calibration Curve of Phenol for GC Analysis

A series of phenol solutions of 100, 150, 200, 300, and 450 µM were injected to the GC to aciheve a calibration curve and it was used for the quantification of phenol as presented in Table B.1 and Figure B.1

Table B.1. Detected peak areas for the injected phenol solutions during calibration of GC.

Phenol Concentration, µM	Retention Time, min	Peak Area, pA.s
100	8.501	87.895
150	8.489	137.345
200	8.500	199.682
300	8.501	306.621
450	8.498	460.399

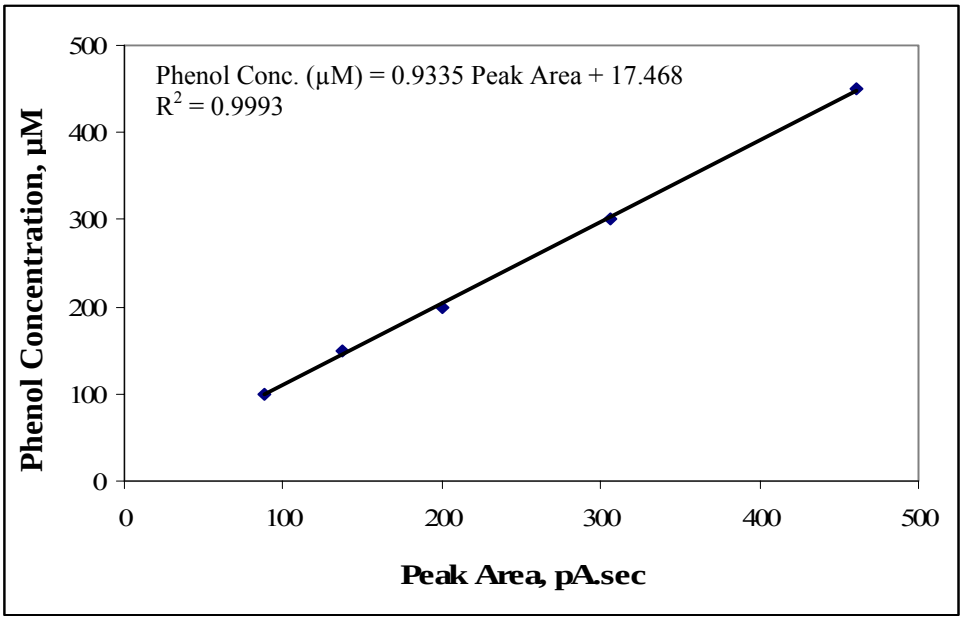

Figure B.1. Calibration curve of phenol for GC analysis.

B.2. Calibration Curve of 2-Chlorophenol for GC Analysis

A series of 2-chlorophenol (2-CP) solutions of 50, 100, 150, 200, 250, and 300 µM were injected to the GC to aciheve a calibration curve and it was used for the quantification of 2-CP as presented in Table B.2 and Figure B.2

Table B.2. Detected peak areas for the injected 2-CP solutions during calibration of GC.

2-CP Concentration, µM	Retention Time, min	Peak Area, pA.sec
50	8.768	81.46613
100	8.772	151.39774
150	8.773	228.90781
200	8.775	327.89496
250	8.777	386.69809
300	8.778	512.75403

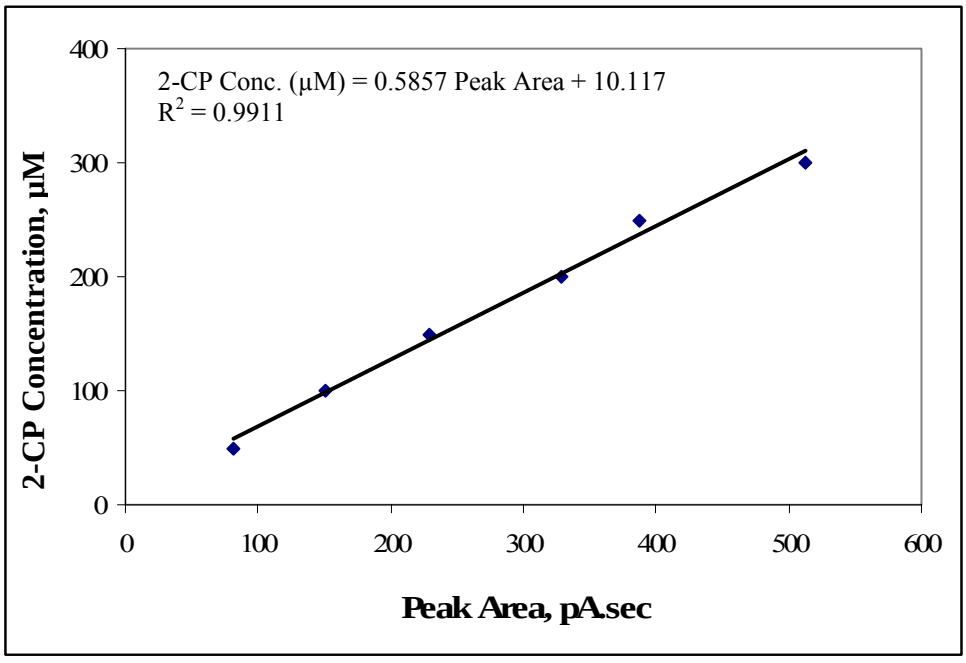

Figure B.2. Calibration curve of 2-chlorophenol for GC analysis.

APPENDIX C

H_2O_2 DETERMINATION BY THE I_3^- METHOD AND CALIBRATION CURVE

H_2O_2 determination was carried out according to the procedure described by Klassen et al. (1994). This method is based on the reaction of (I^-) with H_2O_2 to form the triiodide ion (I_3^-), which has a strong absorbance 351 nm. The analysis of H_2O_2 at concentrations as low as 1 μM is conveniently done by determining the yield of I_3^- formed when H_2O_2 reacts with KI in a buffered solution containing ammonium molybdate tetrahydrate as a catalyst.

Solutions A and B for the I_3^- method were prepared according to the recipe given by Klassen et al. (1994). Solution A consisted of 33 g of KI, 1 g of NaOH, and 0.1 g of ammonium molybdate tetrahydrate diluted to 500 mL with deionized water. The solution was stirred for ~1 h to dissolve the molybdate. Solution A was kept in dark to inhibit the oxidation of I^-. Solution B, an aqueous buffer, contained 10 g of KHP per 500 mL. Various concentrations of H_2O_2 was prepared from reagent grade H_2O_2 (35%), Merck. 2.5 mL of solution A, 2.5 mL of solution B, 1 mL of sample were mixed and diluted to 10 mL by deionized water, and the absorbance at 351 nm was recorded. Blank sample was prepared in the absence of sample. Various concentrations of H_2O_2 and the corresponding absorbance values at 351 nm are recorded for calibration curve, and given in Table C.1. Plot of H_2O_2 concentration versus the corresponding absorbance of the solution, and the calibration curve for H_2O_2 analysis in sonicated samples is given in Figure C.1.

Table C.1. H_2O_2 concentration versus absorbance at 351 nm data used for calibration curve preparation.

H_2O_2 concentration (mg L^{-1})	Absorbance at 351 nm
0.40	0.019
0.79	0.044
1.18	0.070
1.58	0.092
1.98	0.121
2.37	0.146
3.16	0.207
3.96	0.253

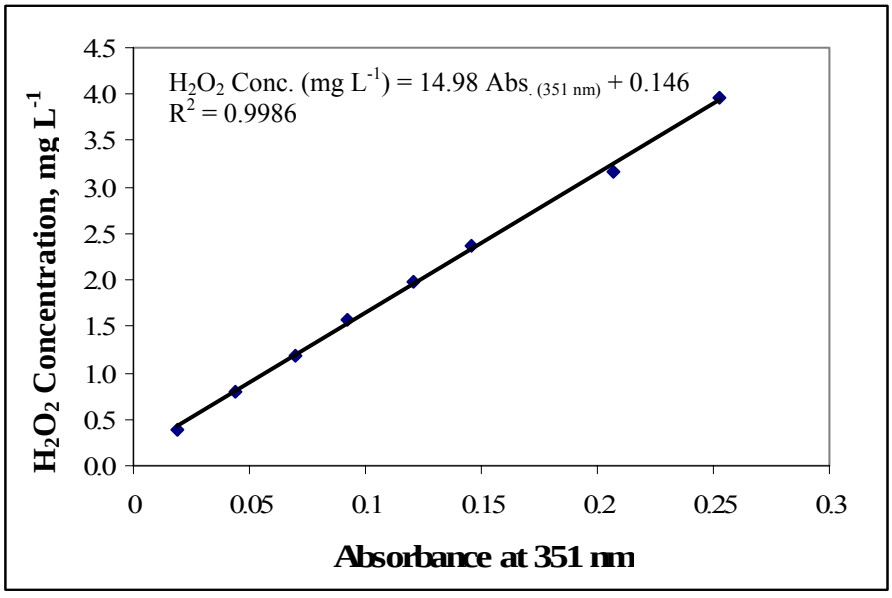

Figure C.1. H_2O_2 calibration curve.